FEDERAL UNIVERSITY OF TECHNOLOGY – PARANÁ
POSTGRADUATE PROGRAMME IN MECHANICAL AND MATERIALS ENGINEERING

ALAN LUGARINI DE SOUZA

LATTICE BOLTZMANN METHOD FOR DIRECT NUMERICAL SIMULATION OF VISCOPLASTIC TURBULENT FLOW

Thesis

CURITIBA
2020

ALAN LUGARINI DE SOUZA

LATTICE BOLTZMANN METHOD FOR DIRECT NUMERICAL SIMULATION OF VISCOPLASTIC TURBULENT FLOW

Método dos Retículos de Boltzmann para Simulação Numérica Direta de Escoamento Viscoplástico Turbulento

Thesis presented to the Postgraduate Programme in Mechanical and Materials Engineering (PPGEM) from the Federal University of Technology - Paraná, as partial fulfillment of the requirements for the degree of Doctor of Sciences.

Advisor: Prof. Dr. Admilson T. Franco
Co-Advisor: Prof. Dr. Paulo C. Philippi

CURITIBA
2020

Ministério da Educação
Universidade Tecnológica Federal do Paraná
Câmpus Curitiba

ALAN LUGARINI DE SOUZA

MÉTODO DOS RETÍCULOS DE BOLTZMANN PARA SIMULAÇÃO NUMÉRICA DIRETA DE ESCOAMENTO VISCOPLÁSTICO TURBULENTO

Trabalho de pesquisa de doutorado apresentado como requisito para obtenção do título de Doutor Em Engenharia da Universidade Tecnológica Federal do Paraná (UTFPR). Área de concentração: Engenharia Térmica.

Data de aprovação: 18 de Dezembro de 2020

Prof Admilson Teixeira Franco, Doutorado - Universidade Tecnológica Federal do Paraná

Prof Cezar Otaviano Ribeiro Negrao, Doutorado - Universidade Tecnológica Federal do Paraná

Prof Diogo Berta Pitz, Doutorado - Universidade Federal do Paraná (Ufpr)

Prof Luiz Adolfo Hegele Junior, Doutorado - Fundação Universidade do Estado de Santa Catarina (Udesc)

Prof Silvio Luiz De Mello Junqueira, Doutorado - Universidade Tecnológica Federal do Paraná

LUGARINI DE SOUZA, ALAN. **Método dos Retículos de Boltzmann para Simulação Numérica Direta de Escoamento Viscoplástico Turbulento**. Tese. Programa de Pós-Graduação em Engenharia Mecânica e de Materiais, Universidade Tecnológica Federal do Paraná, Curitiba, Brasil, 104 páginas, 2020.

RESUMO

Escoamentos turbulentos de fluidos viscoplásticos estão presentes em várias aplicações industriais. No entanto, o desenvolvimento de métodos e modelos de simulação para turbulência em fluidos não Newtonianos ainda está em fase inicial. Nesta tese, um esquema numérico baseado no método dos retículos de Boltzmann (LBM) foi desenvolvido para escoamentos de fluidos viscoplásticos. Em seguida, esse esquema foi usado em simulações numéricas diretas de escoamento em canal turbulento com fluido viscoplástico. Foi formulada uma metodologia numérica completa para o escoamento do fluido de Bingham, bem como a expansão de Chapman-Enskog para a demonstração de sua equivalência macroscópica. O uso de regularização de momentos fantasmas resultou em simulações notavelmente estáveis, com frequências de relaxamento muito baixas ou altas. Uma excelente característica do LBM é a possibilidade de representar viscosidade infinita ajustando a frequência de relaxação para zero. Isso permite a representação da equação constitutiva de Bingham sem artefatos. Casos de benchmark de regimes permanente e transiente foram resolvidos a fim de validar o presente esquema LB. Para o escoamento turbulento em canal com fluido Bingham, o número de Reynolds de atrito foi fixado em 180, enquanto o número de Bingham variou de 0 (Newtoniano) a 0,15. É mostrado que porções plásticas de material são transportadas pelo escoamento ao redor da linha central. Ao contrário do que alguns estudos sugerem, essas porções plásticas não desaparecem rapidamente, mas têm uma vida útil significativa. Outro resultado interessante é que a tensão limite de escoamento tem o efeito de aumentar a anisotropia da turbulência, fazendo com que as flutuações da velocidade normal e transversal diminuam, enquanto que a componente na direção do escoamento aumenta. Em geral, os resultados numéricos diretos obtidos por LBM foram muito semelhantes aos obtidos por outros métodos numéricos.

Palavras-chave: Método dos Retículos de Boltzmann, Viscoplástico, Turbulência, Simulação Numérica Direta.

LUGARINI DE SOUZA, ALAN. **Lattice Boltzmann Method for Direct Numerical Simulation of Viscoplastic Turbulent Flow**. Thesis. Postgraduate Programme in Mechanical and Materials Engineering, Federal University of Technology – Paraná, Curitiba, Brazil, 104 pages, 2020.

ABSTRACT

Turbulent flows of viscoplastic fluids are present in a number of industrial applications. However, the development of simulation methods and models for non-Newtonian turbulence are still in its early days. In this thesis, a numerical scheme based on lattice Boltzmann method (LBM) was developed for viscoplastic fluid flows. Then, this scheme was used in direct numerical simulations of viscoplastic turbulent channel flow. A complete numerical methodology for Bingham fluid flow was formulated, as well as the Chapman-Enskog expansion for the demonstration of its macroscopic equivalence. The use of regularization of ghost moments has resulted in remarkably stable simulations, at very low or high relaxation frequencies. A great characteristic of LBM is the possibility of representing infinite viscosity by setting the relaxation frequency to zero. This enables the representation of the Bingham constitutive equation without artifacts. Steady-state and transient benchmark cases were solved in order to validate the present LB scheme. For the turbulent channel flow with Bingham fluid, the friction Reynolds number was fixed at 180, while the Bingham number varied from 0 (Newtonian) to 0.15. It is shown that unyielded portions of material travel along with the flow around the centerline. Unlike some studies suggested, these unyielded spots do not disappear quickly, but rather have a significant life-time. Another interesting outcome is that the yield stress has the effect on increasing the turbulence anisotropy, by making the spanwise and normal velocity fluctuations lower, while the streamwise component increases. In general, the direct numerical results achieved by LBM were very similar to those obtained by other numerical methods.

Keywords: Lattice Boltzmann Method, Viscoplastic, Turbulence, Direct Numerical Simulation.

ACKNOWLEDGMENTS

Many people wanted to see this work finished. If it were not for them, it would take me another four years to see the end of it. I am blessed to have the support of a loving family. My son Vitor was not even born when I started in the doctorate program. In some ways, I raised two children hand in hand. Every now and then Vitor would knock on my door and ask me to play. I tell him daddy has to work, and he kindly understand it and turns back to his toys. I think he knows I do it for him. My wonderful wife Renata gave me everything I needed to focus on the work. Not only that, she has advised me on everything related to graphic design, such as copy-editing, figures and presentations. This thesis is as much as mine as it is hers. I have felt immense encouragement and support from my mother Josiani, my father João and my brother Igor. They have tried everything, and succeeded, to keep me strong.

An enormous gratitude goes to my advisor Admilson T. Franco. He mentored me for ten years with wisdom and patience. I think this thesis, particularly the chapter on viscoplastic turbulence, is the best work of our partnership. I have also a great appreciation for Paulo C. Philippi and his counseling on LBM. It was great to have him onboard. I thank all of the examiners for their constructive criticism and advices. Many of their suggestions, made during the project evaluation, have impacted the final version of this work.

This work was done in a very productive environment. I was lucky to be surrounded by highly skilled people. I would like the express my sincere thanks to a few names. Vinicius Daroz, for his friendship and endless conversations on turbulence. Luiz Gustavo, for the expert technical support with the GPU servers. Waine B. Oliveira Jr., for his brilliant LBM implementation for GPU. Marco A. Ferrari and Rodrigo S. Romanus, for all of their help and unrelenting will to move the needle with their work. My gratitude extends to all students, researchers and personnel from the Research Center for Rheology and Non-Newtonian Fluids – CERNN.

This study was financed in part by the Coordenação de Aperfeiçoamento de Pessoal de Nível Superior - Brasil (CAPES) - Finance Code 001.

LIST OF FIGURES

LIST OF TABLES

LIST OF ABBREVIATIONS AND ACRONYMS

ALM	Augmented Lagrangian Method
BGK	Bhatnagar-Gross-Krook Collision Operator
DNS	Direct Numerical Simulation
FVM	Finite Volume Method
GNF	Generalized Newtonian Fluid
GPU	Graphics Processing Unit
HWBB	Halfway Bounce-Back
LBGK	Lattice BGK Equation
LBM	Lattice Boltzmann Method
MRT	Multiple Relaxation Time
NEBB	Non-Equilibrium Bounce-Back
NSE	Navier-Stokes Equation
RANS	Reynolds-Averaged Navier-Stokes
RBGK	Regularized BGK Collision Operator

NOMENCLATURE

Latin letters

$\boldsymbol{A}$	Dummy tensor	[-]
$\boldsymbol{c}$	Velocity set vector	[-]
c_s	Sound speed	[m.s^{-1}]
C	Correction coefficient	[-]
d	Number of spatial dimensions	[-]
D	Diameter	[m]
f	Friction factor / Particle distribution function	[- / kg.s^{3}.m^{-6}]
F	Volumetric body force	[N.m^{-3}]
H	Height	[m]
l	Length scale	[m]
L	Length	[m]
L_2	Quadratic error norm	[-]
L_{ST}	Steady state residual	[-]
N	Number of lattice nodes	[-]
$\mathcal{O}$	Order of magnitude	[-]
p	Pressure	[Pa]
q	Number of discrete velocities	[-]
$\boldsymbol{Q}$	Lattice velocities tensor $Q_{i\alpha\beta} = c_{i\alpha}c_{i\beta} - c_s^2\delta_{\alpha\beta}$	[-]
R / $\boldsymbol{R}$	Ideal gas constant / Velocity correlation function	[J.K^{-1}.mol^{-1} / m^{2}.s^{-2}]
t	Time	[s]
$\boldsymbol{t}$	Tangent vector	[-]
T	Temperature / Elapsed time in lattice units	[K / -]
$\boldsymbol{u}$	Flow velocity vector	[m.s^{-1}]
U	Reference velocity	[m.s^{-1}]
$\boldsymbol{v}$	Relative velocity vector	[m.s^{-1}]
$\boldsymbol{x}$	Cartesian position vector	[m]
x, y, z	Cartesian coordinates	[m]
w	Velocity set weight	[-]

Greek letters

$\dot{\boldsymbol{\gamma}}$	rate-of-strain tensor	[s^{-1}]
δ / $\boldsymbol{\delta}$	Channel half-height / Kronecker's delta	[m / -]
ϵ	Expansion parameter	[-]
ε	Rate of dissipation of kinetic energy	[J.m^{-3}.s^{-1}]
η	Viscosity	[Pa.s]
μ	Dynamic viscosity	[Pa.s]
ν	Kinematic viscosity	[m^{2}.s^{-1}]

$\boldsymbol{\xi}$	Particle velocity vector	[m.s^{-1}]
$\boldsymbol{\Pi}$	Second moment of discrete particle distribution function	[-]
ρ	Density	[kg.m^{-3}]
$\boldsymbol{\sigma}$	Extra stress tensor	[Pa]
τ	Relaxation time	[s]
ω	Relaxation frequency	[s^{-1}]
Ω	Collision operator	[kg.s^{2}.m^{-6}]

Non-dimensional groups

Bi	Bingham number, $\sigma_y L/U\eta_p$ or $\sigma_y/\overline{\sigma}_{\mathrm{w}}$	[-]
He	Hedstrom number, $\rho\sigma_y L^2/\eta_p^2$	[-]
Kn	Knudsen number, ℓ_{mfp}/ℓ	[-]
Ma	Mach number, U/c_s	[-]
Re	Reynolds number, $\rho UL/\mu$	[-]
Re_p	Plastic Reynolds number, $\rho UL/\eta_p$	[-]
Re_p	Friction Reynolds number, $\rho u^* \delta/\eta_p$	[-]

Superscripts

$(\,)^*$	Post-collision or wall-scaled property
$(\,)^{\mathrm{eq}}$	Equilibrium
$(\,)^{\mathrm{neq}}$	Non-equilibrium
$(\,)^{\mathrm{reg}}$	Regularized
$(\,)^T$	Transposed

Subscripts

$(\,)_0$	Initial
$(\,)_{\alpha,\beta,\gamma}$	Cartesian directions
$(\,)_{\mathrm{a}}$	Atom or molecule
$(\,)_b$	Boundary or bulk property
$(\,)_c$	Center
$(\,)_{\mathrm{conv}}$	Convection
$(\,)_{\mathrm{diff}}$	Diffusion
$(\,)_i$	Discrete velocity direction
$(\,)_{\mathrm{mfp}}$	Mean free path
$(\,)_p$	Plastic
$(\,)_S$	System
$(\,)_t$	Tangent
$(\,)_{\mathrm{w}}$	Wall
$(\,)_y$	Yield

CONTENTS

1 INTRODUCTION

1.1 Context and Motivation

Turbulent flow of yield stress (or viscoplastic) fluids take place in a number of natural or industrial instances. As examples, one can mention the slurry transport in mining activities, arterial blood flow and mud flow in wellbore drilling. In the mining industry, it is often necessary to transport ore for long distances, for further processing, treatment and disposal. This ore may be mixed with a fluid, such as water, and be efficiently transported for many kilometers (GUANG et al., 2011). The thin mixture is called slurry and it can exhibit a yield stress. The flow regimes in mining slurry transport can be laminar, transitional or fully turbulent. In order to design efficient pipeline and pumps, friction factor estimation needs good accuracy. Rheological uncertainty and lack of comprehensive experimental data make this a difficult task.

Blood flow in arteries can transition to turbulence when cholesterol and other lipids deposit beneath the intima of the arterial wall, creating stenosis (MOLLA and PAUL, 2012). This biological fluid is a complex suspension that possesses many non-Newtonian characteristics, including yield stress (PICART et al., 1998). Flow patterns and fluctuations caused by turbulence are associated with some pathologies. For instance, high wall shear stresses influence endothelial damages of vessel and atherosclerosis. As shown by Molla and Paul (2012), the post-stenotic flow has a recirculation zone, which may become momentarily unyielded. Thus, combined modeling of viscoplasticity and turbulence would be desired as an analysis tool for arterial blood flow.

Figure 1.1 – Illustration of hole cleaning processes in typical oil-well drilling. (a) In vertical wells the mud may undergo turbulent flow inside the drill string, though the flow in the annular region is most likely laminar due to the larger cross section area. (b) In horizontal wells subject to laminar flow a cuttings bed is formed, which may obstruct the drill string and eventually interrupt its movement. One of the possible workarounds is to induce turbulence in order to resuspend cuttings and free the drill string.

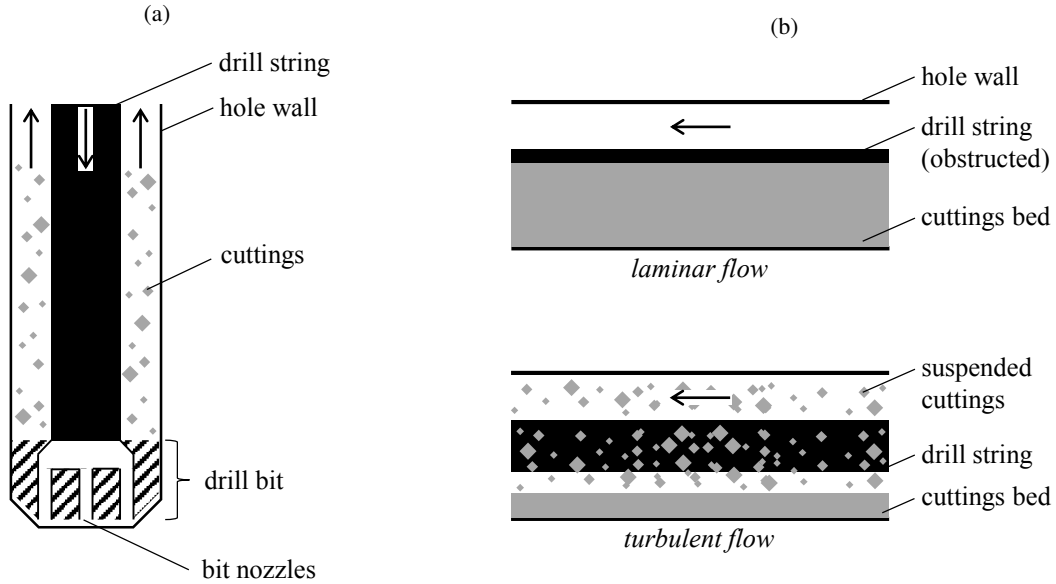

Source: the author.

In the wellbore drilling process, a viscoplastic fluid is often used as drilling fluid due to its ability to keep cuttings suspended (MITCHELL and MISKA, 2011). In this particular industry, the drilling fluid is called mud. Figure 1.1a illustrates a vertical well being drilled. The mud is pumped into the drill string, passes through the bit nozzles, and returns upwards in the annular region formed between the string and the hole walls. It is well known that at high flow rates a turbulent regime may take place inside the drill string. In the annular region, the mud flow path comes across a series of contractions where turbulence can be induced, such as in the bit nozzles, stabilizers and tool joints. Another occasion in which the mud may undergo turbulent flow is during the cleaning of a horizontal well obstructed by a cuttings bed. Figure 1.1b depicts how the turbulent mud flow can keep more cuttings suspended, in contrast to the laminar flow. Indeed, inducing turbulence in horizontal wells is one of the techniques employed in case of serious obstruction risks caused by poor hole cleaning (OKRAJNI and AZAR, 1986). Given the variety of situations in which viscoplastic turbulent flow happens during oil-well drilling operations, it is important to have reliable predictive methods to assist in decision making processes and to improve the design of drilling accessories.

Although the above mentioned and many other applications are related to the turbulent flow of viscoplastic fluids, the present work is mainly motivated by the oil-well drilling and completion industry. Despite the long research history in this field, there are still many limitations on the accuracy of predictive methods. Quantities of interest, such as friction factors and velocity fields, are difficult to be reliably estimated. The empirical correlations available in the literature have to be used with care, for they typically fit a complex thixotropic elastoviscoplastic material's response to a simple constitutive equation, such as the Bingham model. Moreover, closure models for turbulence equations of Non-Newtonian fluids are still in their early days. The approach of the present work is to take advantage of the scalability of the lattice Boltzmann method to achieve cost-effective direct numerical simulations of viscoplastic turbulent flow. Therefore, this work has a prominently scientific character, and its vision is guided towards industry needs.

1.2 Literature Review

In this section a review of the pertinent literature on viscoplastic turbulent flow is presented. The scope of the present review is limited to studies on fluids with yield stress and insignificant thixotropy or elasticity. A formal definition of viscoplastic material is given in Chapter 2. The bibliographic material on the subject can be broadly divided into three approaches, which in the following text will be discussed separately. Section 1.2.1 discusses the most important works on empirical correlations for the friction factor. In section 1.2.2, experimental investigations on the detailed velocity field will be discussed. In section 1.2.3, focus will be on reports of direct numerical simulations. Finally, the most important remaining open questions are highlighted in section 1.2.4, revealing the scientific opportunity explored in the present thesis. Their relevance with respect to oil-well drilling engineering is explained whenever opportune. Also, the reasons why direct numerical simulation is a potential candidate to clarify the above issues are emphasized.

1.2.1 Friction Factor

Before getting into the subject of friction factor itself, the relevant dimensionless groups and the efforts made to characterize laminar-to-turbulent transition will be mentioned. The most used parameter to determine pipe flow transition of Bingham fluids is the plastic Reynolds number, defined as $Re_p = \rho UD/\eta_p$, where ρ is the density, U is the average fluid velocity, D is the pipe's diameter and η_p is the plastic viscosity according to the Bingham fluid constitutive equation (Eq. 2.40). Another relevant parameter to determine the flow behavior of yield stress fluids is the Hedstrom number, $He = \rho\sigma_y D^2/\eta_p^2$, where σ_y is the yield stress. This dimensionless group was defined in Hedström's work on turbulent slurry flow (HEDSTRÖM, 1952), one of the first exhibition of theoretical analysis on the subject. Based on a few experimental data for cement rock suspensions, Hedström was able to draw meaningful conclusions. He correctly predicted that the critical Reynolds number for the onset of turbulence increases with He. Moreover, the friction factor for turbulent slurry flow was estimated to be close to that of a Newtonian fluid with $\mu = \eta_p$. Even though this is a questionable approximation, it is still recommended in oil-well drilling manuals (API, 2010).

An early effort to determine the laminar-to-turbulent transition of yield stress fluid flow was made by Caldwell and Babbitt (1941). The authors believed transition should take place at $Re_p \approx 2500$, and calculated a critical velocity for transition. Hanks (1963) and Hanks (1967) took a step further and presented a more rigorous mathematical development considering a Bingham fluid, which proved consistent against extensive experimental data. Hanks' transition criteria for pipe flow, showed graphically in Figure 1.2, is present in many drilling hydraulics textbooks. Shah and Sutton (1990) curve-fitted Hanks' equation to cement slurry data and obtained an alternative correlation for critical Re_p as a function of He, although it may fail to represent other slurry varieties.

Figure 1.2 – Critical plastic Reynolds number (vertical axis) as a function of Hedstrom number (horizontal axis). Hanks' correlation is the solid line. The markers represent experimental data from third-parties.

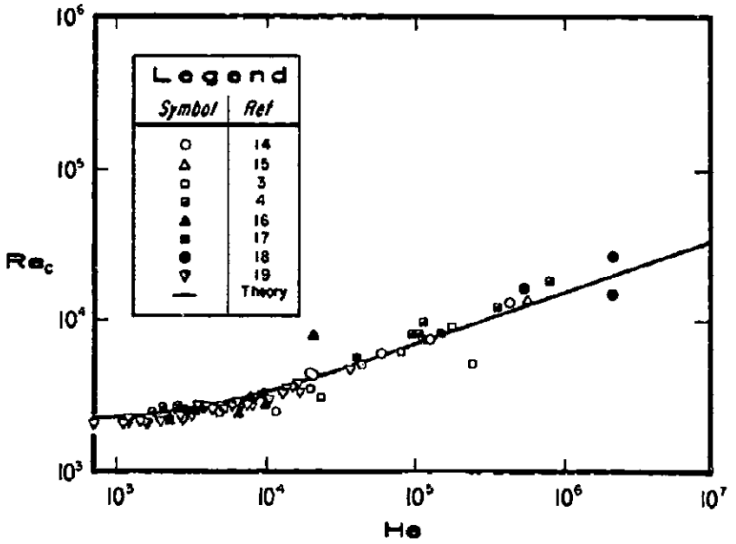

Source: Hanks (1967).

The current understanding of transition in pipe flow of viscoplastic fluids dictates that it happens in two stages. First, low frequency oscillations of the axial velocity may be observed near the wall, while the central region has an either true (PEIXINHO et al., 2005) or pseudo-plug flow (GÜZEL et al., 2009).

In this stage the friction factor departs slightly from the laminar curve. Eventually, the friction factor reaches a local minimum. Then, with further increasing Re_p, turbulent spots appear in the form of puffs (or slugs), that are initially far from each other (GÜZEL et al., 2009). Between two successive puffs, the presence of the plug zone is possible, characterizing a type of viscoplastic intermittent flow. The friction factor then increases with Re_p because of the increasing size of puffs. At some point, these spots fill up the whole pipe, and the flow reaches a fully turbulent regime. In the fully turbulent flow at feasible He and Re_p, there have been yield stress effects observed (SHAH and SUTTON, 1990; HALLBOM, 2008), even though the asymptotic behavior of the friction factor is expected to approach the Newtonian's as $Re_p \to \infty$. The general picture of the transition for a viscoplastic material is similar to a Newtonian fluid. However, the critical points and transition ranges remain to be clarified.

Dodge and Metzner (1959) suggested that their power-law fluid correlation correctly represented the friction factor for viscoplastic fluids, as if the yield stress would have a negligible effect during fully turbulent flow. Although their expression correlated well for attapulgite clay suspension, the validity of their approach for viscoplastic fluids has been questioned by several authors (GOVIER and AZIZ, 1972; HANKS and RICKS, 1975). After Hedström (1952), a relevant theoretical analysis of Bingham fluid turbulent flow was done by Tomita (1959), who derived an expression for fully turbulent friction factor based on Prandtl's mixing length concept. Thomas (1962) made another interesting contribution. He developed a Blasius type equation through data-fitting of flocculated suspensions of kaolin, titanium dioxide and thorium oxide in water. His results showed the friction factors of these suspensions to be smaller than those of water. Contrary to the views of Hedström and Hanks, neither Tomita's or Thomas' correlations can be expressed in terms of He.

Figure 1.3 – Friction factor for a Bingham fluid (vertical axis) as a function of plastic Reynolds number (called "N_{Re}" in the horizontal axis). The dashed curve represents the critical plastic Reynolds number.

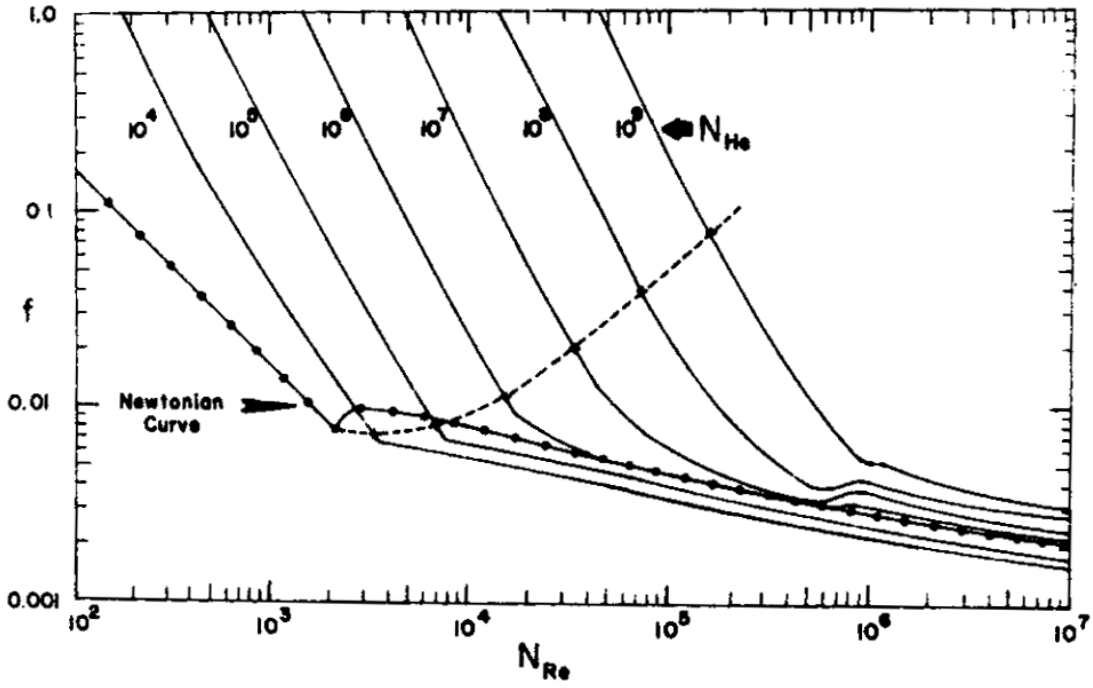

Source: Hanks and Dadia (1971).

The first comprehensive friction factor chart for a Bingham fluid was presented by Hanks and Dadia (1971), and it is exhibited in Figure 1.3. They performed a semi-theoretical formulation and obtained

a numerical routine for the calculation of f. Hanks would latter extend the methodology for Herschel-Bulkley fluids (HANKS, 1978). Many drilling textbooks and engineering manuals cite Darby and Melson (1987) for the friction factor of Bingham turbulent flow. It must be emphasized that Darby and Melson simply fitted data points present in (HANKS and DADIA, 1971) to a convenient mathematical expression, so it seems that more credit should be given to the work of Hanks and Dadia. The most interesting features of Figure 1.3 are listed below:

- Transition seems to occur in two stages, as depicted by Peixinho et al. (2005). However, the local minima are only present for $He \geq 10^6$.
- The transition range for $He \geq 10^6$ spans an order of magnitude in Re_p, while for $He < 10^6$ the transition is rather abrupt.
- On fully turbulent flow, all curves are parallel to the Newtonian flow curve;

Besides the paper by Hanks (1978), the Hershel-Bulkley model was explored by Wilson and Thomas (1985), Thomas and Wilson (1987). They employed velocity scale arguments to re-calibrate the conventional viscous layer thickness and logarithmic sub-layer constants for the case of non-Newtonian flow. For the sake of simplicity, only the Bingham friction factor is reproduced here. Figure 1.4 shows Wilson and Thomas' friction factor along with experimental data points. The most important contrasting features in relation to (HANKS and DADIA, 1971) are:

- The transition region for $He < 10^6$ is significantly broader;
- The transition region for $He \geq 10^6$ is significantly narrower;
- All constant He curves merge into the same fully turbulent curve, corresponding to a Newtonian behavior at high Re_p.

Figure 1.4 – Bingham model friction factor (vertical axis) as a function of plastic Reynolds number (horizontal axis). The solid lines represent the turbulent friction factor and the markers are experimental data points.

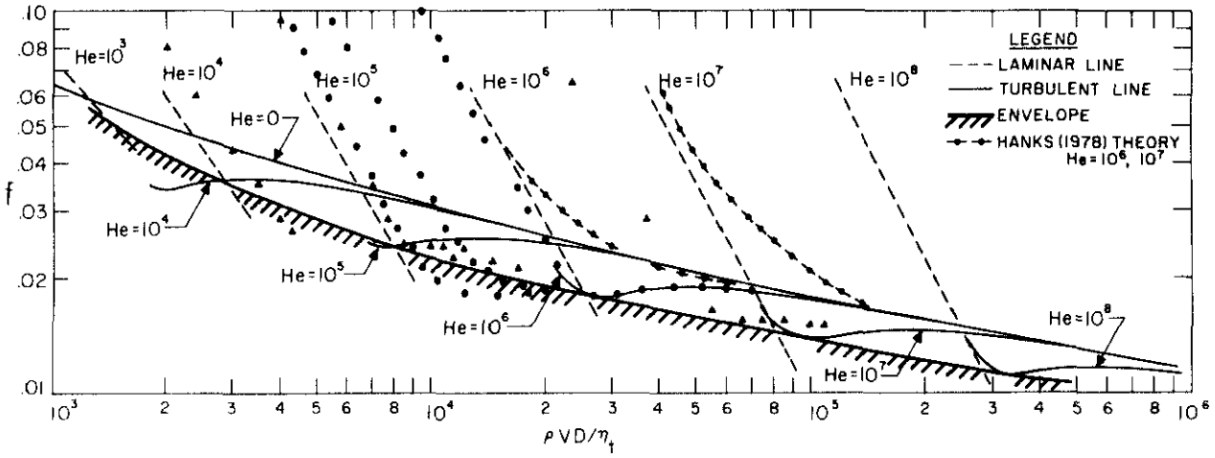

Source: Wilson and Thomas (1985).

In the present author's opinion, the overall available experimental data seem to support Wilson and Thomas' short transition range. However, treating fully turbulent f as independent of He is questionable,

for no conclusive data has pointed that way. Shah and Sutton (1990) conducted extensive experiments on cement slurry and fitted its rheological parameters to a Bingham fluid. They curve-fitted its flow loop results and identified distinct fully turbulent curves for He smaller and higher than 10^5. Also, both curves fell below the Newtonian curve, which qualitatively agrees with Hanks and Dadia's theory. In practice, it is difficult to reach high Re_p and high He in experimental flow loops. Therefore, one must consider that in realistic viscoplastic turbulent flows, the Newtonian approximation may not apply.

Recently, an entirely theoretical determination of Bingham friction factor was published by Anbarlooei et al. (2017). They used scale arguments and re-examined the energy cascade and energy spectrum theories under the influence of yield stress. For the range $5 \times 10^5 \leq He \leq 2 \times 10^6$, their theoretical friction factor expression seemed to better represent the experimental data than the correlation by Darby and Melson (1987) (curve-fitting of Hanks and Dadia's theory). The comparison with DNS data also looked very good (ANBARLOOEI et al., 2018). This theoretical development represents a significant advance towards understanding the effects of rheological parameters into turbulent flow. The limits of influence of many rheological characteristics such as thixotropy, elasticity and plasticity, on turbulence are far from being well understood. For the oil industry particularly, it would be beneficial to the drilling engineer to know at what conditions plasticity or elasticity can or cannot be neglected.

It can be noticed from this literature review that there exists a lack of experimental effort to characterize turbulent friction factor for viscoplastic fluids from 1990 on. Comprehensive experimental studies demand significant investments in infrastructure, rheometry and fluid supply. As an example of the grandiosity of such installation, the Low Pressure Ambient Temperature (LPAT) flow loop of the University of Tulsa Drilling Research Projects (TUDRP) may be cited. The LPAT, pictured in Figure 1.5 is one of the largest flow loops in the world. It consists of a 100 feet long test section, a transparent acrylic outer casing (8 in. ID) and an aluminum inner drill pipe (4.5 in. OD). Drilling fluid can be pumped at up to 700 gpm. The fluid volume required is approximately 1000 liters. This test facility was designed for the study of cuttings transport. However, in order to obtain high Re and high He data for real industrial muds or slurries, a similar installation would be necessary. Given such level of expenses, it is reasonable to believe that more accurate and extensive data exist, but are under proprietary protection.

Figure 1.5 – The Large Indoor Flow Loop (LPAT) of the University of Tulsa Drilling Research Projects (TUDRP).

Sources: http://www.tudrp.utulsa.edu (TUDRP website) and (DUAN et al., 2008).

1.2.2 Flow Visualization

Motivated by the interest in drag reduction mechanisms of polymer solutions, some visualization studies of non-Newtonian turbulent flow were published (PINHO and WHITELAW, 1990; PEREIRA

and PINHO, 1994; PEREIRA and PINHO, 2002). From velocity profile data, an apparent asymmetry caught the attention of researchers. As a means to eliminate any directional bias from the experimental apparatus, Escudier et al. (2005) performed laser Doppler anemometry (LDA) measurements in unrelated research programs in UK, France and Australia. They used a selection of polymer and clay suspensions, and fitted their rheological curves in either Carreau-Yasuda or Herschel-Bulkley models. The results revealed varying degrees of departure from symmetry in transitional pipe flow. Interestingly, symmetry was maintained for laminar and fully turbulent flows. Typical velocity profiles, obtained by a subsequent work, are shown in Figure 1.6. After eliminating other hypotheses, the authors came to the conclusion that the asymmetry must be a consequence of a fluid-dynamic mechanism rather than imperfections in the flow facilities.

Figure 1.6 – Mean axial velocity profiles at different Reynolds number. The working fluid is a 0.2 wt% aqueous solution of Carbopol 940, with Herschel-Bulkley parameters $\sigma_y = 9.75$ Pa, $K = 3.82$ Pa.s^n, $n = 0.47$.

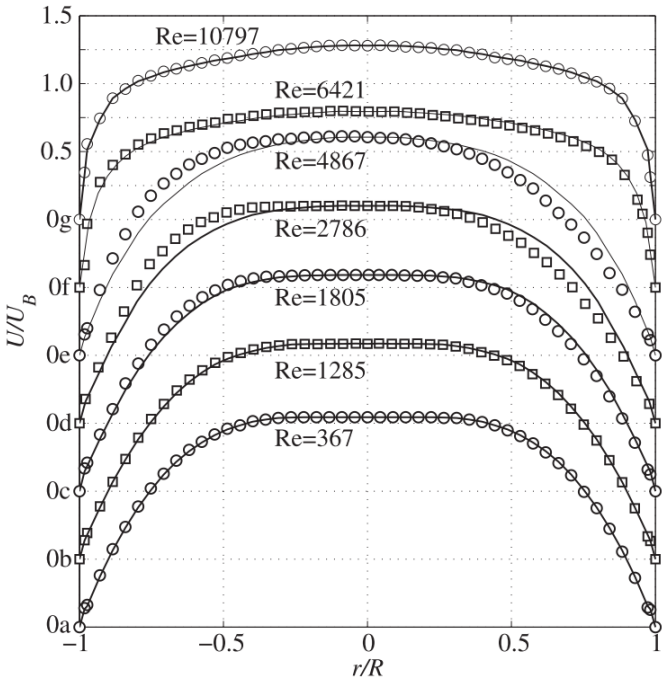

Source: Esmael and Nouar (2008).

Since it was still not clear which rheological characteristic was responsible for the asymmetry, Peixinho et al. (2005) conducted an experimental study of the laminar, transitional and turbulent flow for three fluids: a Newtonian glucose syrup, a shear-thinning CMC solution and a yield-stress Carbopol solution. The Carbopol solution was fitted into a Herschel-Bulkley model with $\sigma_y = 7.2$ Pa, $k = 4.3$ Pa.s^n, $n = 0.47$. Both non-Newtonian fluids exhibited asymmetric velocity profiles at transitional flow, thereby ruling out the possibility of yield stress being responsible for the phenomenon. Elasticity effects were considered negligible based on the evaluation of the first normal stress difference (N_1). An attempt to characterize the asymmetric non-Newtonian flow was made by Esmael and Nouar (2008). They provided a three-dimensional description of this phenomenon from axial velocity profiles measurements at various axial and azimuthal positions. It was observed a robust nonlinear coherent structure characterized by two weakly modulated counter-rotating longitudinal vortices. They found that the asymmetry was intensified along the pipe axis. Bahrani and Nouar (2014) demonstrated experimentally that the asymmetric velocity

profile is related to the emergence of turbulent spots, corresponding to the second stage of transition.

The recent and extensive work of Wen (2016) comprises a series of three-dimensional measurements of shear-thinning and viscoelastic fluids under transitional pipe flow. Several degrees of shear-thinning and viscoelasticity were tested through different concentrations of xanthan gum and polyacrylic acid (PAA) solutions, respectively. It was observed that shear-thinning intensifies asymmetry, while viscoelasticy suppresses it. Moreover, the asymmetry has a preferred azimuthal and axial locations, which means there is no helical pattern of turbulence fluctuations. High-speed stereoscopic PIV data showed that when a turbulent puff went through the measurement plane, the average flow was symmetric. This implies that the laminar flow between puffs is deformed to an asymmetric state.

A detailed flow visualization study was performed by Güzel et al. (2009). They focused on the effect of yield stress on transition. Based on velocity fluctuations measurements, they sustained that transition only starts when the Reynolds stresses exceed the yield stress and the plug region has completely vanished. In this case, they were referring to the second stage of transition, corresponding to the appearance of puffs (or slugs). They concluded that in transitional or fully turbulent regime, a yield stress fluid behaves simply as a shear-thinning fluid. In the present author's opinion, it is questionable to expect that Reynolds stresses can alternate the yielding state of a viscoplastic fluid, since it is not a true stress. By the way, the conditional applied to any viscoplastic constitutive equation is on the magnitude of the extra (viscous) stress tensor, which does not include the Reynolds stress.

The experimental results of Güzel et al. (2009) and Peixinho et al. (2005) do not contradict each other, although their interpretation diverges regarding the turbulent transition characteristics. It is definitely too premature to accept that yield stress plays no role in transitional or fully turbulent flow. Conclusive experimental results would be too difficult to obtain, if possible at all, because they would require prototypical fluids with perfectly controlled rheology. As it was commented in the previous section, some of the friction factor data presented in the literature diverges at high Re_p (as noticed in Figure 1.4). Although shear-thinning has certainly the major effect in viscoplastic turbulent flow, the quantitative effect of yield stress still needs to be answered. Moreover, recent DNS results revealed that many unyielded fluid portions travel along with the turbulent elastoviscoplastic flow, disappearing and reappearing again somewhere else in the domain (ROSTI et al., 2018). Such numerical approaches are capable of elucidating essential questions on this field. This and other DNS articles will be discussed in the following section.

1.2.3 Direct Numerical Simulations

Direct numerical simulations (DNS) are becoming increasingly popular due to advances in high performance computation and numerical methods. They offer the advantage of not having to model closure terms in averaged or filtered momentum balance equations. In simple words, DNS consists of solving the momentum balance equations exactly as they are, in a grid fine enough to capture the intended time and space scales of the fluid motion. In the previous literature review, it was emphasized that the experimental approach to non-Newtonian turbulent flow is to assume that the fluid behaves according to a constitutive equation. However, doing so is practically equivalent to a regression exercise. Some constitutive parameters do not even have physical meaning. Real fluids do not obey to any constitutive equation, so there will always be some rheological characteristics that remain unrepresented. This is

where DNS stands out. With DNS it is possible to isolate the effects of any non-Newtonian parameter on turbulent flow, and consequently investigate limiting cases.

Even though there had been DNS studies of non-Newtonian fluid flow before, for investigations of drag reducing in polymer solutions, the first to consider the presence of yield stress was Rudman et al. (2004). The authors used a spectral element method to model power-law and Herschel-Bulkley pipe flow. The singular viscosity at zero shear rate was prevented by a cut-off value, equivalent to a viscosity regularization by bi-viscosity. The authors argued that the cut-off was never invoked. Although there were evidences of insufficient domain length, their results showed a qualitatively fair comparison with experimental data. For a power-law fluid with $n = 0.5$ an intermittent flow pattern was found, and there was a mention of an observed asymmetry. In a follow-up paper, Rudman and Blackburn (2006) focused on the yield stress parameter and revealed interesting features. It was seen that the yield stress significantly dampens turbulence fluctuations in the core region of the flow where a quasi-laminar flow co-exists with a transitional wall zone. Their results are in accordance with the experimentally-based conclusions of Güzel et al. (2009). However, Rudman and Blackburn (2006) did not provide any whole section velocity profile, which could be used to verify the occurrence of asymmetry.

Most of the DNS papers on purely viscous non-Newtonian flow deal exclusively with shear-thinning effects, since it is known to have a major importance compared to yield stress. Ohta and Miyashita (2014) developed a fourth-order central finite difference method to obtain DNS results for power-law fluid flow in a periodic channel. Despite the absence of yield stress, their work is worth mentioning by the fact that they attempted to use DNS data to model the turbulent viscous stress in large eddy simulation (LES). In LES, a turbulent viscous stress term appears as a consequence of filtering the fluid's non-linear stress term. They showed that a well-resolved LES can solve the non-Newtonian motion without consideration of the turbulent viscous stress. However, this would loose the advantage of LES in the first place, because a well-resolved LES is almost as expensive as a DNS. Therefore, Ohta and Miyashita (2014) employed a scale analysis to compute the turbulent viscous stress' effect into the standard Smagorinsky model. Their "extended" Smagorinsky model approximated the DNS results when coarse grids were used, indicating that viscosity fluctuations are very small scale features. When referring to DNS studies of shear-thinning fluids, one cannot fail to mention the pipe flow simulations of Singh et al. (2017b) and Singh et al. (2018), whose methodology is similar to Rudman et al. (2004), but the quality of analysis was much improved. Their most important findings can be summarized as follows: i) the mean bulk velocity is higher than for a Newtonian fluid, causing a minor drag reduction effect, ii) there is an increasing anisotropy of turbulence intensities when the power-law index is decreased, and iii) shear-thinning effects do not seem to disappear or collapse at high Re.

A very helpful article on rheology characterization for DNS input parameters was published by Singh et al. (2016). They emphasized the importance of using the correct shear rate range before the adoption of a constitutive equation and consequent use in turbulence simulations. According to the authors, the upper shear rate limit required in rheology characterization must be at least twice the shear rate corresponding to the mean wall shear stress. In practice, this is considerably higher than what is used in conventional rheometry. The reason for using high shear rheology is that the wall shear stress will be defined by flow at a very high shear rate. This could explain why previous DNS studies were not able to give accurate friction factor results. A particularly interesting observation made in (SINGH et al., 2016) is that the Hallbom's *Yield Plastic* model (HALLBOM and KLEIN, 2009) captured much

better the whole range rheogram (0.01 — 15000 s^{-1}) than the usual Herschel-Bulkley equation for a 0.075 wt% Carbopol solution in water. Singh et al. suggested that at high shear rates, the model type has little effect on turbulent flow predictions. In the present author's opinion, this is actually an outcome of the regression method used, most likely the least squares method (LSQ). Unless the squared terms are normalized, LSQ will favor the fitting of data with the highest absolute value. Using a normalized LSQ will probably evidence the unequal fitness of different constitutive equations.

Up to the present date, the most comprehensive DNS study focusing solely on viscoplasticity effect is (SINGH et al., 2017a). In this investigation, direct numerical simulations were carried out for Bingham fluid with yield stress equal to 5 to 20% of the mean wall shear stress, while the friction Reynolds number defined with wall viscosity was kept constant at 323. Bi-viscosity was employed by a cut-off in the strain rate. Figure 1.7 shows that increasing σ_y reduces the range of spatial scales of the flow and makes low speed streaks run longer in the streamwise direction. No unyielded fluid portions were found traveling with the turbulent flow. It was noticed that the yield stress had an effect similar to shear thinning as a turbulence damping mechanism. However, while shear thinning acts most inside the viscous sublayer, yield stress was found to only impact above this layer. An analysis of the turbulent kinetic energy budget revealed that the yield stress effect on turbulence was mainly confined to the near wall region ($y^+ \lesssim 60$). This is somehow counter-intuitive because strain rates are lowest in the core region, so one could expect yield stress manifestations in that area. In their work, the wall viscosity η_w was kept constant throughout all different cases. This parameter choice is misleading because, by changing yield stress, the plastic viscosity has to be changed also. Hence, it fails to isolate yield stress effects. As a way to avoid misinterpretations in future work, the plastic viscosity should be fixed.

Figure 1.7 – Instantaneous axial velocity contours: (left) at $y^+ = 10$ shown on developed cylindrical surfaces and (right) at a cross section. Plots for Newtonian fluid and Bingham fluids with σ_y equal to 5, 10 and 20% of the mean wall shear stress. Flow is from left to right, and lighter grey represents higher speed.

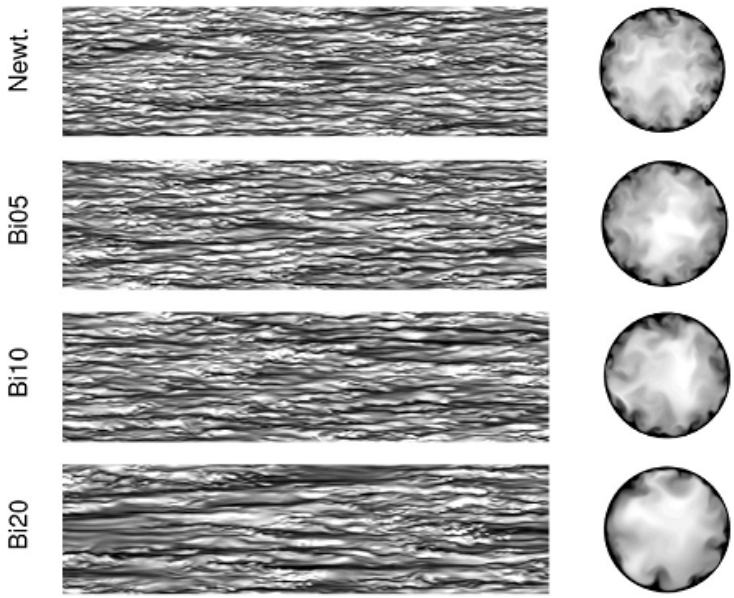

Source: Singh et al. (2017a).

A recent numerical investigation by Rosti et al. (2018) revealed that unyielded portions of fluid travel along with the flow for a material with elastoviscoplastic characteristics. They employed Saramito's constitutive model (SARAMITO, 2007), consisting of an Oldroyd-B viscoelastic fluid in the yielded

locations and recoverable Kelvin–Voigt viscoelastic deformation in the unyielded locations. The ratio of elastic to viscous forces was made very small (1%) as a means to focus on viscoplasticity effects. They carried out DNS for turbulent flow with $Re_p = 5600$. In Figure 1.8 a visual picture of the phenomena is given. Unyielded regions grow from the centerline towards the walls as the ratio He/Re_p increases. For a relatively high He/Re_p ratio (fourth picture from the top in Fig. 1.8) the authors observed a seemingly intermittent flow, with characteristics reminding the experimental investigation of Peixinho et al. (2005). The unyielded region interacts with the near-wall structures, forming preferentially above the high-speed streaks. With increasing yield stress, turbulence anisotropy increased near the walls, and the flow became more correlated in the streamwise direction. Since a very low level of elasticity was set in their simulations, they suggested yield stress is the property responsible for the flow features found.

Figure 1.8 – Contours of instantaneous spanwise vorticity in and $x - y$ plane (left) and in a $y - z$ plane (right). Re_p is fixed at 5600. The dark areas represent the instantaneous regions where the flow is not yielded. The yield stress magnitude increases from top-down.

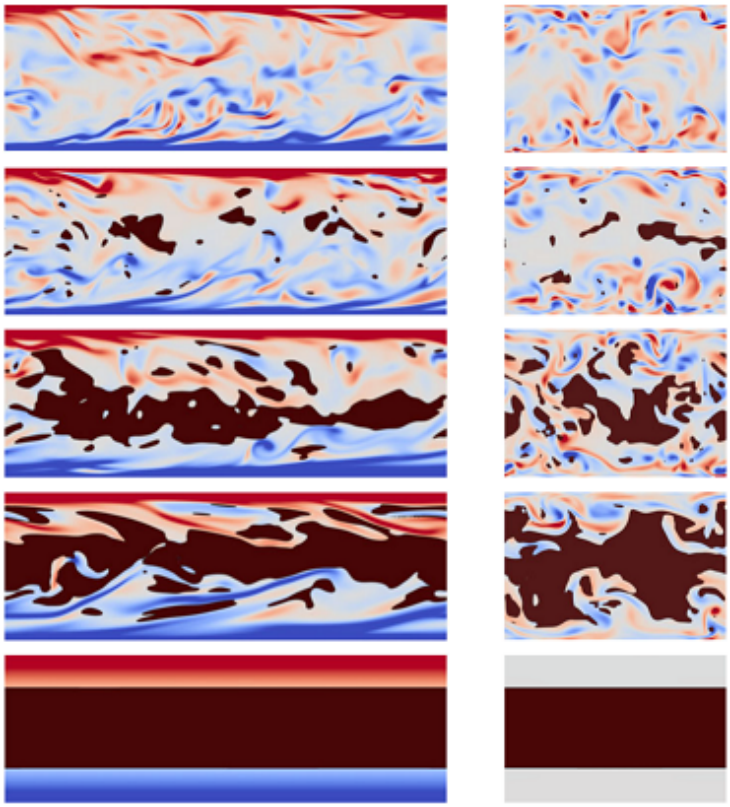

Source: Rosti et al. (2018).

1.2.4 Open Issues

From the literature review exposed above, one can notice that for viscoplastic turbulent flow there is general agreement concerning features that can be associated with shear-thinning. Since all viscoplastic materials are also shear-thinning to some extent, it is not easy to isolate yield stress effects. When it comes to particular yield stress effects, some disagreements are clear. Regarding laminar-to-turbulent transition, two distinct descriptions were identified. Peixinho et al. (2005) believe that during transition turbulent puffs alternate with quasi-laminar flow, and plug zones can be found in the latter. On the other hand, Güzel et al. (2009) argue that transition only begins after the plug zone has completely vanished.

Investigations by DNS have demonstrated disagreements with respect to the occurrence of unyielded spots in turbulent flow. Some of the main open issues in the field are listed below:

- What is the true effect of the yield stress on the friction factor curve? Do the curves for different σ_y really merge under fully turbulent flow? Is there really a local minimum in transitional flow?
- What is the physical origin and mathematical explanation of the asymmetric velocity profile? Can it be reproduced in a virtual environment?
- How does the yield stress effect on turbulence differs from shear thinning over a wide Reynolds number range?
- How may the turbulent viscous stress be modeled in averaged/filtered approaches, allowing for cost-effective industrial simulations?

These questions serve as a motivation to expand the research involvement in the field, for there is still much to be answered. Therefore, a worthwhile scientific opportunity is clearly defined. Moreover, there is also an economic opportunity, since this type of research output may be used for the improvement of industrial installations that are typically huge in size and power consumption, such as mineral transport and oil-well drilling.

1.3 Objectives

From the vision that DNS can help solving some of the open questions mentioned above, the present work is set up to develop such a tool. The following thesis is stated:

> *The lattice Boltzmann method can be formulated into an accurate, stable and efficient tool for direct numerical simulations of viscoplastic turbulent flows.*

The general objective of the present thesis is to formulate an LB scheme for the direct numerical simulation of viscoplastic turbulent flow, and subsequently make use of the method to advance the phenomena interpretation and produce industrial relevant outcomes. More specifically, the general objective is partitioned into the following goals:

1. Development of an accurate, stable and efficient LB scheme for viscoplastic simulations;
2. Scheme's validation and application for direct numerical simulation of viscoplastic turbulent flows.

For the first goal, the challenge is to set the LBM's relaxation frequency to zero in order to represent the "infinite viscosity" of the Bingham fluid, while preventing spurious stresses from spoiling numerical stability and accuracy. That way, it is not necessary to employ any viscosity regularization. Whatever implementation choices must respect the method's locality, which is a fundamental characteristic for high efficiency in parallel computing. Validation of the viscoplastic LB scheme is obtained by reproducing classical steady and transient laminar flow cases.

For the second goal, a canonical turbulent flow is solved by DNS with viscoplastic fluid. Statistically steady and developed channel flow is the configuration chosen for this purpose. Results are compared with independent DNS works, since experimental data of viscoplastic turbulent flow is not available for the channel geometry. Since the Reynolds number is constrained by hardware characteristics and time limitations, it will be kept constant. The yield stress will be subject to parametric analysis. Its range is going to the defined in further time. As of particular interest is the comparison between the present and other DNS in terms of efficiency and physical outcome.

1.4 Why LBM?

Many numerical methods have been successfully formulated for direct numerical simulations, such as finite differences, spectral element and lattice Boltzmann. A researcher interested in solving the mass and momentum balance equations has to opt for whichever method better suits him/her. Every numerical method has its advantages and disadvantages. Below a list of the most significant LBM advantages and disadvantages is offered:

- **Advantages**

    1. Most of the method's operations are fully local, which allows very efficient parallelization. As a consequence, cost-effective DNS is possible through the use of graphics processing units (GPU);
    2. The algorithm is significantly simpler than other numerical alternatives. This is an important factor for anyone looking to start from scratch, and it makes the code simpler to learn, debug and add on;
    3. The inverse of viscosity is represented by the relaxation frequency, which is an algebraic parameter within the method. This means infinite viscosity can actually be computed by setting the relaxation frequency to zero. Although it has never been tried, this is worth the effort because it could dismiss the need for viscosity regularization.

- **Disadvantages**

    1. Every numerical method has some sort of numerical instability depending on a parameter combination. In LBM, stability issues limit the practical range of velocity and viscosity. Any high Reynolds or high viscosity simulation will require some treatment for stability;
    2. LBM does not solve the macroscopic equations (Navier-Stokes) exactly. Rather, it represents them by a weakly compressible formulation. So, it is an indirect solver for the Navier-Stokes equation. When working with LBM variables, insights on errors, mass sources and boundary conditions do not come as intuitively as for macroscopic properties;
    3. The LB schemes available in the literature are discretized in Cartesian coordinates. Converting the results to cylindrical coordinates requires additional post-processing and generates interpolation errors. Additionally, up to the present date, feasible aspect ratios for non-uniform grids remain small.

The present author's evaluation is that the trade-off is positive for LBM, because there are viable remedies for many obstacles found during implementation and simulations. For instance, stability problems can be attenuated by regularization of ghost moments (not to be confused with viscosity regularization, see section 3.3), and the compressibility can be lowered to negligible levels by setting a small velocity. Add to that the fact that LBM is becoming an increasingly popular DNS tool due to its attractive numerical efficiency (TOUIL et al., 2014; GEHRKE et al., 2017; PENG et al., 2018; PENG and WANG, 2018).

1.5 Document Outline

This thesis is organized as follows: Chapter 2 presents the fundamentals of the lattice Boltzmann method, and how it can be applied to non-Newtonian or turbulent flows. Also, the Chapman-Enskog expansion is performed in order to demonstrate the macroscopic equivalence of the method. Chapter 3 presents the numerical methodology developed for stable and accurate Bingham fluid flow simulations. In Chapter 4, the validation of the present viscoplastic LB scheme is performed for steady and transient laminar flows. Chapter 5 presents results and analyses for viscoplastic turbulent flow in a channel. Finally, the main conclusions concerning this thesis are exposed in Chapter 6.

2 THEORETICAL FORMULATION

This chapter is oriented towards the lattice Boltzmann method (LBM) and its theories. The equations shown here form the basis for the viscoplastic LB scheme, detailed in the next chapter. Starting with the implications of the mesoscopic treatment in Section 2.1, the present chapter goes on to explain the forcing LBM in Section 2.2. The relation between the mesoscopic relaxation frequency and the macroscopic viscosity is deduced in Section 2.3 through the Chapman-Enskog expansion. Finally, Sections 2.4 and 2.5 show how LBM can be formulated to simulate non-Newtonian and turbulent flows, respectively.

2.1 Kinetic Theory

While the microscopic treatment tracks individual atoms or molecules and their various degrees of freedom, the macroscopic treatment averages out the atomistic picture and tracks more tangible quantities, such as density and fluid velocity. Both approaches derive from Newton's Second Law, which for the microscopic treatment results in the astoundingly expensive molecular dynamics (MD), and for the macroscopic treatment results in the non-linear partial differential Navier-Stokes equation (NSE). The NSE has been the preferred way for solving fluid flow problems in engineering because numerical methods are well established and the formulation of closure equations and boundary conditions are relatively easy. However, there is another way to approach a fluid flow problem: the mesoscopic level.

2.1.1 The Particle Distribution Function

The essence of the kinetic theory is in focusing not on individual particles, but instead, on representative collections of particles. Starting from the particle level, the relevant spatial scales are: the atom's or molecule's size ℓ_a, the mean free path (distance traveled between two successive collisions) ℓ_{mfp}, the typical scale for gradients in some macroscopic flow ℓ and the system size ℓ_S. The respective time scales are: the collision time (duration of a collision event) t_c, the mean collision time (time between two successive collisions) t_{mfp}, the convection time t_{conv} and the diffusion time t_{diff}. Figure 2.1 gives an illustrative picture of where the mesoscopic level stands. In the mesoscopic kinetic theory, the representative collections of particles evolve on timescales around the mean collision time t_{mfp}.

The fundamental variable in kinetic theory is the particle distribution function $f(\boldsymbol{x}, \boldsymbol{\xi}, t)$. Krüger et al. (2017) describe f as the density of particles with velocity $\boldsymbol{\xi} = (\xi_1, \xi_2, \xi_3)$ at position $\boldsymbol{x}$ and time t. Its dimensions are kg $\times$ m^{-3} $\times$ (m/s)$^{-3}$ = kg s^3/m^6. Macroscopic variables are obtained from moments of the particle distribution function. These moments are integrals of f over the entire velocity space. For instance, the macroscopic mass density is

$$\rho(\boldsymbol{x}, t) = \int f(\boldsymbol{x}, \boldsymbol{\xi}, t) \mathrm{d}^3\xi \tag{2.1}$$

and the macroscopic momentum density is

$$\rho(\boldsymbol{x}, t)\boldsymbol{u}(\boldsymbol{x}, t) = \int \boldsymbol{\xi} f(\boldsymbol{x}, \boldsymbol{\xi}, t) \mathrm{d}^3\xi \tag{2.2}$$

Figure 2.1 – Hierarchy of length and time scales in typical fluid dynamics problems.

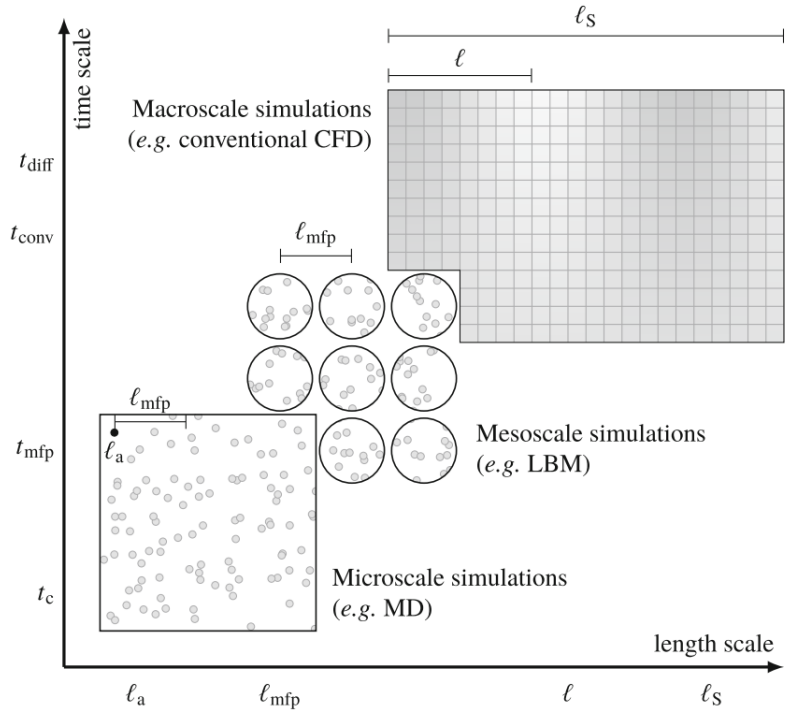

Source: Krüger et al. (2017).

Considering an isolated system left alone for sufficiently long time, it eventually reaches thermodynamic equilibrium, which is isotropic in velocity space around $\boldsymbol{\xi} = \boldsymbol{u}$. An equilibrium distribution function $f^{\mathrm{eq}}(\boldsymbol{x}, \boldsymbol{\xi}, t)$ is defined to represent this state. James C. Maxwell first came up with the derivation of an equilibrium distribution function, and it was later proven to be unique through the statistical mechanics approach of Ludwig E. Boltzmann. In a reference frame moving with speed $\boldsymbol{u}$, the Maxwell-Boltzmann distribution reads

$$f^{\mathrm{eq}}(\boldsymbol{x}, |\boldsymbol{v}|, t) = \rho \left(\frac{1}{2\pi RT} \right)^{3/2} \mathrm{e}^{-\frac{|\boldsymbol{v}|^2}{2RT}} \tag{2.3}$$

where $\boldsymbol{v}(\boldsymbol{x}, t) = \boldsymbol{\xi}(\boldsymbol{x}, t) - \boldsymbol{u}(\boldsymbol{x}, t)$ is the relative velocity, i.e., the particle's velocity deviation from the local mean velocity. A thorough derivation of the above equation is given in (GOMBOSI and GOMBOSI, 1994).

2.1.2 The Boltzmann Equation

In order to find an evolution equation for f, one must first observe its total derivative with respect to time t:

$$\frac{\mathrm{d}f}{\mathrm{d}t} = \left(\frac{\partial f}{\partial t} \right) \frac{\mathrm{d}t}{\mathrm{d}t} + \left(\frac{\partial f}{\partial x_\alpha} \right) \frac{\mathrm{d}x_\alpha}{\mathrm{d}t} + \left(\frac{\partial f}{\partial \xi_\alpha} \right) \frac{\mathrm{d}\xi_\alpha}{\mathrm{d}t} \tag{2.4}$$

where the terms on the right-hand side are $\mathrm{d}t/\mathrm{d}t = 1$, $\mathrm{d}x_\alpha/\mathrm{d}t = \xi_\alpha$ and $\mathrm{d}\xi_\alpha/\mathrm{d}t = F_\alpha/\rho$ (specific body force). Einstein notation, which implies summation over repeated indices, was used in the above equation. In the course of this work, the bold symbol is used to represent vectors and tensors, and

Einstein notation is used for operations with components (the components of tensor $\boldsymbol{A}$ are denoted by $A_{\alpha\beta}$).

The total derivative of f is treated as a source term, called collision operator $\mathrm{d}f/\mathrm{d}t = \Omega(f)$, and the result is known as the Boltzmann equation:

$$\frac{\partial f}{\partial t} + \xi_\alpha \frac{\partial f}{\partial x_\alpha} + \frac{F_\alpha}{\rho}\frac{\partial f}{\partial \xi_\alpha} = \Omega(f) \tag{2.5}$$

The simplest collision operator available was proposed in (BHATNAGAR et al., 1954) and is known as BGK after its authors (Bhatnagar, Gross and Krook). It is also called single-relaxation-time since it makes f evolves towards f^{eq} with only one temporal parameter: $\Omega(f) = -(f - f^{\mathrm{eq}})/\tau$. The relaxation time τ is the most crucial parameter in LBM simulations because it is directly related to the fluid's viscosity, as will be demonstrated in Section 2.3. It is worth mentioning that, although the Boltzmann equation and the equilibrium distribution function were derived for an ideal dilute gas, it is possible to represent liquids with the Boltzmann equation, by tuning τ to an appropriate value. Even non-Newtonian fluids can be correctly represented with the lattice Boltzmann method.

2.2 Lattice Boltzmann Method

The lattice Boltzmann method consists in solving the Boltzmann equation in the discrete phase space. Discretization in the velocity space leads to the so-called velocity sets and discrete-velocity particle distribution functions. Discretization in space and time generates explicit equations for the discrete-velocity particle distribution functions for a finite number of points in space and time. The moments of the discrete-velocity particle distribution functions lead back to the macroscopic quantities. Below, the step-by-step of the lattice Boltzmann method will be briefly explained.

Figure 2.2 – Common two- and three-dimensional velocity sets (lattices) for LBM. Rest velocities $\boldsymbol{c}_0 = \mathbf{0}$ are not shown. All sides have length $2\Delta x$.

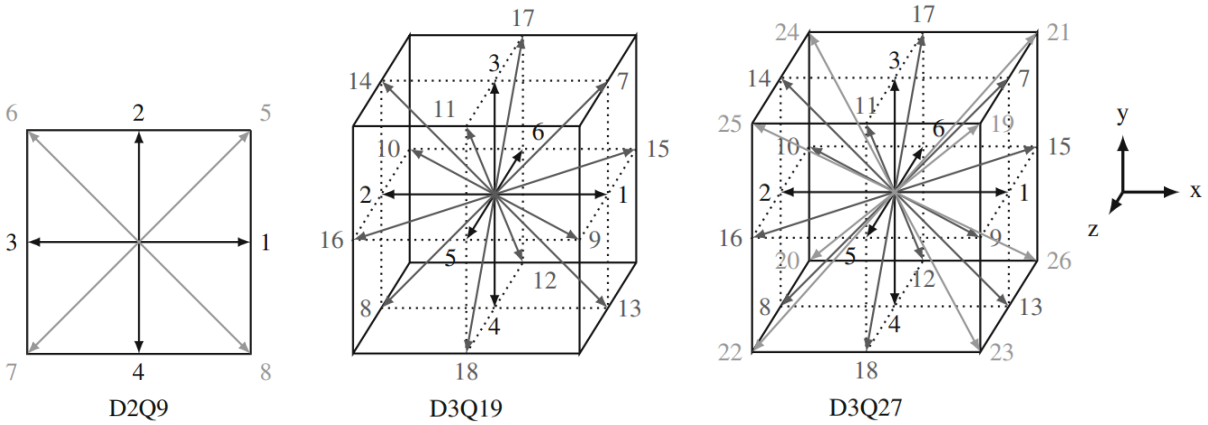

Source: adapted from Krüger et al. (2017).

2.2.1 Velocity Discretization

The discretization in velocity space enables one to reduce the continuous 3D velocity space to a small number of discrete velocities without undermining the resulting macroscopic behavior. A velocity

set, or lattice, for LBM is defined by velocity vectors $\{\boldsymbol{c}_i\}$ and their corresponding weights $\{w_i\}$. Also, from a given velocity set, a scaling factor c_s is defined. For isothermal models, c_s represents the speed of sound. In the present work, the naming of the velocity sets is given by the nomenclature $\mathrm{D}d\mathrm{Q}q$, where d is the number of spatial dimensions and q is the number of discrete velocities (including the rest velocity $\boldsymbol{c}_0 = \mathbf{0}$). The commonly used D2Q9, D3Q19 and D3Q27 lattices are illustrated in Figure 2.2. Their velocity vectors and weights are seen in Table 2.1.

Table 2.1 – Properties of the velocity sets (lattices) exhibited in Figure 2.2. The speed of sound for all of these velocity sets is $c_\mathrm{s} = 1/\sqrt{3}$.

Name	Velocity vectors ($\boldsymbol{c}_i$)	Length ($\lvert\boldsymbol{c}_i\rvert$)	Weight (w_i)
D2Q9	(0, 0)	0	4/9
	(±1, 0); (0, ±1)	1	1/9
	(±1, ±1)	$\sqrt{2}$	1/36
D3Q19	(0, 0, 0)	0	1/3
	(±1, 0, 0); (0, ±1, 0); (0, 0, ±1)	1	1/18
	(±1, ±1, ±1)	$\sqrt{2}$	1/36
D3Q27	(0, 0, 0)	0	8/27
	(±1, 0, 0); (0, ±1, 0); (0, 0, ±1)	1	2/27
	(±1, ±1, 0); (±1, 0, ±1); (0, ±1, ±1)	$\sqrt{2}$	1/54
	(±1, ±1, ±1)	$\sqrt{3}$	1/216

Source: Krüger et al. (2017).

A mathematically sound procedure for the velocity space discretization is a truncated Hermite expansion. A full description is found in (MARTYS et al., 1998) and will be left out because the derivation is extensive and it is not part of the present thesis' scope. The discrete-velocity Boltzmann equation is

$$\frac{\partial f_i}{\partial t} + c_{i\alpha}\frac{\partial f_i}{\partial x_\alpha} = \Omega_i + F_i \tag{2.6}$$

where i ranges from 0 to $q-1$. The discrete-velocity particle distribution functions f_i are commonly called *populations* in LBM literature. The velocity space discretization is also performed for f^eq, Ω and F_α. The second-order truncated force term F_i is (GUO et al., 2002)

$$F_i = w_i\left[\frac{c_{i\alpha}}{c_\mathrm{s}^2} + \frac{\left(c_{i\alpha}c_{i\beta} - c_\mathrm{s}^2\delta_{\alpha\beta}\right)u_\beta}{c_\mathrm{s}^4}\right]F_\alpha \tag{2.7}$$

and its first three velocity moments, corresponding to the integrals in velocity space, are

$$\sum_i F_i = 0 \tag{2.8a}$$

$$\sum_i F_i c_{i\alpha} = F_\alpha \tag{2.8b}$$

$$\sum_i F_i c_{i\alpha}c_{i\beta} = F_\alpha u_\beta + F_\beta u_\alpha \tag{2.8c}$$

Accordingly, the second-order truncated discrete-velocity equilibrium distribution function is

$$f_i^\mathrm{eq} = w_i\rho\left[1 + \frac{c_{i\alpha}u_\alpha}{c_\mathrm{s}^2} + \frac{u_\alpha u_\beta\left(c_{i\alpha}c_{i\beta} - c_\mathrm{s}^2\delta_{\alpha\beta}\right)}{2c_\mathrm{s}^4}\right] \tag{2.9}$$

and its velocity moments are

$$\sum_i f_i^{\mathrm{eq}} = \rho \tag{2.10a}$$

$$\sum_i f_i^{\mathrm{eq}} c_{i\alpha} = \rho u_\alpha \tag{2.10b}$$

$$\sum_i f_i^{\mathrm{eq}} c_{i\alpha} c_{i\beta} = \rho u_\alpha u_\beta + \rho c_s^2 \delta_{\alpha\beta} \equiv \Pi_{\alpha\beta}^{\mathrm{eq}} \tag{2.10c}$$

$$\sum_i f_i^{\mathrm{eq}} c_{i\alpha} c_{i\beta} c_{i\gamma} = \rho c_s^2 \left(u_\alpha \delta_{\beta\gamma} + u_\beta \delta_{\alpha\gamma} + u_\gamma \delta_{\alpha\beta}\right) \equiv \Pi_{\alpha\beta\gamma}^{\mathrm{eq}} \tag{2.10d}$$

In Equations 2.10c and 2.10d the symbols $\Pi_{\alpha\beta}^{\mathrm{eq}}$ and $\Pi_{\alpha\beta\gamma}^{\mathrm{eq}}$ are shorthand tensor notations for the second and third velocity moments of f_i^{eq}, respectively.

2.2.2 Space and Time Discretization

The discrete-velocity Boltzmann equation (Eq. 2.6) can be discretized in time and space by the Method of Characteristics using ζ as a trajectory parameter (KRÜGER et al., 2017). The total derivative of f_i with respect to ζ is

$$\frac{\mathrm{d}f_i}{\mathrm{d}\zeta} = \left(\frac{\partial f_i}{\partial t}\right)\frac{\mathrm{d}t}{\mathrm{d}\zeta} + \left(\frac{\partial f_i}{\partial x_\alpha}\right)\frac{\mathrm{d}x_\alpha}{\mathrm{d}\zeta} \tag{2.11}$$

Imposing $\mathrm{d}\zeta/\mathrm{d}t = 1$ and $\mathrm{d}\zeta/\mathrm{d}x_\alpha = c_{i\alpha}^{-1}$ as conditions, the right-hand side of Equation 2.11 becomes equal to $\Omega_i\left(\boldsymbol{x}(\zeta), t(\zeta)\right) + F_i\left(\boldsymbol{x}(\zeta), t(\zeta)\right)$ (see Eq. 2.6). The integration of $\mathrm{d}f_i/\mathrm{d}\zeta$ along the trajectory ζ has an exact solution:

$$\int_t^{t+\Delta t} \frac{\mathrm{d}f_i}{\mathrm{d}\zeta}\mathrm{d}\zeta = f_i(\boldsymbol{x} + \boldsymbol{c}_i\Delta t, t + \Delta t) - f_i(\boldsymbol{x}, t) \tag{2.12}$$

The remaining problem is to solve the integral

$$\int_t^{t+\Delta t} \left(\Omega_i + F_i\right)\mathrm{d}\zeta \tag{2.13}$$

This integral can be solved in many ways. In the present work, we follow the strategy of He et al. (1998) which consists of a second-order trapezoidal integration followed by a clever change of variables:

$$\bar{f}_i = f_i - \frac{\left(\Omega_i + F_i\right)\Delta t}{2} \tag{2.14}$$

Using the discrete results of the integrals 2.12 and 2.13 one finally gets to the so-called *lattice Boltzmann equation* (LBE)

$$\bar{f}_i(\boldsymbol{x} + \boldsymbol{c}_i\Delta t, t + \Delta t) - \bar{f}_i(\boldsymbol{x}, t) = \left[\Omega_i(\boldsymbol{x}, t) + F_i(\boldsymbol{x}, t)\right]\Delta t \tag{2.15}$$

It must be pointed out that the LBE may take several forms depending on the choice for the discretization method of the integral 2.13 and the presence (or absence) of the force term. The BGK collision operator may be combined with LBE to result in the second-order LBGK with force term

$$\bar{f}_i(\boldsymbol{x}+\boldsymbol{c}_i\Delta t, t+\Delta t) - \bar{f}_i(\boldsymbol{x},t) = -\frac{\Delta t}{\bar{\tau}}\left[\bar{f}_i(\boldsymbol{x},t) - \bar{f}_i^{\mathrm{eq}}(\boldsymbol{x},t)\right] + \left(1-\frac{\Delta t}{2\bar{\tau}}\right)F_i(\boldsymbol{x},t)\Delta t \tag{2.16}$$

with $\bar{\tau} = \tau + \Delta t/2$.

2.2.3 Macroscopic Moments

As well as the continuous integrals of Equations 2.1 and 2.2 recovered macroscopic quantities ρ and $\rho\boldsymbol{u}$, one may compute discrete moments of $\bar{f}_i$. The first, second and third velocity moments of $\bar{f}_i$ are, respectively (SILVA and SEMIAO, 2012)

$$\rho = \sum_i \bar{f}_i + \frac{\Delta t}{2}\sum_i F_i \tag{2.17a}$$

$$\rho u_\alpha = \sum_i \bar{f}_i c_{i\alpha} + \frac{\Delta t}{2}\sum_i F_i c_{i\alpha} \tag{2.17b}$$

$$\Pi_{\alpha\beta} = \left(1-\frac{\Delta t}{2\bar{\tau}}\right)\sum_i \bar{f}_i c_{i\alpha}c_{i\beta} + \frac{\Delta t}{2\bar{\tau}}\sum_i \bar{f}_i^{\mathrm{eq}} c_{i\alpha}c_{i\beta} + \frac{\Delta t}{2}\left(1-\frac{\Delta t}{2\bar{\tau}}\right)\sum_i F_i c_{i\alpha}c_{i\beta} \tag{2.17c}$$

The first and second moments correspond to density and momentum, respectively. The third one is related to the inertial and viscous forces, and it was intentionally defined this way for reasons that will be clear in the next section. To make sense of what it means, it is necessary to know the macroscopic correspondence of the LBM variables. Equations 2.17 can be further simplified by considering the moments of the force term (Equations 2.8):

$$\rho = \sum_i \bar{f}_i \tag{2.18a}$$

$$\rho u_\alpha = \sum_i \bar{f}_i c_{i\alpha} + \frac{\Delta t}{2}F_\alpha \tag{2.18b}$$

$$\Pi_{\alpha\beta} = \left(1-\frac{\Delta t}{2\bar{\tau}}\right)\sum_i \bar{f}_i c_{i\alpha}c_{i\beta} + \frac{\Delta t}{2\bar{\tau}}\sum_i \bar{f}_i^{\mathrm{eq}} c_{i\alpha}c_{i\beta} + \frac{\Delta t}{2}\left(1-\frac{\Delta t}{2\bar{\tau}}\right)\left(F_\alpha u_\beta + F_\beta u_\alpha\right) \tag{2.18c}$$

From this point on, the bar symbol will be dropped for simplicity.

2.3 Chapman-Enskog Expansion

Now that the LBE is known, it is opportune to understand how it can represent the macroscopic momentum balance equation, which for Newtonian fluids is the Navier-Stokes equation (NSE). The most common way to do so is through the Chapman-Enskog analysis. It begins with the notion that when $f \approx f^{\mathrm{eq}}$, the Boltzmann equation results in the Euler equation of motion (KRÜGER et al., 2017). Therefore, the *non-equilibrium* part $f^{\mathrm{neq}} = f - f^{\mathrm{eq}}$ must be responsible for viscous forces. As a

way to determine f^{neq}, the Chapman-Enskog analysis enters as a perturbation expansion of f_i around the equilibrium distribution f^{eq} with an expansion parameter ϵ (originally devised to be the Knudsen number[1] Kn):

$$f_i = f_i^{\mathrm{eq}} + \epsilon f_i^{(1)} + \epsilon^2 f_i^{(2)} + ... \tag{2.19}$$

A common ansatz of the Chapman-Enskog procedure is to consider only the two lowest orders in ϵ (up to ϵ^1) to find the macroscopic momentum balance equation. A scale of order $\mathcal{O}(\epsilon)$ for the force term is sufficient in the present analysis (BUICK and GREATED, 2000), which implies $F_i = \epsilon F_i^{(1)}$. Another important assumption comes from the observation of the first two moments of f_i^{eq} and f_i (Equations 2.10 and 2.18):

$$\sum_i f_i^{(1)} = -\frac{\Delta t}{2} \sum_i F_i^{(1)} \tag{2.20a}$$

$$\sum_i f_i^{(1)} c_{i\alpha} = -\frac{\Delta t}{2} \sum_i F_i^{(1)} c_{i\alpha} \tag{2.20b}$$

Thus, the higher-order solvability conditions are (SILVA and SEMIAO, 2012)

$$\sum_i f_i^{(\mathrm{k})} = 0 \tag{2.21a}$$

$$\sum_i f_i^{(\mathrm{k})} c_{i\alpha} = 0 \tag{2.21b}$$

with $k \geq 2$.

A Taylor expansion can be written such as

$$f_i(\boldsymbol{x} + \boldsymbol{c}_i \Delta t, t + \Delta t) - f_i(\boldsymbol{x}, t) = \sum_{n=1}^{\infty} \frac{(\Delta t)^n}{n!} \left(\partial_t + c_{i\alpha}\partial_\alpha\right)^n f_i(\boldsymbol{x}, t) \tag{2.22}$$

where the contracted derivative notation $\partial_t() = \partial()/\partial t$ and $\partial_\alpha() = \partial()/\partial x_\alpha$ was employed. Applying the above relation to the LBGK (Equation 2.16), one gets

$$\Delta t \left(\partial_t + c_{i\alpha}\partial_\alpha\right) f_i + \frac{(\Delta t)^2}{2} \left(\partial_t + c_{i\alpha}\partial_\alpha\right)^2 f_i = -\frac{\Delta t}{\tau} \left(f_i - f_i^{\mathrm{eq}}\right) + \left(1 - \frac{\Delta t}{2\tau}\right) F_i \Delta t \tag{2.23}$$

where $f_i = f_i(\boldsymbol{x}, t)$. The terms with order superior to $\mathcal{O}(\Delta t^2)$ were left out since they exceed the discretization order of the LBGK. By subtracting $(\Delta t/2)\left(\partial_t + c_{i\alpha}\partial_\alpha\right)$ applied to the equation itself, the second-order derivative can be eliminated. After some algebra, it results in

$$\left(\partial_t + c_{i\alpha}\partial_\alpha\right) \left[f_i - \frac{\Delta t}{2\tau} \left(f_i - f_i^{\mathrm{eq}}\right) + \frac{\Delta t}{2} \left(1 - \frac{\Delta t}{2\tau}\right) F_i\right] = -\frac{1}{\tau} \left(f_i - f_i^{\mathrm{eq}}\right) + \left(1 - \frac{\Delta t}{2\tau}\right) F_i \tag{2.24}$$

[1] The Knudsen number is defined as $Kn = \ell_{\mathrm{mfp}}/\ell$. For $Kn < 0.1$, the macroscopic approach (NSE) can be used (LAURENDEAU, 2005). Otherwise, the microscopic motions have magnitudes close to the system size, and the continuum assumption does not hold.

The separation step consists in isolating terms of same order in ϵ. Before it is possible, a multiple-scale separation of the derivatives is needed. For the spatial derivative, $\partial_\alpha = \epsilon\partial_\alpha^{(1)}$, and for the temporal derivative, $\partial_t = \epsilon\partial_t^{(1)} + \epsilon^2\partial_t^{(2)}$. The first and second terms of ∂_t correspond to convective and diffusive time scales, respectively. Unfolding Equation 2.24 based on the multiple-scale derivatives and f_i, the ϵ-perturbed equations are found to be

$$\mathcal{O}(\epsilon^1): \qquad \left(\partial_t^{(1)} + c_{i\alpha}\partial_\alpha^{(1)}\right) f_i^{\mathrm{eq}} - \left(1 - \frac{\Delta t}{2\tau}\right) F_i^{(1)} = -\frac{1}{\tau} f_i^{(1)} \tag{2.25a}$$

$$\mathcal{O}(\epsilon^2): \qquad \partial_t^{(2)} f_i^{\mathrm{eq}} + \left(\partial_t^{(1)} + c_{i\alpha}\partial_\alpha^{(1)}\right)\left[\left(1 - \frac{\Delta t}{2\tau}\right)\left(f_i^{(1)} + \frac{\Delta t}{2} F_i^{(1)}\right)\right] = -\frac{1}{\tau} f_i^{(2)} \tag{2.25b}$$

The 0*th* and 1*st* velocity moments of the perturbed equations are obtained by multiplying Equation 2.25 by 1 and $c_{i\beta}$, respectively, and then summing over i. For the $\mathcal{O}(\epsilon^1)$ equation they are:

$$\partial_t^{(1)}\rho + \partial_\alpha^{(1)}\left(\rho u_\alpha\right) = 0 \tag{2.26a}$$

$$\partial_t^{(1)}\left(\rho u_\alpha\right) + \partial_\alpha^{(1)}\Pi_{\alpha\beta}^{\mathrm{eq}} = \sum_i F_i^{(1)} c_{i\alpha} \tag{2.26b}$$

Also for the $\mathcal{O}(\epsilon^1)$ equation, the second velocity moment yields an important expression, which is

$$\Pi_{\alpha\beta}^{(1)} = -\left(\tau - \frac{\Delta t}{2}\right)\left(\partial_t^{(1)}\Pi_{\alpha\beta}^{\mathrm{eq}} + \partial_\gamma^{(1)}\Pi_{\alpha\beta\gamma}^{\mathrm{eq}} - \sum_i F_i^{(1)} c_{i\alpha} c_{i\beta}\right) \tag{2.27}$$

The 0*th* and 1*st* velocity moments of the $\mathcal{O}(\epsilon^2)$ equation are

$$\partial_t^{(2)}\rho = 0 \tag{2.28a}$$

$$\partial_t^{(2)}\left(\rho u_\alpha\right) + \partial_\beta^{(1)}\Pi_{\alpha\beta}^{(1)} = 0 \tag{2.28b}$$

Recombining the $\mathcal{O}(\epsilon^1)$ terms, one gets

$$\partial_t\rho + \partial_\alpha\left(\rho u_\alpha\right) = 0 \tag{2.29}$$

which is precisely the mass conservation equation for compressible and transient flow, obtained through continuum mechanics (WHITE, 2011). Recombining the $\mathcal{O}(\epsilon^2)$ terms yields

$$\partial_t\left(\rho u_\alpha\right) + \partial_\beta\left(\Pi_{\alpha\beta}^{\mathrm{eq}} + \epsilon\Pi_{\alpha\beta}^{(1)}\right) = F_\alpha \tag{2.30}$$

The above equation is supposed to represent the macroscopic momentum balance. Therefore, it is necessary to make sense of its tensorial terms. The spatial derivative to $\Pi_{\alpha\beta}^{\mathrm{eq}}$ of Equation 2.10c is

$$\partial_\beta\Pi_{\alpha\beta}^{\mathrm{eq}} = \partial_\beta\left(\rho u_\alpha u_\beta\right) + \partial_\beta\left(\rho c_s^2\delta_{\alpha\beta}\right) \tag{2.31}$$

which means that the equilibrium tensor represents the inertial and pressure forces of the momentum balance, given a state equation for the thermodynamic pressure $p = c_s^2\rho$. Consequently, the $\Pi_{\alpha\beta}^{(1)}$ term

can only be associated with the viscous forces. The path to solving $\Pi^{(1)}_{\alpha\beta}$ starts from Equation 2.27. The spatial derivative of $\Pi^{\mathrm{eq}}_{\alpha\beta\gamma}$ is straightforward (see Equation 2.10d):

$$\partial^{(1)}_{\gamma}\Pi^{\mathrm{eq}}_{\alpha\beta\gamma} = c_s^2\left[\partial^{(1)}_{\alpha}\left(\rho u_\beta\right) + \partial^{(1)}_{\beta}\left(\rho u_\alpha\right) + \delta_{\alpha\beta}\partial^{(1)}_{\gamma}\left(\rho u_\gamma\right)\right] \tag{2.32}$$

Next, the temporal derivative $\partial^{(1)}_t\Pi^{\mathrm{eq}}_{\alpha\beta} = \partial^{(1)}_t(\rho u_\alpha u_\beta) + \partial^{(1)}_t(\rho c_s^2\delta_{\alpha\beta})$ needs to be determined. Two insights are invoked in order to do so. The first is a corollary of the product rule:

$$\partial_*(abc) = a\partial_*(bc) + b\partial_*(ac) - ab\partial_* c \tag{2.33}$$

and the second is the use of Equation 2.26b. Together, these two ideas produce

$$\partial^{(1)}_t\Pi^{\mathrm{eq}}_{\alpha\beta} = u_\alpha\sum_i F^{(1)}_i c_{i\beta} + u_\beta\sum_i F^{(1)}_i c_{i\alpha} - c_s^2\left[u_\alpha\partial^{(1)}_\beta\rho + u_\beta\partial^{(1)}_\alpha\rho + \delta_{\alpha\beta}\partial^{(1)}_\gamma\left(\rho u_\gamma\right)\right] \tag{2.34}$$

Inputting Equations 2.32 and 2.34 into Equation 2.27, and distributing the parameter ϵ to recombine the expanded terms:

$$\epsilon\Pi^{(1)}_{\alpha\beta} = -\left(\tau - \frac{\Delta t}{2}\right)\rho c_s^2\left(\partial_\alpha u_\beta + \partial_\beta u_\alpha\right) \tag{2.35}$$

A parameter of the form

$$\eta = \rho c_s^2\left(\tau - \frac{\Delta t}{2}\right) \tag{2.36}$$

may be defined. Making use of it and rewriting Equation 2.30 yields

$$\partial_t\left(\rho u_\alpha\right) + \partial_\beta\left(\rho u_\alpha u_\beta\right) = -\partial_\alpha p + \partial_\beta\left[\eta\left(\partial_\alpha u_\beta + \partial_\beta u_\alpha\right)\right] + F_\alpha \tag{2.37}$$

and this is the momentum conservation equation for a Generalized Newtonian fluid with viscosity η (BIRD et al., 1987). One may notice that at no point in the above formulation was τ considered constant with respect to time or space. Another important observation is that the extensional stress, produced by density changes, is not represented by Equation 2.37. As a matter of fact, the generalized Newtonian fluid does not predict such stress, for it was inspired in the incompressible Newtonian constitutive equation (MORRISON, 2001).

In order to approach the limit of incompressible flow, the Mach number $Ma = U/c_s$, where U is a typical fluid velocity scale, has to be made much smaller than the unity (Anderson JR, 2010). The above LBM formulation serves this exact purpose, since terms of order $\mathcal{O}(u^3)$ arise in the momentum equations as a consequence of insufficient Hermitian representation. This is why the LBM is often referred to as a *weakly compressible* NSE solver. Throughout this work, all $\mathcal{O}(u^3)$ terms were omitted in the Chapman-Enskog expansion for clarity. Avoiding these spurious terms and solving high Ma flows would require higher-order lattices, like the D2V17 (PHILIPPI et al., 2006).

2.4 Non-Newtonian Fluid Flow with LBM

The previous section demonstrated how the mesoscopic relaxation time τ is related to the macroscopic balance equations through Equation 2.36. It was demonstrated that τ is directly proportional to

the viscosity η. In this section, the fundamentals of viscoplastic fluid mechanics will be discussed, as well as the existing schemes in LBM.

2.4.1 Viscoplastic Fluid Mechanics

A Newtonian fluid is one that has a constant dynamic viscosity μ with respect to shear or elongational rate, even though it can vary with temperature or pressure. The extra stress equation for an incompressible flow is (MORRISON, 2001)

$$\sigma_{\alpha\beta} = \mu\dot{\gamma}_{\alpha\beta} \tag{2.38}$$

where $\boldsymbol{\sigma}$ is the extra stress tensor and $\dot{\boldsymbol{\gamma}} = \nabla\boldsymbol{u} + (\nabla\boldsymbol{u})^T$ is the rate-of-strain tensor. Such fluids cannot sustain stress, i.e., the smallest stress will trigger continuous motion. On the other hand, a viscoplastic fluid can sustain stress without continuous deformation through a property called *yield stress*[2]. The generalized Newtonian fluid (GNF) model is able to represent this and many other non-Newtonian characteristics by considering η as a function of the magnitude of $\dot{\boldsymbol{\gamma}}$ (BIRD et al., 1987):

$$\sigma_{\alpha\beta} = \eta\left(|\dot{\boldsymbol{\gamma}}|\right)\dot{\gamma}_{\alpha\beta} \tag{2.39}$$

The simplest constitutive equation that exhibits the ability to sustain stress is the Bingham model (BINGHAM, 1922). For three-dimensional flow, it is defined as

$$\begin{cases} \eta \to \infty & , |\boldsymbol{\sigma}| \leq \sigma_y \\ \eta = \eta_p + \dfrac{\sigma_y}{|\dot{\boldsymbol{\gamma}}|} & , |\boldsymbol{\sigma}| > \sigma_y \end{cases} \tag{2.40}$$

where η_p is the plastic viscosity, corresponding to the viscosity at very high shear rates, σ_y is the yield stress, and $|\boldsymbol{A}| = \sqrt{(\boldsymbol{A} : \boldsymbol{A})/2}$ is the second invariant (magnitude) of a tensor. The key computational challenge when it comes to viscoplastic flow is to track the yield surfaces that separate plugs from yielded regions (BALMFORTH et al., 2014). The most common approach to treat the singularity in Equation 2.40 is to regularize the viscosity. The solid behavior is replaced by a very viscous fluid, thereby eliminating any yield surfaces. As a side note, it must be kept in mind that the term *regularization* has two different meanings in the present work: regularization of the viscosity and regularization of ghost populations of the LBM (see Section 3.3). In practice, viscosity regularization approaches result in fairly good velocity field, but their capacity to obtain precise yield surface shape and correct fluid dynamic (and static) stability limits for a wide variety of flows is limited (FRIGAARD and NOUAR, 2005).

2.4.2 Existing Schemes

Several articles have been published concerning LBM of Bingham fluids. The immediate and natural solution is to make the relaxation time vary in space by combining Equations 2.36 and 2.40. However,

[2] There is a debate on whether the yield stress exists or not. Barnes and Walters (1985) argument in their controversial article that with enough measurement accuracy, no yield stress would be observable. Regardless of this debate, in many applications the timescale is low enough so that the consideration of a yield stress is fine and, more importantly, practical.

this requires τ to be truncated at some relatively high value to avoid disastrous instabilities. This corresponds to the usual viscosity regularization. In the works (GINZBURG and STEINER, 2002; WANG and HO, 2008; TANG et al., 2011; OHTA et al., 2011; GRASINGER et al., 2018) Papanastasiou's regularization was employed (PAPANASTASIOU, 1987), while in the works (PRASHANT and DERKSEN, 2011; XIE et al., 2016; KHABAZI et al., 2016) a bi-viscosity model was applied. None of these authors quantified their errors against exact solutions though, except for Grasinger et al. (2018). Also, most of the above works did not release any stability guidelines, so their safe ranges of relaxation time are unclear. Grasinger et al. (2018) compared both single- and multiple-relaxation-time (MRT) collision operators and tested the entropic filtering as a means to obtain numerical stability. These authors found for parallel plates Poiseuille flow with a Bingham number near 0.25 (as defined in Section 4.1.1) a normalized quadratic error of 1×10^{-1} for $N_y = 64$ (nodes in the normal direction) and 6×10^{-2} for $N_y = 128$, thus, incompatible with the second-order decay of the LBM. In their MRT implementation, they obtained a normalized quadratic error of 3×10^{-3} for $N_y = 64$, which is notably low for this resolution. Strangely, refining the resolution caused the error to increase. The abnormal error behavior experienced in Grasinger's work was not related to accuracy issues of the LBM, but to instabilities caused by the elevated relaxation time.

In the works of Vikhansky (2008) and Vikhansky (2012) it has been successfully demonstrated that LBM can reproduce viscoplastic behavior while dismissing any type of viscosity regularization. He opted for an alternative formulation instead of the standard LBM and built the collision operator according to Ladd (1994), in such a way that an implicit tensorial equation dictated the relation between shear rate and shear stress. Therefore, some inner iterations had to be performed within each time-step to satisfy the fluid's constitutive equation. Vikhansky (2008) presented results for two-dimensional parallel plates Poiseuille flow and flow through a periodic cylinder's array, and three-dimensional squared duct Poiseuille flow. The outcome was qualitatively good in comparison to reference results from the literature. However, there are some indications that his method did not follow the second-order of error convergence $\mathcal{O}(\Delta x^2)$. As pointed out by Regulski et al. (2016), spurious Burnett stresses are present in Vikhansky's scheme, which introduces transversal currents to the flow. Actually, these "ghost" stresses are also present in standard LB schemes. More important than accuracy itself, they may expressively compromise numerical stability.

Considering this brief literature review, it is clear that there are still barriers for fast and stable calculations of the exact Bingham model. These characteristics can be established by a more standard approach of the LBM. The LB scheme formulated in the present thesis is based on two aspects. The first comes from the observation that in LBM the relaxation frequency, corresponding to the inverse of the relaxation time, can be set to zero without causing any algebraic indetermination. Instabilities are known to inflict on LBM when the relaxation frequency is too high (approaching 2) or too low (under 0.5). However, for viscoplastic simulation, an extremely low (zero) relaxation frequency is needed. Moreover, to reach high Reynolds numbers, the scheme would also require convergence with high relaxation frequency. To circumvent this, the second aspect of the present LB scheme is to make use of the so-called regularization of ghost moments for the elimination of Burnett stresses. Details of this procedure are given in Section 3.3.

2.5 Turbulent Flow With LBM

The concept of direct numerical simulation (DNS) is quite straightforward. It consists in solving the macroscopic balance equations in a grid fine enough to capture the smallest flow features. The smallest grid spacing must be of the order of the smallest turbulent eddies, while the time step must follow some numerical stability principle. So, in a sense, DNS do not require anything more than the mass and momentum solvers, because there is no closure model to deal with. In Chapter 5, details of grid sizing and data treatment are given. For now, it is opportune to explain what is the statistical approach to turbulence and to give a brief review of the LBM as a DNS tool.

2.5.1 Statistical Approach

Suppose a large tank of a fluid undergoing turbulent motion. If a probe is positioned in a point A (Fig. 2.3a), the velocity component recorded would exhibit a random signal. Now, suppose this experiment is repeated many times. Even though the experiments are very carefully conducted, minute variations in the initial conditions will cause the signals of the many experiments to seem completely different. When the velocity values of all realizations are averaged for each time t, the *ensemble average* $\langle(\sim)_\mathrm{A}\rangle$ is obtained (Fig. 2.3b). If one were to repeat the same experiment anytime later, the ensemble average would be the same. Although the detailed properties of the velocity component seem to be highly disorganized and unpredictable, its statistical properties are reproducible (DAVIDSON, 2015). Therefore, the study of turbulence is largely developed in statistical terms.

Figure 2.3 – Decaying turbulence in a tank. (a) Illustration of the turbulent eddies and probe location. (b) Single realization signal and ensemble average.

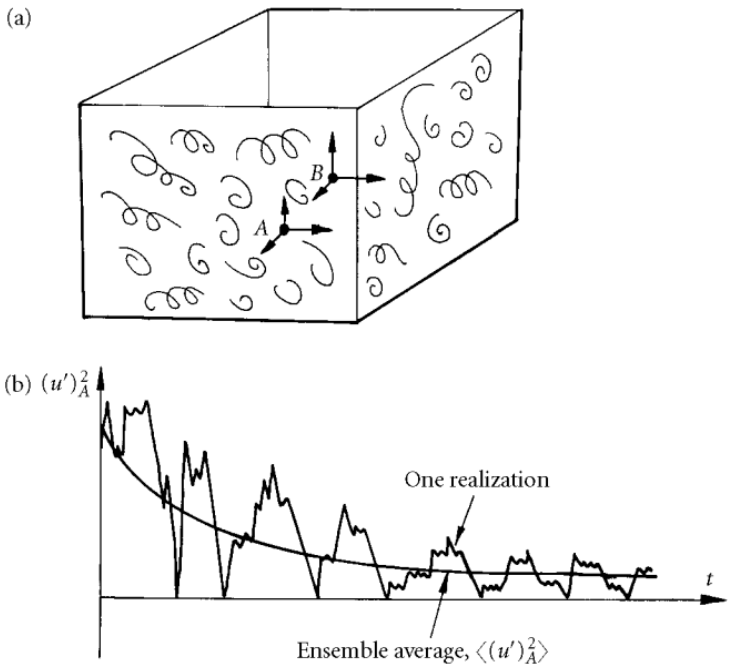

Source: Davidson (2015).

There are other forms of averaging. The time average $\overline{(\sim)}_\mathrm{A}$ consists in averaging the velocity component measured in point A in a single realization. In statistically steady flows, such as the turbulent pipe flow, the ensemble and time averages are equal. Alternatively, a volume average could be obtained by

probing the tank in many locations simultaneously and averaging their signals for each time t. In homogeneous turbulence, which means statistical properties independent on location, ensemble and volume averages are equal. These averaging properties facilitate the calculation of the ensemble average for a turbulent pipe (or channel) flow. Averages can be made in time, and also in space for the homogeneous directions. Thus, reducing the total flow time required to achieve statistical convergence.

2.5.1.1 Reynolds Decomposition

In a statistically steady flow a variable can be split into a time-averaged and a fluctuation parcel. For example, a velocity component can be written as

$$u_\alpha(t) = \overline{u}_\alpha + u'_\alpha(t) \tag{2.41}$$

While $\overline{u}_\alpha$ is time invariant, the fluctuation parcel u'_α is not. It should be noted that $\overline{u'}_\alpha = 0$. Higher-order statistics such as $\overline{u'_\alpha u'_\beta}$ are generally non-zero.

The mass balance equation was shown in Equation 2.29. An incompressible form of it produces a divergence-free velocity field $\partial_\alpha u_\alpha = 0$. It can be easily demonstrated that the velocity field parcels are also divergence-free: $\partial_\alpha \overline{u}_\alpha = \partial_\alpha u'_\alpha = 0$. The momentum balance (Eq. 2.37) in an incompressible form is

$$\rho\partial_t u_\alpha + \rho u_\beta \partial_\beta u_\alpha = -\partial_\alpha p + \partial_\beta \left(\eta\dot{\gamma}_{\alpha\beta}\right) + F_\alpha \tag{2.42}$$

By time-averaging this equation for a statistically steady flow, one gets

$$\rho\overline{u}_\beta\partial_\beta\overline{u}_\alpha = -\partial_\alpha\overline{p} + \partial_\beta\left(\overline{\eta}\overline{\dot{\gamma}}_{\alpha\beta} + \overline{\eta'\dot{\gamma}'_{\alpha\beta}} - \rho\overline{u'_\alpha u'_\beta}\right) + F_\alpha \tag{2.43}$$

where the quantities $-\rho\overline{u'_\alpha u'_\beta}$ and $\overline{\eta'\dot{\gamma}'_{\alpha\beta}}$ are the Reynolds stress and the turbulent viscous stress, respectively. Note in passing that, since F_α is used as a flow drive term (constant), the time-averaged pressure gradient in the streamwise direction $\partial_\alpha\overline{p}$ is zero. However, in a wall-normal direction the time-averaged pressure gradient is generally non-zero.

The significance of the Reynolds stress is well known. It is a consequence of time-averaging the nonlinear inertial term. It is not a true stress, but rather a net effect of momentum fluxes induced by velocity fluctuations. The turbulent viscous stress, on the other hand, is an actual stress. The time-averaged extra stress for a generalized Newtonian fluid is $\overline{\sigma}_{\alpha\beta} = \overline{\eta\dot{\gamma}_{\alpha\beta}} = \overline{\eta}\overline{\dot{\gamma}}_{\alpha\beta} + \overline{\eta'\dot{\gamma}'_{\alpha\beta}}$. So, both terms on the right-hand side are stresses. The reason $\boldsymbol{\sigma}$ was described in terms of viscosity was simply to be consistent with Reynolds-averaged models (RANS). If the fluid were Newtonian, the time-averaged extra stress would be simply $\overline{\eta}\overline{\dot{\gamma}}_{\alpha\beta}$ with $\overline{\eta}$ corresponding to μ. For strain-rate dependent rheology, viscosity fluctuations give rise to an additional viscous stress parcel $\overline{\eta'\dot{\gamma}'_{\alpha\beta}}$. This component do not correspond to any peculiar physical manifestation, it is just a result of the time-average breakdown of a product. The time-averaged Bingham constitutive equation is

$$\begin{cases} \overline{\eta} \to \infty & , |\overline{\boldsymbol{\sigma}}| \leq \sigma_y \\ \overline{\eta} = \eta_p + \sigma_y\overline{\dot{\boldsymbol{\gamma}}^{-1}} & , |\overline{\boldsymbol{\sigma}}| > \sigma_y \end{cases} \tag{2.44}$$

A couple of things must be noticed in Equation 2.44. First, the time-averaged stress magnitude $|\overline{\boldsymbol{\sigma}}|$ is composed of both mean and turbulent parcels. Second, $\overline{\dot{\boldsymbol{\gamma}}^{-1}} \neq \overline{\dot{\boldsymbol{\gamma}}}^{-1}$, so the time-average of the inverse rate-of-strain has to be computed separately.

A RANS-like implementation of a GNF would require some closure model for the turbulent viscous stress. A closure model for the Reynolds stress has been long pursued, and it remains a major challenge in the field of turbulence. Equations 2.42 and 2.43 could be combined to generate an evolution equation for the Reynolds stress. However, this equation would contain triple correlations of the form $\overline{u'_\alpha u'_\beta u'_\gamma}$ that are unknown. When the chaotic, although perfectly deterministic, momentum balance equation is converted to the reproducible time-average form, the equations become under-determined. This is the closure problem of turbulence. The advantage of DNS is the fact that it does not need any closure. The statistical properties presented above are built from DNS data, as if the simulation were a numerical experiment. The overwhelming number of degrees of freedom in a direct numerical simulation normally restricts its use to simple geometries and relatively low Reynolds numbers. Hardware performance and limitations are discussed in Section 3.5.

2.5.2 Existing Schemes

The locality of LBM operations makes them particularly interesting for heavy-work computations, since it can be efficiently parallelized for GPU computation (JANUSZEWSKI and KOSTUR, 2014). Since the requirement for low Mach number prevents the characteristic velocity U to be increased, the artifact for high Reynolds number simulations in LBM is reducing the relaxation time τ (reducing viscosity). This causes problems in the standard LBM, because the LBGK suffers severe instabilities at low τ. There are many workarounds for this problem, the most commonly employed being the Multiple-Relaxation-Time (MRT) collision operator. The MRT has been successfully applied to DNS studies (SUGA et al., 2015; PENG and WANG, 2018; WANG et al., 2019). However, in terms of accuracy, it does not seem superior to LBGK (GEHRKE et al., 2017; NATHEN et al., 2018). An alternative fix for stability problems is the regularization of ghost moments (LATT and CHOPARD, 2006; MATTILA et al., 2017), which is adopted in the present work. This technique has been used by Nathen et al. (2018), who solved three-dimensional turbulent Taylor-Green vortex flow by DNS. Hegele Jr et al. (2018) employed regularization of ghost moments in bulk and boundary nodes in direct numerical simulations of lid-driven cavity flow with Reynolds number up to 5×10^4. In both works, the researchers obtained good stability properties. Nonetheless, further work is necessary to assess the dissipative behavior of the regularized LB.

In investigations on turbulent flow with LBM, there has been some controversy related to rotational invariance. Kang and Hassan (2013) published results of large eddy simulation in circular and square ducts for which the D3Q19 lattice broke the rotational invariance and produced unreasonable data. When the D3Q27 lattice was employed, the rotational invariance in terms of long-time-averaged turbulence statistics was achieved. However, more recently, Peng et al. (2018) published a comprehensive study of lattice effects for DNS in circular duct and accurate turbulence statistics were obtained using both D3Q19 and D3Q27 lattices. The only setback they found with D3Q19 was related to stability, not to rotational invariance. The authors claimed that the spurious transversal currents found in previous works (KANG and HASSAN, 2013; SUGA et al., 2015) are actually a much weaker artifact when a careful

implementation is made.

2.6 Chapter Summary

In this chapter the fundamentals of the lattice Boltzmann method with force term were presented. A Chapman-Enskog expansion analysis was performed in order to demonstrate how the mesoscopic relaxation time τ relates to the viscosity η of the macroscopic momentum balance for generalized Newtonian fluid. The LB scheme presented is valid for low Mach number flows, which means it solves the nearly incompressible mass and momentum balance equations. It was shown that the viscoplastic fluid treatment requires τ to reach very high values. On the other hand, turbulence requires extremely low τ at the walls. This wide range of τ calls for special attention regarding numerical stability. In the next chapter it will be demonstrated how to achieve regularization of ghost moments for LBM with force term, and the complete methodology for DNS of viscoplastic turbulent flow will be presented.

3 NUMERICAL METHODOLOGY

This chapter describes the numerical methodology of the present LB scheme, for which viscoplastic turbulent flow can be calculated through direct numerical simulations. The LBM formulation presented in Chapter 2 is second-order accurate in space and time. The basic collision and streaming processes of LBM, as well as initialization and boundary conditions, will be explained in Section 3.1. Then, in Section 3.2, the viscosity treatment will be disclosed. The main challenge for such method is related to numerical stability. The chosen approach to inhibit instabilities is the regularization of ghost moments, and this will be the topic of Section 3.3. Section 3.4 presents a discussion on how to simulate real flows on LBM based on the Law of Similarity. The performance of a GPU implementation of the present numerical scheme is discussed in Section 3.5. Lastly, a flowchart of the present algorithm will be given in section 3.6.

3.1 Solving the LBGK

The Equation to be solved is 2.16. There is more than one way to solve it. However, the power of LBM is its parallelization capabilities, which are most evident in the traditional collision and streaming algorithm. All numerical operations are done in terms of the inverse relaxation time. The *relaxation frequency* is defined as $\omega = \Delta t/\tau$.

3.1.1 Collision, Streaming and Macroscopics

Equation 2.16 may be decomposed in two steps. The first step is collision:

$$f_i^*(\boldsymbol{x},t) = f_i(\boldsymbol{x},t) - \omega\Big[f_i(\boldsymbol{x},t) - f_i^{\mathrm{eq}}(\boldsymbol{x},t)\Big] + \Big(1-\frac{\omega}{2}\Big)\,F_i(\boldsymbol{x},t)\Delta t \tag{3.1}$$

where f_i^* is the post-collision population. The collision step is a local algebraic operation. Then, the second part reconstitutes Equation 2.16 by streaming all populations along their lattice links:

$$f_i(\boldsymbol{x}+\boldsymbol{c}_i\Delta t, t+\Delta t) = f_i^*(\boldsymbol{x},t) \tag{3.2}$$

One time step is elapsed once these two operations are completed throughout the domain. Unlike the collision step, streaming is not a local operation. However, it also can be run in parallel for all lattice nodes by allocating f_i^* to the computer memory. Resorting to such strategy must be made carefully since memory bandwidth may quickly become the program's bottleneck.

Before moving on to the next iteration, the macroscopic variables must be computed, because they will enter the equilibrium population f_i^{eq}. The macroscopic variables are obtained through velocity moments of f_i, as given by Equations 2.18. The second velocity moment, Equation 2.18c, can be used for obtaining a very fine approximation for the extra stress tensor. According to Equation 2.35, the extra stress $\sigma_{\alpha\beta}$ is equal to $\epsilon\Pi^{(1)}_{\alpha\beta}$. If one assumes that only first order terms in ϵ are responsible for the second velocity moment of non-equilibrium ($\Pi^{\mathrm{neq}}_{\alpha\beta}$), which is consistent with the current Chapman-

Enskog analysis, it turns out that $\epsilon\Pi^{(1)}_{\alpha\beta} = \Pi_{\alpha\beta} - \sum_i f_i^{\mathrm{eq}} c_{i\alpha} c_{i\beta}$. The expression for the extra stress is then

$$\epsilon\Pi^{(1)}_{\alpha\beta} \approx \sigma_{\alpha\beta} = \left(1 - \frac{\omega}{2}\right)\left[\sum_i (f_i - f_i^{\mathrm{eq}}) c_{i\alpha} c_{i\beta} + \frac{\Delta t}{2}(F_\alpha u_\beta + F_\beta u_\alpha)\right] \tag{3.3}$$

The fact that the stress can be obtained without calculating any gradient is a very important characteristic for computational performance.

3.1.2 Initialization

Transient problems require initial conditions. The simplest way to initialize the populations f_i is to equal them to their equilibrium state of a known initial density ρ_0 and velocity $\boldsymbol{u_0}$:

$$f_i(\boldsymbol{x}, t = 0) = f_i^{\mathrm{eq}}(\rho_0, \bar{\boldsymbol{u}}_{\boldsymbol{0}}) \tag{3.4}$$

where $\bar{\boldsymbol{u}}_{\boldsymbol{0}} = \boldsymbol{u_0} - \boldsymbol{F}\Delta t/2\rho_0$ in order to obey the discrete moment in Equation 2.18b (GINZBURG et al., 2008). However, some types of problems are sensitive to initial conditions and require a more accurate initialization. When this is the case, the non-equilibrium part f_i^{neq} must be added to the right-hand side of Equation 3.4. Section 3.3 will demonstrate how to obtain Equation 3.23 as a good approximation for f_i^{neq}, as long as the initial rate-of-strain field is known.

3.1.3 Boundary Conditions

Macroscopic numerical methods use functions of properties such as density, temperature and velocity as boundary conditions. Converting these properties to particle distribution functions is not a trivial task. Although the boundary condition treatment in LBM is not so intuitive, some principles do help simplifying it. The boundary conditions used in the present work are of just two types: periodic and no-slip. For more options and a thorough discussion on boundary conditions in LBM the reader is referred to Latt et al. (2008).

3.1.3.1 Periodic Boundary

Periodic boundary conditions assume that the fluid leaving the domain at one side will re-enter in the opposite side with the same properties. It is commonly used in fully developed flows and turbulence. Though turbulence is never truly periodic, when applied correctly it provides reliable long-time-averages. Care must be taken with the domain size L, because this boundary condition leads to finite size structures with length no greater than L. Thus, it is necessary to validate the domain size to make sure the physically expected structures are in fact smaller than L. The driving force for the fluid flow could be a pressure difference, but this would lead to an artificial mass increase within the domain (KRÜGER et al., 2009). All along, the intention of formulating an LBM with force was to implement a source term to act as a driving force. Consequently, the periodic boundary condition of the present work conserves mass and momentum at all times.

Figure 3.1 – Schematic of the periodic boundary condition on the left/right edges. Grey arrows are post-collision populations and black arrows are streamed populations. Periodic boundaries are separated from adjacent nodes by a distance $\Delta x/2$.

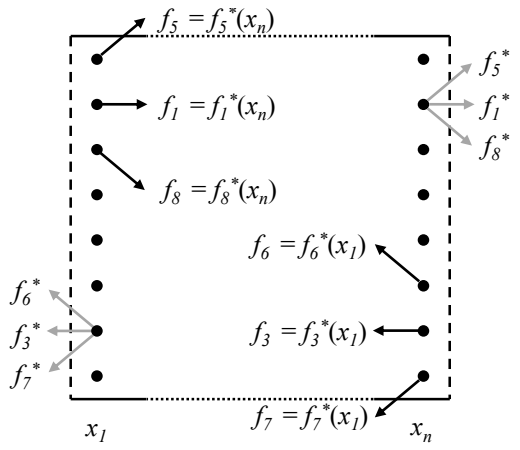

Source: the author.

Figure 3.1 illustrates a domain with periodic boundary condition in x_1 and x_N. The treatment used in the present work is to simply stream the populations between the periodic nodes, as if both boundaries were connected. For a D2Q9 velocity set for instance, one would find for the nodes at x_1

$$\begin{cases} f_1(x_1, y_2, t + \Delta t) = f_1^*(x_N, y_2, t) \\ f_5(x_1, y_2, t + \Delta t) = f_5^*(x_N, y_1, t) \\ f_8(x_1, y_2, t + \Delta t) = f_8^*(x_N, y_3, t) \end{cases} \tag{3.5}$$

and for the nodes at x_N

$$\begin{cases} f_3(x_N, y_2, t + \Delta t) = f_3^*(x_1, y_2, t) \\ f_6(x_N, y_2, t + \Delta t) = f_6^*(x_1, y_1, t) \\ f_7(x_N, y_2, t + \Delta t) = f_7^*(x_1, y_3, t) \end{cases} \tag{3.6}$$

3.1.3.2 Solid Boundary: Halfway Bounce-Back

The principle behind the LBM approach for solid walls is called *bounce-back*. As shown in Figure 3.2 the population f_8 (assuming D2Q9) hitting a wall is reflected back to where it came from. Hence, the streaming step will take it to the opposite position (i =6). Formally, the halfway bounce-back can be expressed as (LADD, 1994)

$$f_{\bar{i}}(\boldsymbol{x_b}, t + \Delta t) = f_i^*(\boldsymbol{x_b}, t) \tag{3.7}$$

where the bar over i represents its opposite direction and the subscript b means boundary. The bounce-back of a population hitting a wall implies no mass flux across the boundary (impermeable wall). Also, the particle's return to its original node, as opposed to being bounced forward, implies no-slip. This

boundary condition is prevalent in LBM due to its simplicity, which makes it particularly preferred for 3D domains. In the case of a moving wall, a correction term must be added:

$$f_{\bar{i}}(\boldsymbol{x_b}, t + \Delta t) = f_i^*(\boldsymbol{x_b}, t) - 2w_i\rho_{\mathrm{w}}\frac{\boldsymbol{c_i}\cdot\boldsymbol{u_w}}{c_s^2} \tag{3.8}$$

Figure 3.2 – Schematic of the halfway bounce-back boundary condition for a D2Q9 lattice. The incoming population f_8^* arrives at the wall and bounces back to the node where it came from, assuming the position f_6 after a single time step Δt has elapsed.

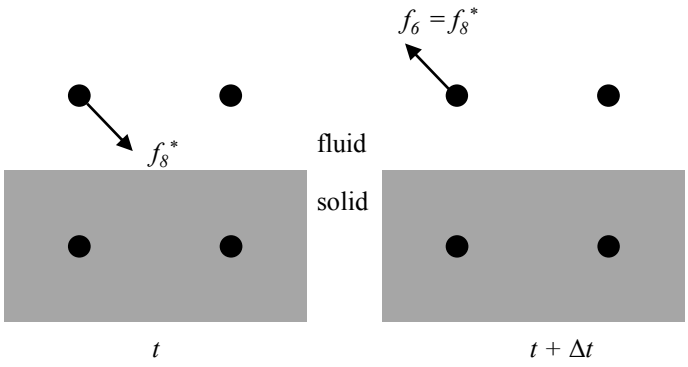

Source: the author.

It is important to note that the halfway bounce-back is a link-wise method, i.e., the solid wall is expected to be distant $\Delta x/2$ from the boundary node. The accuracy of the link-wise bounce-back is τ-dependent, with an optimum at $1/2 + \sqrt{3/16}$ (GINZBURG and D'HUMIÈRES, 2003). As a consequence of using other τ values, the solid boundary will no longer be located at $\Delta x/2$, which requires the solution to be corrected in post-processing. Although it is second-order accurate in space, if a close-to-optimal τ cannot be set at the wall, a more accurate boundary condition is recommended.

3.1.3.3 Solid Boundary: Non-Equilibrium Bounce-Back

Zou and He (1997) developed a third-order accurate bounce-back scheme by reflecting only the non-equilibrium part. It is a wet-node method, meaning that the boundary node is placed exactly on the wall interface. Remarkably, its accuracy is independent of τ. The underlying principle is

$$f_{\bar{i}}^{\mathrm{neq}}(\boldsymbol{x_b}, t) = f_i^{\mathrm{neq}}(\boldsymbol{x_b}, t) - \frac{\boldsymbol{t}\cdot\boldsymbol{c_i}}{|\boldsymbol{c_i}|}C_t \tag{3.9}$$

where $\boldsymbol{t}$ is a tangent unit vector on $\boldsymbol{x_b}$ and C_t is a correction term necessary to ensure the desired tangential velocity. The procedure requires that the density on $\boldsymbol{x_b}$ is known a priori. In some cases, extrapolation is necessary. For a D2Q9 velocity set ρ_{w} can be determined by the known populations. Figure 3.3 illustrates the application of the non-equilibrium bounce-back on a top surface. After streaming, the populations f_4, f_7 and f_8 are unknown. The term $f_4 + f_7 + f_8$ can be eliminated from the ρ_{w} calculation (Equation 2.18a) by combining it with the second moment (Equation 2.18b). For an impermeable wall, the resulting expression is

$$\rho_{\mathrm{w}} = f_0 + f_1 + f_3 + (f_2 + f_5 + f_6) + \frac{F_{y,\mathrm{w}}\Delta t}{2} \tag{3.10}$$

The application of Equation 3.9 leads to the following system

$$\begin{cases} f_4 = f_2 + (f_4^{\mathrm{eq}} - f_2^{\mathrm{eq}}) - C_y \\ f_7 = f_5 + (f_7^{\mathrm{eq}} - f_5^{\mathrm{eq}}) - C_x - C_y \\ f_8 = f_6 + (f_8^{\mathrm{eq}} - f_6^{\mathrm{eq}}) + C_x - C_y \end{cases} \tag{3.11}$$

C_x and C_y can be solved by inputting the above equations into the x- and y-moments of Equation 2.18b, respectively. Their solution is

$$C_x = -\frac{1}{2}(f_1 - f_3) + \frac{\rho_{\mathrm{w}} u_{x,\mathrm{w}}}{3} - \frac{F_{x,\mathrm{w}}\Delta t}{2} \tag{3.12a}$$

$$C_y = -\frac{F_{y,\mathrm{w}}\Delta t}{6} \tag{3.12b}$$

Then, the final solution for the unknown populations is obtained by replacing Equation 3.12 into 3.9:

$$\begin{cases} f_4 = f_2 - \dfrac{2\rho_{\mathrm{w}} u_{y,\mathrm{w}}}{3} + \dfrac{F_{y,\mathrm{w}}\Delta t}{6} \\ f_7 = f_5 + \dfrac{1}{2}(f_1 - f_3) - \dfrac{\rho_{\mathrm{w}} u_{x,\mathrm{w}}}{2} - \dfrac{\rho_{\mathrm{w}} u_{y,\mathrm{w}}}{6} + \dfrac{F_{x,\mathrm{w}}\Delta t}{4} + \dfrac{F_{y,\mathrm{w}}\Delta t}{6} \\ f_8 = f_6 - \dfrac{1}{2}(f_1 - f_3) + \dfrac{\rho_{\mathrm{w}} u_{x,\mathrm{w}}}{2} - \dfrac{\rho_{\mathrm{w}} u_{y,\mathrm{w}}}{6} - \dfrac{F_{x,\mathrm{w}}\Delta t}{4} + \dfrac{F_{y,\mathrm{w}}\Delta t}{6} \end{cases} \tag{3.13}$$

Implementing the above procedure for 3D geometries is a cumbersome task. Also, a generic algorithm of this method would be very inefficient. The trade-off for the excellent accuracy is its implementation difficulties. For instance, if the domain is a rectangular cuboid, it will require an individual treatment for all unknown populations in 6 faces, 12 edges and 8 vertices. In this case, a D3Q27 lattice would require 234 expressions to be determined!

Figure 3.3 – Schematic of the non-equilibrium bounce-back boundary condition. After streaming, the populations represented by the solid arrows are known. The populations represented by the dashed arrows are unknown and have to be determined.

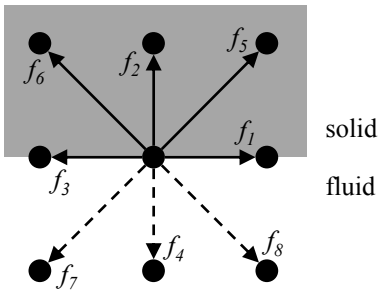

Source: the author.

3.2 Viscosity Treatment

The relaxation frequency ω is intrinsically tied to the fluid's viscosity η, as demonstrated through the Chapman-Enskog expansion in Chapter 2. A potential advantage for simulation of yield stress materials

with LBM comes from noting that ω could be set to zero to represent the singularity in the viscoplastic constitutive equation. Equation 2.36 can be expressed in terms of relaxation frequency as

$$\omega = \frac{2\eta^-}{\frac{2}{\Delta t \rho c_s^2} + \eta^-} \tag{3.14}$$

where η^- is the inverse of viscosity, which in the case of Bingham fluid ranges from 0 (infinite viscosity) to $1/\eta_p$. In Equation 3.14 ω is bounded by 0, when $\eta^- = 0$, and 2, when $\eta^- \to \infty$ (inviscid). The Bingham constitutive equation in terms of η^- is

$$\eta^- = \begin{cases} 0 & , |\boldsymbol{\sigma}| \leq \sigma_y \\ \left(\eta_p + \frac{\sigma_y}{|\dot{\boldsymbol{\gamma}}|}\right)^{-1} & , |\boldsymbol{\sigma}| > \sigma_y \end{cases} \tag{3.15}$$

The relaxation frequency has to be computed in the macroscopics evaluation step, since it will be required in the collision process of the next iteration. It is obtained by Equation 3.14 with η^- from Equation 3.15. The extra stress $\boldsymbol{\sigma}$ components are obtained by Equation 3.3. However, ω and $\boldsymbol{\sigma}$ are implicitly related, because Equation 3.3 needs ω in the first place.

One way to solve this implicit relationship is through an iterative scheme (inner-iterations), but it would compromise numerical efficiency. Another option is to take ω from the previous time-step to insert in Equation 3.3. The temporal error introduced by this procedure can be diminished by decreasing Δt, which in LBM occurs simultaneously along with spatial refinement. Indeed, this option was chosen for the steady-state cases presented in Section 4.1, and it produced satisfactory results.

Fortunately, an exact solution for ω can be found. Considering the generalized Newtonian fluid, it is noted that the magnitudes of stress and rate-of-strain are related by $|\boldsymbol{\sigma}| = \eta(|\dot{\boldsymbol{\gamma}}|)|\dot{\boldsymbol{\gamma}}|$. The Bingham viscosity η is an invertible function of $|\dot{\boldsymbol{\gamma}}|$. This means the stress magnitude is sufficiently defined by the viscosity: $|\boldsymbol{\sigma}| = |\boldsymbol{\sigma}|(\eta)$. The rate-of-strain function is

$$|\dot{\boldsymbol{\gamma}}|(\eta) = \begin{cases} 0 & , |\boldsymbol{\sigma}| \leq \sigma_y \\ \frac{\sigma_y}{\eta - \eta_p} & , |\boldsymbol{\sigma}| > \sigma_y \end{cases} \tag{3.16}$$

Consider for a moment a blob of yielded material. In this case the GNF relation predicts the stress magnitude to be

$$|\boldsymbol{\sigma}| = \frac{\sigma_y}{1 - \eta_p \eta^-} = \frac{\sigma_y}{1 - \left(\frac{1-\omega_p}{\omega_p}\right)\left(\frac{\omega}{2-\omega}\right)} \tag{3.17}$$

where ω_p is the relaxation frequency associated with the plastic viscosity η_p. The above equation will be left aside for a while. Equation 3.3 gives another expression for the stress magnitude:

$$|\boldsymbol{\sigma}| = \left(1 - \frac{\omega}{2}\right)|\boldsymbol{T}| \tag{3.18}$$

where the tensor $\boldsymbol{T}$ is simply the ω-independent part of $\boldsymbol{\sigma}$

$$T_{\alpha\beta} = \left[\sum_i \left(f_i - f_i^{\mathrm{eq}}\right) c_{i\alpha} c_{i\beta} + \frac{\Delta t}{2}\left(F_\alpha u_\beta + F_\beta u_\alpha\right)\right] \tag{3.19}$$

Eliminating $|\boldsymbol{\sigma}|$ between Equations 3.17 and 3.18 results in

$$\omega = \omega_p \left(1 - \frac{\sigma_y}{|\boldsymbol{T}|}\right) \tag{3.20}$$

Equation 3.20 gives an exact solution for ω in a yielded material. The question remaining is how to obtain an answer for a unyielded portion of material. There is only one possible solution, which is $\omega = 0$. In that case, the consideration that the stress magnitude be lower, or equal than, the yield stress requires $|\boldsymbol{T}| \leq \sigma_y$, or $\sigma_y/|\boldsymbol{T}| \geq 1$. Thus, the conditional solution for the relaxation frequency is

$$\omega = \omega_p \max\left(0, 1 - \frac{\sigma_y}{|\boldsymbol{T}|}\right) \tag{3.21}$$

Whenever Equation 3.21 is checked in a unyielded point, the expression $1 - \sigma_y/|\boldsymbol{T}|$ will be negative, which gives $\omega = 0$ as answer. In Section 4.2, this viscosity treatment is validated against theoretical solutions of transient viscoplastic laminar flows. Besides an improved transient accuracy, this implementation also contributed for a better numerical stability. The viscoplastic turbulent channel flow of Chapter 5 was solved with Equation 3.21. The above calculations retain the locality of the standard LBM, and are therefore perfectly suitable for large scale computations. The same procedure could be used to obtain an exact solution for the Power-Law constitutive equation. However, it would not be possible for the Herschel–Bulkley model, because its viscosity is not an invertible function of the rate-of-strain magnitude.

Viscoplastic flows are characterized by a wide range of viscosity levels throughout the domain. As a consequence, the relaxation frequency is also going to have a spectrum. With respect to accuracy, an error proportional to $(\tau - 1/2)^2$ is known to inflict on the LBGK (D'HUMIÈRES and GINZBURG, 2009). The nature of this error comes from neglecting higher-order terms in the Chapman-Enskog expansion. In Section 4.1 it is demonstrated that the overall error can be significantly brought down by resolution refinement, implying that the relaxation frequency spectrum did not harm the solution. In the limit of $\omega \to 0$, stability becomes troubling (GRASINGER et al., 2018). In the present work this problem is worked out by regularization of ghost moments.

3.3 Regularization of Ghost Moments

In Equation 3.1 the orders $f_i^{(k)}$ entering the population f_i are unbounded. Nonetheless, the Chapman-Enskog analysis of Section 2.3 considered terms up to order $\mathcal{O}(\epsilon)$ as relevant to the LBGK formulation. All of those $f_i^{(k)}$ terms with $k \geq 2$ are generative of ghost moments[1], which recover higher-order dynamics such as the Burnett equations (CHAPMAN and COWLING, 1970). Although these higher-order terms have small magnitude, they do spoil the solution stability.

Confronted with this problem, Latt and Chopard (2006) proposed a regularization of the ghost moments for low order LBM. Mattila et al. (2017) expanded the method, demonstrating how to apply it for higher order of truncation and more elaborated lattices. Also, this approach is attractive because it can be used with the simple BGK collision operator, dismissing the need for the time-consuming MRT.

[1] Rigorously speaking, some high-order moments of $f_i^{(1)}$ are also ghosts, for they do not fit into the Hermitian representation of the D2Q9 and D3Q19 lattices (MATTILA et al., 2017). As a consequence, $\mathcal{O}(u^3)$ errors are manifested in the macroscopic momentum equations and the method is bound to low U, as was stated in the Chapman-Enskog expansion.

The following procedure is inspired in the work of Latt and Chopard and validated by Silva and Semiao (2012). It starts with Equation 2.25a, repeated here for convenience:

$$\left(\partial_t^{(1)} + c_{i\alpha}\partial_\alpha^{(1)}\right) f_i^{\mathrm{eq}} - \left(1 - \frac{\Delta t}{2\tau}\right) F_i^{(1)} = -\frac{1}{\tau} f_i^{(1)} \tag{3.22}$$

The solution for the temporal and spatial derivatives of f_i^{eq} may be obtained by the exact same procedures used in Section 2.3 to determine $\Pi_{\alpha\beta}^{(1)}$. After a great deal of algebra, the expression for $f_i^{(1)}$ is

$$\begin{aligned} \epsilon f_i^{(1)} = -\frac{w_i \tau}{c_s^2}\Bigg[& \frac{Q_{i\alpha\beta}}{2}\rho\left(\partial_\alpha u_\beta + \partial_\beta u_\alpha\right) + \frac{\Delta t}{4\tau}\frac{Q_{i\alpha\beta}}{c_s^2}\left(u_\alpha F_\beta + u_\beta F_\alpha\right) + \frac{\Delta t}{2\tau} c_{i\alpha} F_\alpha \\ & - c_{i\alpha}\partial_\beta\left(\rho u_\alpha u_\beta\right) + \frac{Q_{i\alpha\beta}}{2c_s^2} c_{i\gamma}\partial_\gamma\left(\rho u_\alpha u_\beta\right)\Bigg] \end{aligned} \tag{3.23}$$

where $Q_{i\alpha\beta} = c_{i\alpha}c_{i\beta} - c_s^2\delta_{\alpha\beta}$ is a symmetric tensor and it has the property $Q_{i\alpha\beta}A_{\alpha\beta} = Q_{i\alpha\beta}A_{\beta\alpha}$. It must be noticed that non-linear terms do not contribute to $\mathbf{\Pi}^{(1)}$ and, therefore, are too small within the above equation. Invoking Equation 2.35, $\epsilon\Pi_{\alpha\beta}^{(1)}$ can replace the first term in the right-hand side of Equation 3.23, and it becomes

$$\epsilon f_i^{(1)} = \frac{w_i}{c_s^4}\left[\left(\frac{\tau}{2\tau - \Delta t}\right) Q_{i\alpha\beta}\left(\epsilon\Pi_{\alpha\beta}^{(1)}\right) - \frac{\Delta t}{4} Q_{i\alpha\beta}\left(u_\alpha F_\beta + u_\beta F_\alpha\right) - \frac{\Delta t}{2} c_s^2 c_{i\alpha} F_\alpha\right] \tag{3.24}$$

Considering $\epsilon\Pi_{\alpha\beta}^{(1)} \approx \sigma_{\alpha\beta}$ according to Equation 3.3:

$$\epsilon f_i^{(1)} \approx \frac{w_i}{2c_s^4}\left(Q_{i\alpha\beta}\sum_i f_i^{\mathrm{neq}} c_{i\alpha}c_{i\beta} - \Delta t c_s^2 c_{i\alpha} F_\alpha\right) \tag{3.25}$$

Equation 3.25 shows that the $\mathcal{O}(\epsilon)$ populations can be approximated by the known populations and a force term correction. The insight of regularization is to replace the non-equilibrium distribution f_i^{neq} by $\epsilon f_i^{(1)}$ during the collision operation, defining a new population $f_i^{\mathrm{reg}} = f_i^{\mathrm{eq}} + \epsilon f_i^{(1)}$. The collision step thus becomes

$$f_i^* = (1-\omega) f_i^{\mathrm{reg}} + \omega f_i^{\mathrm{eq}} + (1 - \omega/2)\Delta t F_i \tag{3.26}$$

Excellent stability properties are achieved with regularization. Latt and Chopard (2006) reported that the maximum Reynolds number possible to be simulated in a lid-driven cavity flow increased by a factor of 7.7 for the force-free LBGK. Also, regularization has been successfully implemented for turbulence simulations (NATHEN et al., 2018; Hegele Jr et al., 2018). Stability tests' results for viscoplastic flow are presented in Chapter 4.

3.4 Lattice Units and Similarity

All variables entering the LBM equations are in lattice units, which are non-dimensional quantities emanated from the velocity space discretization. The variables Δt, Δx and ρ (reference density) are commonly set to unity. There is no good reason to depart from this habit. In LBM simulations, one has to resort to the *law of similarity* to reproduce the desired physics. Apart from the geometric similarity,

the dynamic similarity requires that the pertinent non-dimensional groups are the same in lattice (l) and physical (p) units. For instance, the Reynolds number matching would require

$$\frac{U_l L_l}{\nu_l} = \frac{U_p L_p}{\nu_p} \tag{3.27}$$

The Mach number $Ma = U/c_s$ is kept small by making sure the maximum local velocity is an order of magnitude lower than the speed of sound ($c_s = 1/\sqrt{3}$ in lattice units). It must be noticed that the similarity in Ma does not necessarily need to be obeyed for nearly incompressible flows. If Ma is small enough, its absolute value does not make any detectable difference in the flow field (KRÜGER et al., 2017).

The length scale in lattice units is $L_l = N_x(\Delta x)_l$, where N_x is the number of lattices equally spaced by $(\Delta x)_l$. In mesh resolution tests, it is often necessary to increase the spatial resolution while keeping Re constant. Therefore, the only two possibilities for it are decreasing U_l or increasing ν_l, while N_x is increased proportionally. This sometimes causes confusion about the time scale of successive simulations with resolution refinement. The rule of thumb is to remember the total time $T_l = N_t(\Delta t)_l$ is proportional to the phenomenon time scale L_l/U_l (or L_l^2/ν_l for highly viscous flow). Hence, the number of time steps follows the proportion

$$N_t \sim \frac{N_x[(\Delta x)_l/(\Delta t)_l]}{U_l} \tag{3.28}$$

3.5 Computational Performance

The numerical scheme developed in this work was implemented for computation in graphics processing units (GPU). Implementation details can be found in Oliveira Jr et al. (2019). The distinguishing characteristic of GPUs is the elevated number of processing cores. Due to the inherent locality of most LBM operations, the parallel efficiency is remarkable. On the other hand, LBM is too demanding on memory. So, the most accessible GPU models may not have enough memory for some direct numerical applications. In the text that follows, the performance of the current GPU implementation for LBM is discussed in detail.

3.5.1 Processing Speed

In the standard LBM, the collision and macroscopic evaluation operations are completely local. The bounce-back operations in the present work are also local, because two sets of populations are stored, one for post-collision and one for post-streaming. The aspect of locality can be very well explored in GPU. In a relatively low-cost piece of hardware (US$1000), the NVIDIA Tesla K20x, the number of million lattices/nodes updates per second (MLUPs) was 400. Taking a 3D case with 128^3 nodes as example, one million time-steps are solved in approximately 90 minutes. The NVIDIA Tesla K20x was used in the laminar cases of Chapter 4. For the turbulent cases of Chapter 5, the NVIDIA Tesla V100 32Gb was used. It is nearly ten times more expensive than the K20x. The number of MLUPs with this machine was around 1500.

For reference, Zheng et al. (2019) investigated the computational performance of a finite volume code (OpenFOAM) and a spectral element-Fourier code (Semtex) for DNS in a massively parallel system. The

computational infrastructure consisted of hundreds of CPUs, installed in multiple compute nodes. The authors reported 6 MLUPs for OpenFOAM with 512 CPUs, and 21 MLUPs for Semtex with 192 CPUs.

3.5.2 Memory Limitations

With the D3Q19 lattice, memory allocation of 19 populations is required. In practice, in order to be able to perform the streaming process in parallel, two sets of populations are stored, post-collision and post-streaming. This leads to a total of 38 double-precision floating point variables for each grid node, without counting the macroscopic quantities (velocity components, density, relaxation frequency and stress components). As if that was not enough, in the present LBM the grid is uniform, i.e., $\Delta x = \Delta y = \Delta z$. This means that the grid is always overdimensioned, because the entire domain follows the resolution of the most critical region. For example, in the turbulent channel flow of Chapter 5, Δy is defined according to the resolution necessary at the walls. However, the grid spacing in the x and z directions could be much larger, without compromising the statistical outcome. To be precise, if a non-uniform LBM grid was viable, the total number of grid nodes in this case would be ten times less.

Clearly, the memory demand of the LBM, compared with other methods, is overwhelming. The NVIDIA Tesla K20x has 6Gb of internal memory, which was capable of allocating about 15 million nodes. Because of the uniform grid, this amount was not enough for the channel length necessary for DNS. Hence, the NVIDIA Tesla V100 32Gb had to be used in the case study of Chapter 5.

In the specialized literature, attention has been given to the formulation of non-uniform LBM grids. This is commonly referred to as rectangular LBM. The most important works are the ones from He et al. (1996), Hegele Jr et al. (2013), Peng et al. (2019). However, for one reason or another, the maximum aspect ratio in these works is not large enough to justify its implementation in the present thesis. An aspect ratio ($\Delta x/\Delta y$) around 5 would certainly be a phenomenal feature for direct numerical simulations with LBM.

3.6 Algorithm

The numerical methodology described above is presented in this section in algorithmic form. All steps from 3 to 7 are repeated for every point in space ($\boldsymbol{x}$). Figure 3.4 illustrates the workflow of the present LB scheme.

1. **Definitions.** The relevant non-dimensional groups such as Reynolds and Bingham numbers are set, as well as the lattice resolution (N_x, N_y, N_z) and reference velocity (U). The combination of these parameters results in the LBGK inputs, which are the relaxation frequency (ω) and the source term (F_x, F_y, F_z). The mesoscopic yield stress is also defined in this step.

2. **Initialization.** The initial macroscopic fields ($\boldsymbol{u_0}$ and ρ_0) are converted into the initial populations through Equation 3.4. In the case of sensitive initial conditions, the regularized non-equilibrium term (Equation 3.23) is added to f_i^{eq}.

3. **Update ω.** First, the components of the auxiliary tensor $\boldsymbol{T}$ are computed by Equation 3.19. Then, the local relaxation frequency is updated via Equation 3.21.

4. **Regularized Collision.** The regularized collision step takes place with Equation 3.26.

5. **Streaming.** The post-collision populations are advanced in time and space according to Equation 3.2. Care must be taken to avoid streaming to or from a null location. Moreover, a streamed population cannot overwrite a post-collision population that has not yet been propagated.

6. **Boundary Conditions.** The boundary conditions described in section 3.1.3 are applied in this step. Post-streaming populations at the boundaries are updated with the post-collision populations of the current iteration.

7. **Macroscopics.** The macroscopic properties ρ and $\boldsymbol{u}$ are computed by Equations 2.18a and 2.18b, respectively. Also, the stress tensor $\boldsymbol{\sigma}$ comes from Equation 3.3. If necessary, the macroscopic quantities are stored for statistical processing.

8. **Statistical Gathering.** In the direct numerical simulations, volume averages are calculated in this step. This is a very slow process because all macroscopic data have to be transferred from the GPU to the CPU. So, this is only done once every 1000 time-steps.

9. **Stop Criterion Reached?** In this checkpoint the program must decide whether to continue or stop the simulation. Two types of stop criteria may be used. It may either be the maximum number of time steps (N_t) or the steady-state residual, defined by

$$L_{ST} = \sqrt{\frac{\sum_{\boldsymbol{x}} \left(u_{x,t} - u_{x,t-1000\Delta t}\right)^2 + \left(u_{y,t} - u_{y,t-1000\Delta t}\right)^2 + \left(u_{z,t} - u_{z,t-1000\Delta t}\right)^2}{\sum_{\boldsymbol{x}} \left(u_{x,t}\right)^2 + \left(u_{y,t}\right)^2 + \left(u_{z,t}\right)^2}} \tag{3.29}$$

where the summation takes place over all fluid nodes. An L_{ST} residual of 10^{-12} is an adequate stop criterion for many applications (LUO et al., 2011). In case the stop criterion has not been reached, the program continues from step 3.

3.7 Chapter Summary

Intrinsic numerical aspects of the proposed viscoplastic LB scheme were discussed in this chapter. The turbulence representation is intended to be obtained through direct numerical simulations, thereby not needing any modeling. Proper initialization and boundary conditions for accurate simulations were presented. The differential of the present scheme is the actual representation of infinite viscosity from the Bingham constitutive equation. This is possible by implementing a regularization of ghost moments for the LBM with force. In the next chapter, the proposed scheme will be tested for stability and accuracy in classical viscoplastic laminar flows.

Figure 3.4 – Flowchart of the computational routine for viscoplastic LB scheme.

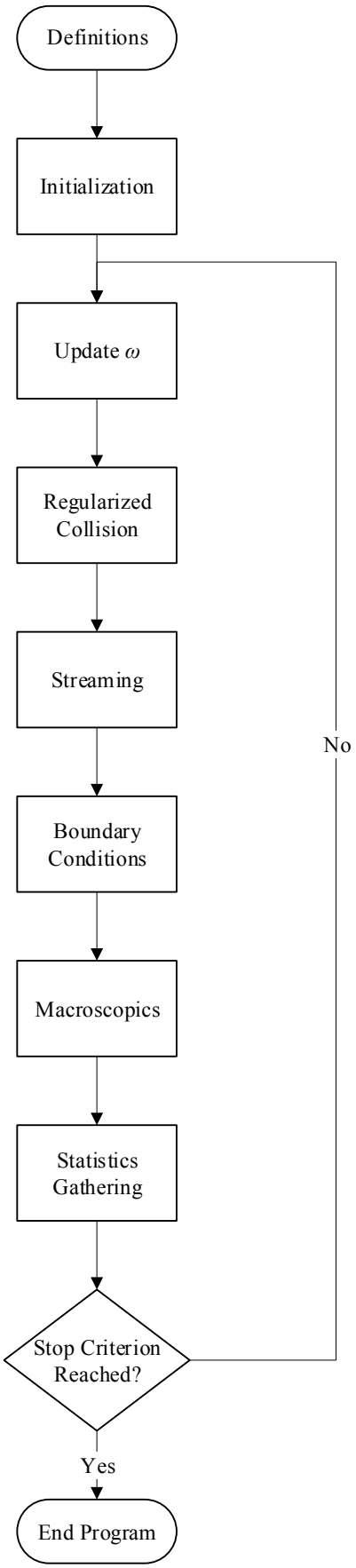

Source: the author.

4 LAMINAR FLOWS

In this chapter, the numerical methodology presented in the preceding pages is put to the test in viscoplastic laminar flows. By solving these cases, the objective is to evaluate the proposed viscosity treatment, namely, setting the relaxation frequency to zero in the unyielded locations. Unless said otherwise, regularization of ghost moments is employed in all test cases. First, steady-state flows are analyzed in Section 4.1. Then, transient flows are presented in Section 4.2. Although the proposed LB scheme extends seamlessly for any generalized Newtonian fluid, only the Bingham constitutive equation is solved for, because it is the simplest viscoplastic model that has a singularity.

4.1 Steady-State Problems

Numerical solutions of steady-state viscoplastic fluid flows are commonly found in the literature. Hence, there is a plentiful database of benchmark cases. The cases investigated in this section are: parallel plates Pouiseuille flow (Section 4.1.1), square duct Pouiseuille flow (Section 4.1.2), and lid-driven cavity flow (Section 4.1.3). These simulations were done in an early stage of the project, when the exact temporal solution for the relaxation frequency ω (Eq. 3.21) had not been developed. So, for all cases presented in this section, ω used in the calculation of the stress components is taken from the previous time-step.

4.1.1 Parallel Plates Poiseuille Flow

One of the simplest Bingham fluid flows that have an exact solution is the Poiseuille flow between parallel plates. The problem is depicted in Figure 4.1. The fluid between the parallel plates is kept at a constant average velocity of U. Both plates are no-slip boundaries and are separated from a distance H. At a region far enough from the inlet, a fully developed region will take place. In this region, the velocity profile will not change and the pressure drop will be constant.

Figure 4.1 – Physical representation of the parallel plates Poiseuille flow. The flow's average velocity is U and both walls are stationary.

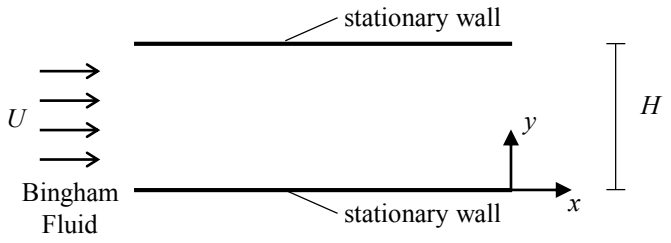

Source: the author.

The currently presented analytical solution is found in (BIRD et al., 2002). The only non-dimensional group governing the solution is the Bingham number, defined as

$$Bn = \frac{\sigma_y}{HF_x} \tag{4.1}$$

where F_x is the momentum source, equivalent to the pressure gradient, necessary to maintain a constant average velocity U:

$$F_x = -\frac{\partial p}{\partial x} = \frac{12\eta_p U}{H^2\left(1 - 3Bn + 4Bn^3\right)} \tag{4.2}$$

The cross section profile of such flow consists in a yielded ($|\boldsymbol{\sigma}| > \sigma_y$) region close to the walls, and a plug region ($|\boldsymbol{\sigma}| \leq \sigma_y$) delimited by

$$\frac{1}{2} - Bn \leq \frac{y}{H} \leq \frac{1}{2} + Bn \tag{4.3}$$

Thus, the limiting cases are $Bn = 0$, corresponding to the absence of a plug (for it would have no volume), and $Bn = 0.5$, corresponding to the whole cross section being plugged (which means no flow at all). The normalized plug velocity is

$$\frac{u}{U} = \frac{3}{2}\frac{(2Bn - 1)^2}{(1 - 3Bn + 4Bn^3)} \tag{4.4}$$

and the normalized yielded fluid velocity is

$$\frac{u}{U} = \frac{1}{(1 - 3Bn + 4Bn^3)}\left\{\frac{3}{2}\left[1 - \left(2\left|\frac{1}{2} - \frac{y}{H}\right|\right)^2\right] - 6Bn\left[1 - 2\left|\frac{1}{2} - \frac{y}{H}\right|\right]\right\} \tag{4.5}$$

This problem was solved with the proposed LB scheme for a 2D domain employing the D2Q9 lattice. Periodic condition was imposed in the left-right boundaries, while the stationary walls were represented by either halfway bounce-back (HWBB) or non-equilibrium bounce-back (NEBB) schemes. The flow was enforced through a constant force term given by Equation 4.2, such that the average velocity U was targeted at 0.1. The plastic Reynolds number $Re_p = \rho U H/\eta_p$ does not influence this fully developed flow, as long as it is laminar. At the walls, a nominal viscosity is defined by $\eta_{\mathrm{w}} = Bn/(1 - 2\eta_p)$. In each simulation, the value for Re_p was determined such that the relaxation time at the nominal wall viscosity was approximately 0.98. The symbol N_x is used to denote the spatial resolution (for example, a grid 128×128 has $N_x = 128$).

Figure 4.2 – Velocity profiles without regularization of ghost moments. Solid lines are exact solutions. (a) NEBB and $Bn = 0.25$ and (b) HWBB and $Bn = 0.40$.

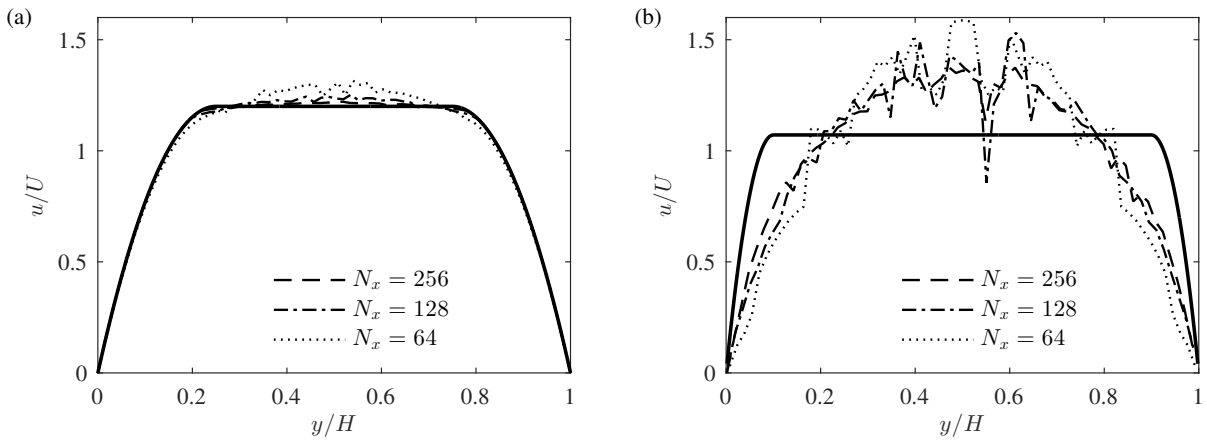

Source: the author.

The consequence of setting a null relaxation frequency ω is that the under-relaxation is so severe that the populations never relax to their local equilibrium. Without regularization of ghost moments, the post collision population f_i^* assume meaningless values caused by higher-order terms. As seen in Figure 4.2, the velocity profiles will never be correctly predicted in this situation. Both HWBB and NEBB were tested in Figure 4.2, as a means to show that the scheme without regularization failed in every attempt. It must be emphasized that spatial refinement did not produce improvements for HWBB. Perhaps a little improvement may be observable for NEBB, but it was not good enough to promote the desired "plug" shape. Although the boundary condition has some effect in weakening the spurious currents, it is not capable of damping them down to an acceptable level. The Burnett stresses are bulk quantities and do not originate at the walls. The problem is more critical as Bn is increased, probably because the under-relaxed region is larger.

The regularization of ghost moments makes feasible the simulation with such low ω. Figure 4.3a shows the time evolution of the steady-state error L_{ST} (Eq. 3.29). It can be seen that the regularized LBE succeeds in bringing the solution to a steady-state, while in the conventional scheme the residual never decreases up to a reasonable solution. As a side note, it is interesting to realize that the regularization of ghost moments stabilizes the solution not only for low τ, for which the method was originally conceived, but also for extremely high τ (low ω). Figure 4.3b shows the velocity profile after the inclusion of regularization. The stability issue is fixed. Even for $Bn = 0.40$, which is quite a difficult case for convergence, the solution is accurate and the plug region is flat. The results of Figure 4.3b were obtained with 128 grid nodes in each direction, which is not the highest resolution employed in the present study.

Figure 4.3 – Results obtained with regularization of ghost moments. (a) Steady state residual L_{ST} with NEBB and $Bn = 0.25$. (b) Velocity profiles with NEBB and several Bn. Solid lines are exact solutions.

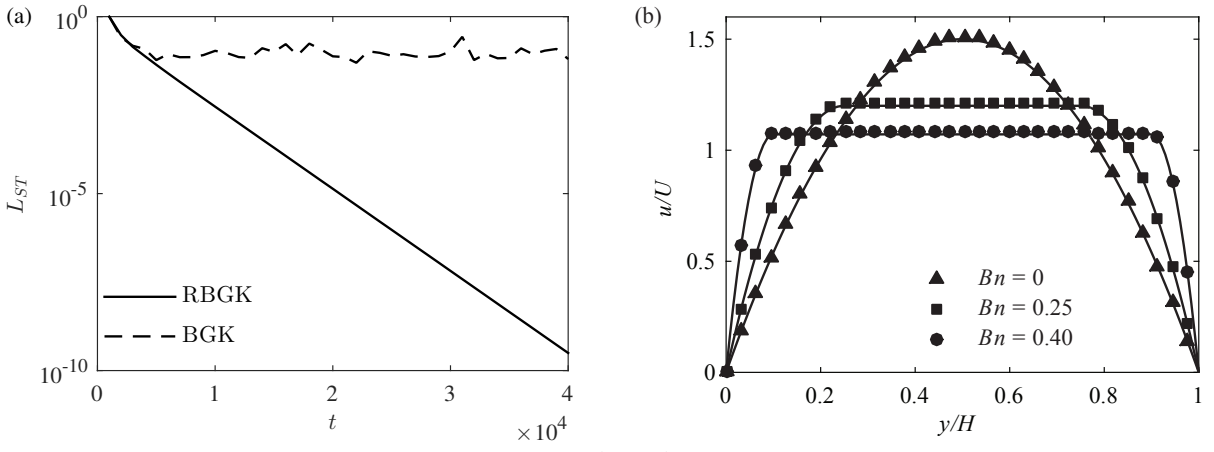

Source: the author.

In order to evaluate the accuracy of the present solution, the quadratic error norm will be used. It is defined as

$$L_2 = \sqrt{\frac{\sum \left(q_{\text{num}} - q_{\text{ref}}\right)^2}{\sum \left(q_{\text{ref}}\right)^2}} \tag{4.6}$$

where q_{num} is the numerical value, q_{ref} is the reference value (preferably analytical) and the summation takes place over a determined set of points of the domain. Figure 4.4 shows how the quadratic error norm L_2 evolved for viscoplastic simulations with HWBB and NEBB. Overall, the expected truncation

order $\mathcal{O}(\Delta x^2)$ did not suffer degradation from the implemented Bingham viscosity. For small Bn, the NEBB boundary condition is only slightly better than HWBB. However, for $Bn = 0.40$, L_2 of HWBB was almost 3 times higher than of NEBB. It has been reported in the literature that when regularization is applied, the use of very small mesoscopic velocities (small Mach number $Ma = U/c_s$) may lead to divergence (MATTILA et al., 2017). However, in all LBM simulations performed in the present work, small Ma divergence was not found.

Single precision results were also obtained for this case. They are shown as empty markers in Figure 4.4. Although it appears that high N_x leads to single precision divergence, the feature that actually causes it is the low mesoscopic velocity U. The data points of Figure 4.4 were obtained with fixed Re and τ. Whenever N_x was doubled, U was decreased in half. U started at 0.1 for N_x = 32. Therefore, for $N_x = 256$, U was 0.0125. The increasing single precision error for small mesoscopic velocity was also reported by Januszewski and Kostur (2014). There is a safe range for single precision computation with the Bingham model, though. In this particular test case, for U up to 0.025 the accuracy of single precision calculations was almost identical to double (notice that the empty markers are behind the filled ones). This is a very important outcome, especially for high-resolution simulations. With respect to double precision on the NVIDIA Tesla K20x, using single precision decreases the memory demand by 50% and increases the processing speed (MLUPs) by a factor of 3.

Figure 4.4 – Quadratic error norm L_2 for different boundary conditions and several Bn. Dashed lines represent the second-order truncation error and empty markers represent single precision mode. (a) $Bn = 0$, (b) $Bn = 0.25$ and (c) $Bn = 0.40$.

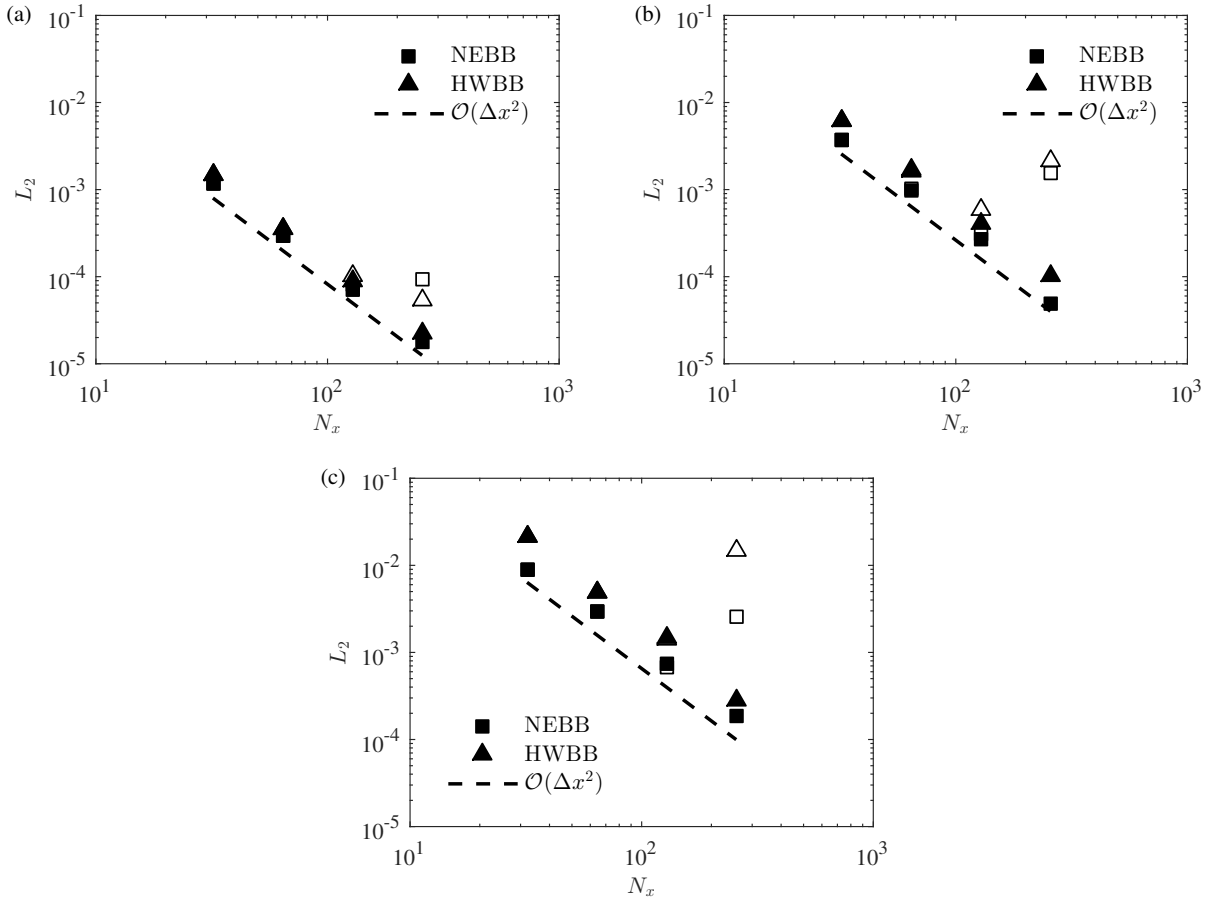

Source: the author.

4.1.2 Square Duct Poiseuille Flow

The leap from 2D to 3D in LBM requires many implementations and it is an essential demonstration of control over the numerical method. The square duct Poiseuille flow of a Bingham fluid was the test case selected for this purpose. Figure 4.5 shows a schematic of the problem. Inside a square duct with half-length L, a Bingham fluid flows due to a constant body force F_z. East and west boundaries are periodic, since the flow field is assumed to be fully developed. Saramito and Roquet (2001) approached this problem with the augmented Lagrangian method (ALM) and a specific mixed finite element method. In their work, the localization of yield surfaces was approximated by an anisotropic auto-adaptive mesh procedure. They defined the Bingham number as

$$Bn = \frac{2\sigma_y}{LF_z} \tag{4.7}$$

Figure 4.5 – Physical representation of the square duct Poiseuille flow. The flow is driven by a body force F_z. Front, back, south and north walls are stationary.

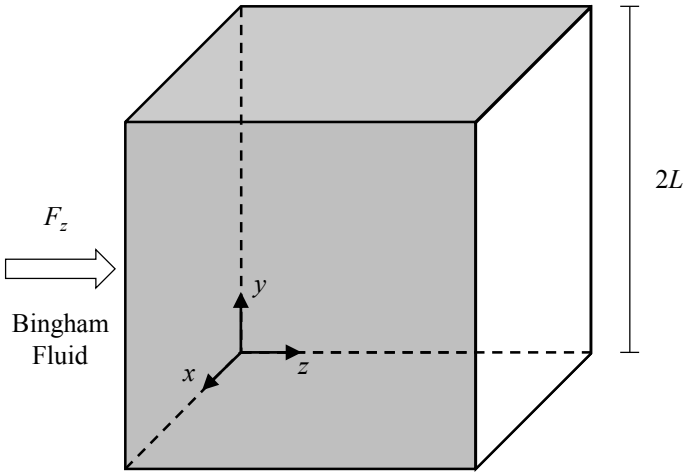

Source: the author.

This problem was solved by the presently proposed viscoplastic LB scheme with regularization of ghost moments and D3Q19 lattice. The halfway bounce-back (HWBB) boundary condition was imposed on the stationary walls, and periodic condition on inlet/outlet. The spatial grid was 128^3 in all simulations. The flow was enforced through a constant force term, calibrated such that the maximum velocity U_{max} was 0.05. The plastic Reynolds number Re_p does not influence this fully developed flow. It was determined such that the relaxation time at the plastic viscosity was approximately 0.88. Figure 4.6 compares the obtained mean and maximum velocities with approximate solutions from Saramito and Roquet (2001). A good agreement was obtained with LBM. A detailed flow field comparison against (SARAMITO and ROQUET, 2001) is shown in Figure 4.7. The auto-adaptive mesh of Saramito and Roquet (2001) is a costly computational procedure. The LBM is undoubtedly a competitive alternative for three-dimensional viscoplastic fluid flow simulations, in which the yield surface may assume complex shapes. The typical computational execution time of these simulations was 90 minutes. Considering that there were over two million nodes, the efficiency of the viscoplastic LB scheme on GPU is remarkable.

Figure 4.6 – Mean and maximum velocities as a function of Bn. Critical Bingham number (no flow) is $Bn_c = 1.07$. The velocity scale is defined as $U = L^2 F_z/(2\eta_p)$. Markers are results from the present work and lines are theoretical solutions.

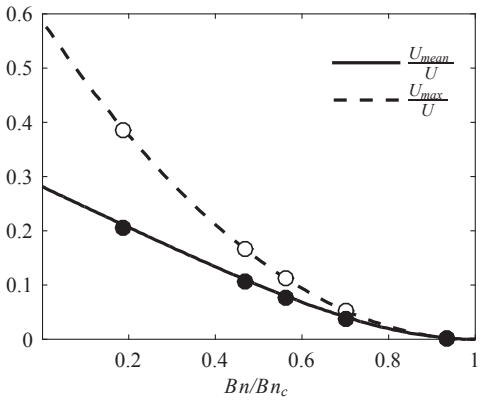

Source: the author.

Figure 4.7 – Comparison of velocity profiles from the present work (lines) and Saramito and Roquet (2001) (markers). (a) Along the median. (b) Along the diagonal.

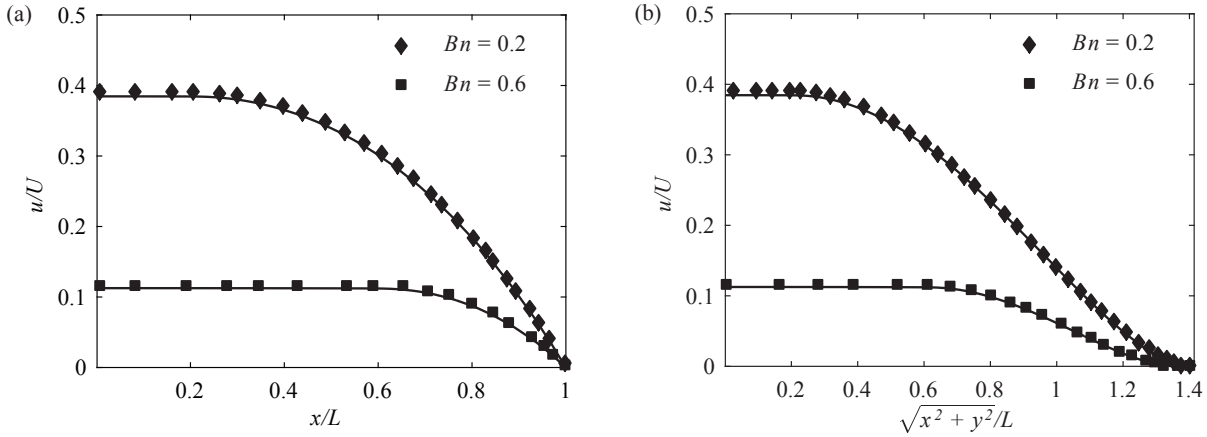

Source: the author.

The yielded and unyielded regions are shown in Figures 4.8 to 4.10. Comparisons are made with the viscoplastic LB scheme of Vikhansky (2008). The unyielded regions consist of dead zones in the corners and a moving "plug" in the center. It is interesting to note that the plug's shape changes from circular at low Bn to almost squared at high Bn. The yield surfaces from the present method are smoother, which may be due to the lower resolution (80^3) employed by Vikhansky (2008). Nonetheless, the quality of the obtained yield surfaces certainly builds up confidence in the present method.

Figure 4.8 – Yielded (white) and Unyielded (grey) regions for $Bn = 0.5$. Left: (VIKHANSKY, 2008). Right: present work.

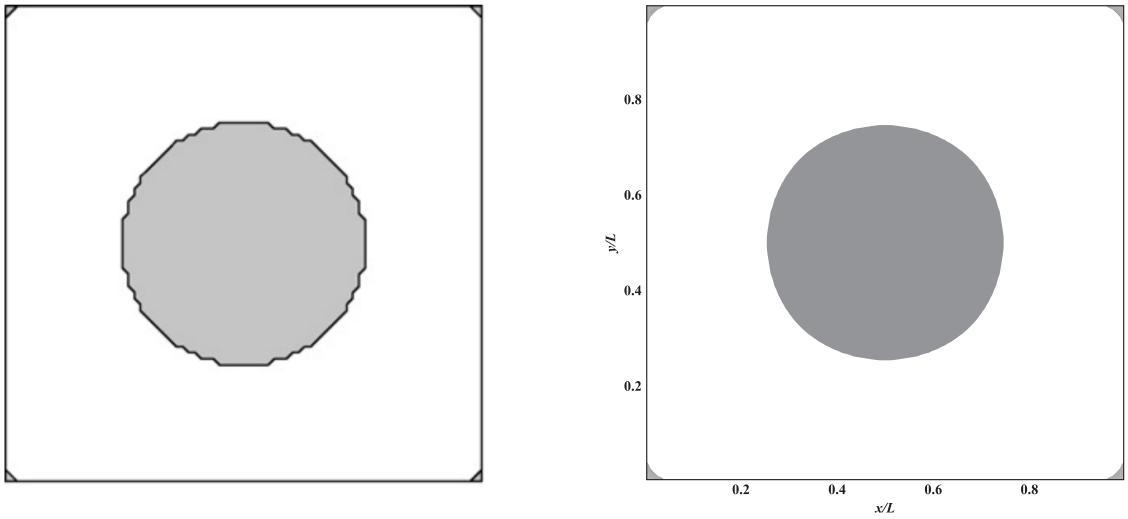

Source: the author and Vikhansky (2008).

Figure 4.9 – Yielded (white) and Unyielded (grey) regions for $Bn = 0.75$. Left: (VIKHANSKY, 2008). Right: present work.

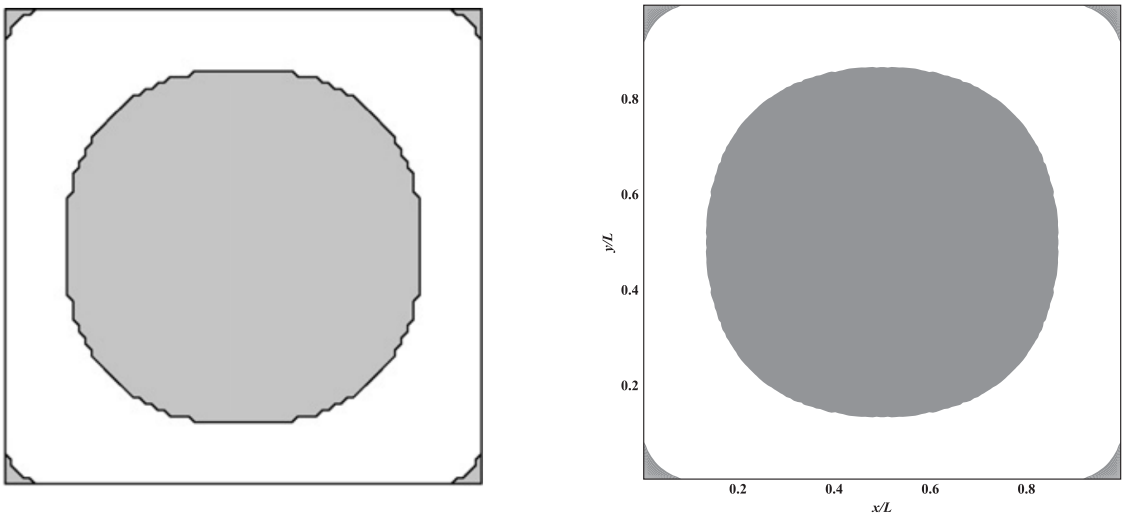

Source: the author and Vikhansky (2008).

Figure 4.10 – Yielded (white) and Unyielded (grey) regions for $Bn = 1$. Left: (VIKHANSKY, 2008). Right: present work.

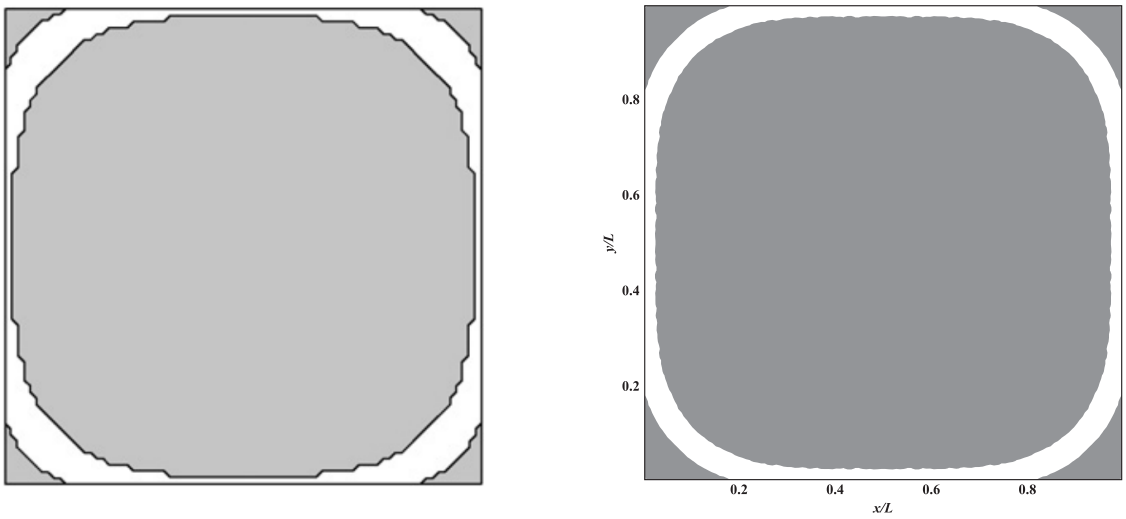

Source: the author and Vikhansky (2008).

4.1.3 Lid-Driven Cavity Flow

The lid-driven cavity flow is an interesting problem to study inertial effects. Since the geometry and boundary conditions are simple, it has become a benchmark case in computational fluid dynamics (GHIA et al., 1982; BOTELLA and PEYRET, 1998). An illustration of the problem is given in Figure 4.11. The squared enclosure has sides L and it is filled with Bingham fluid. All walls are stationary, except for the north wall, which moves horizontally with constant velocity U. The north wall's motion causes the fluid to recirculate inside the cavity.

Figure 4.11 – Physical representation of the lid-driven cavity flow. The north wall moves to the positive x-direction with constant velocity U.

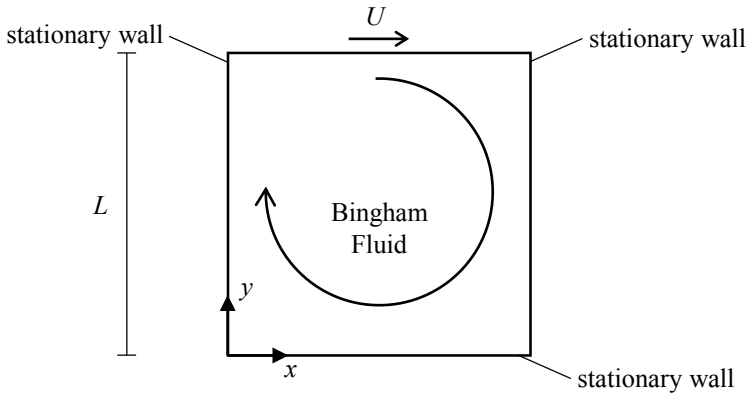

Source: the author.

Results from the present viscoplastic LB scheme will be compared with finite volume method (FVM) data available in the literature. The present LBM results were obtained with NEBB boundary condition,

for stationary and the moving walls, and D2Q9 lattice. Syrakos et al. (2013) defined the Reynolds number as $Re_p = \rho U L/\eta_p$ and the Bingham number as

$$Bn = \frac{\sigma_y L}{\eta_p U} \tag{4.8}$$

Figure 4.12 – Horizontal (x) velocity profile in the vertical mid-plane for $Re_p \to 0$ and $Bn = 50$. Comparison with FVM data of Syrakos et al. (2013). Present work results were obtained with a grid 128×128.

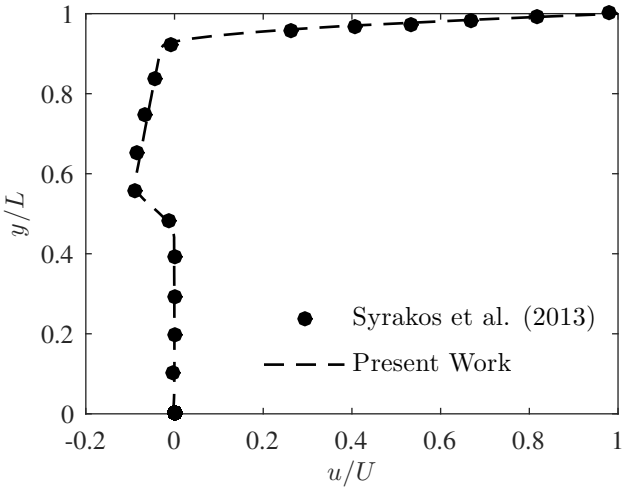

Source: the author.

The lid-driven cavity creeping flow ($Re_p \to 0$) was investigated in (SYRAKOS et al., 2013) with a Bingham model regularized according to Papanastasiou's expression. The x-velocity profile in the vertical mid-plane for $Bn = 50$ is shown in Figure 4.12. An excellent comparison was obtained for a grid 128×128. To reach creeping flow Reynolds number, the mesoscopic lid velocity had to be set very small. A value of approximately 10^{-4} was used. It should be noted that, again, small Ma divergence did not occur.

Figure 4.13 – Streamlines for $Re_p = 1000$ and $Bn = 0$. Left: Syrakos et al. (2014). Right: present work (grid 256×256).

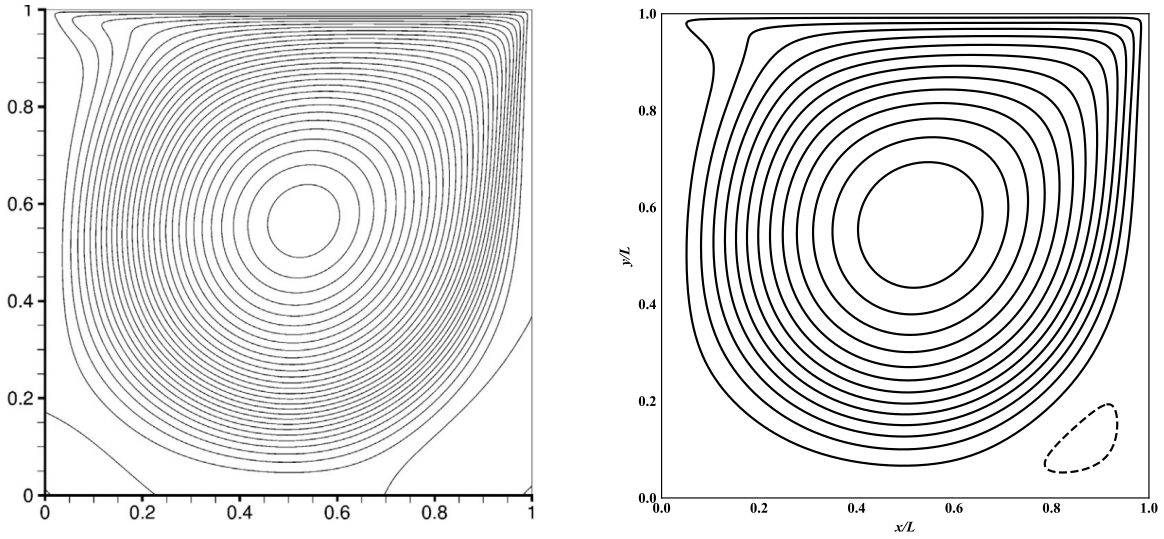

Source: the author and Syrakos et al. (2014).

Figure 4.14 – Streamlines and unyielded regions (grey areas) for $Re_p = 1000$ and $Bn = 1$. Left: Syrakos et al. (2014). Right: present work (grid 256×256).

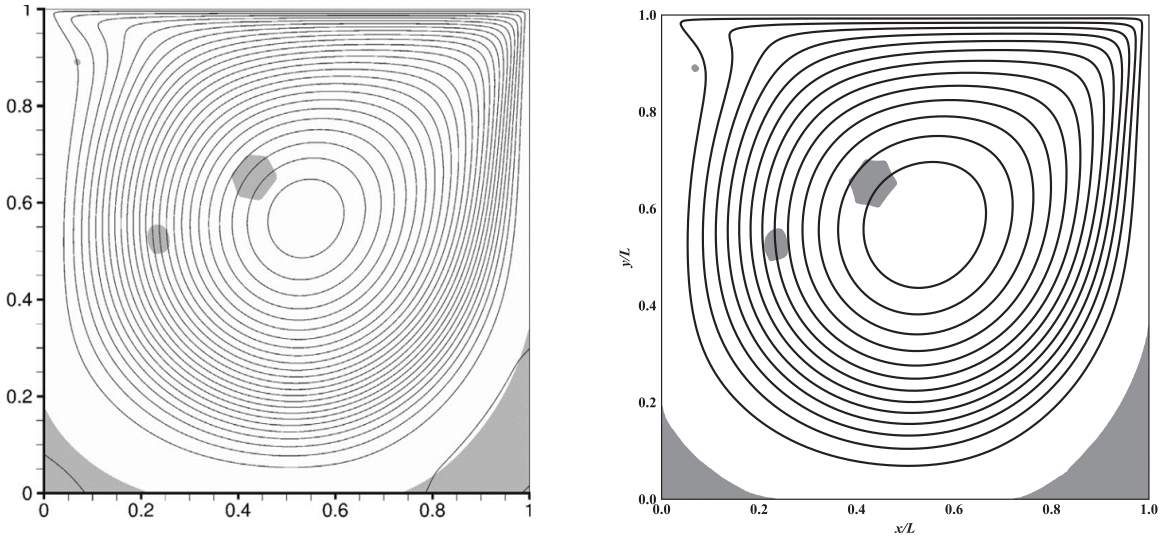

Source: the author and Syrakos et al. (2014).

The cited authors further extended their work to study inertial effects in (SYRAKOS et al., 2014). Reynolds numbers up to 5000 and Bingham numbers up to 100 were investigated with the same FVM scheme. Those results are much more interesting because the non-linearity of the inertial terms makes the numerical problem significantly harder. Figures 4.13 to 4.16 show streamlines and unyielded regions obtained from the present work. The streamlines in all cases are practically identical to those of Syrakos et al. (2014). For Newtonian fluid ($Bn = 0$) there is a weak counter-circulating region in the lower right side of the cavity. A similar structure also exists in the lower left side, but it has a much lower stream function value. When the fluid is viscoplastic, the counter-circulating regions disappear, because the unyielded fluid in the lower corners is stationary.

Figure 4.15 – Streamlines and unyielded regions (grey areas) for $Re_p = 1000$ and $Bn = 10$. Left: Syrakos et al. (2014). Right: present work (grid 256×256).

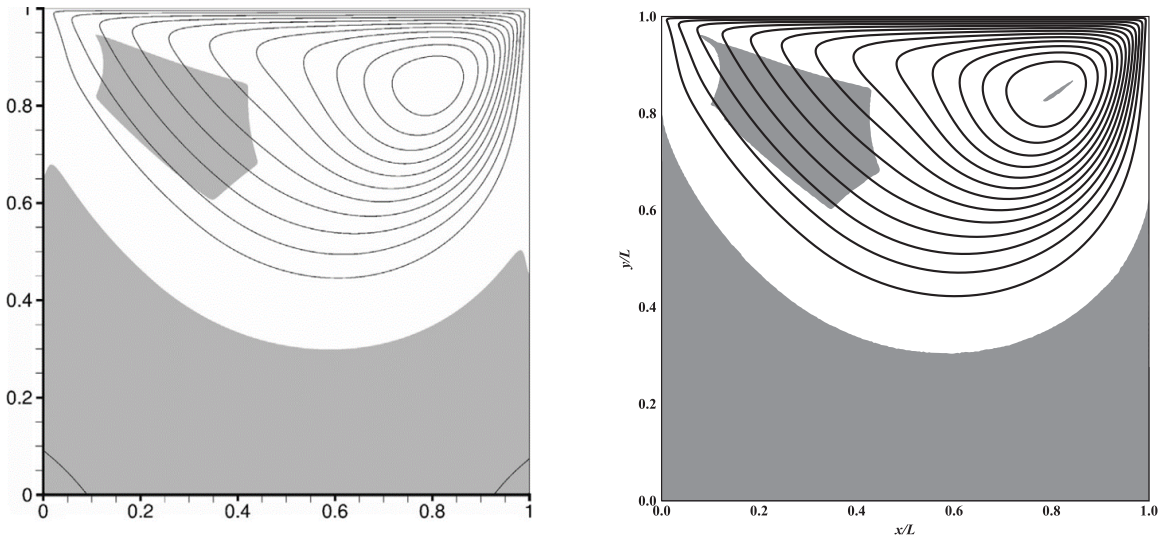

Source: the author and Syrakos et al. (2014).

Figure 4.16 – Streamlines and unyielded regions (grey areas) for $Re_p = 1000$ and $Bn = 100$. Left: Syrakos et al. (2014). Right: present work (grid 512×512).

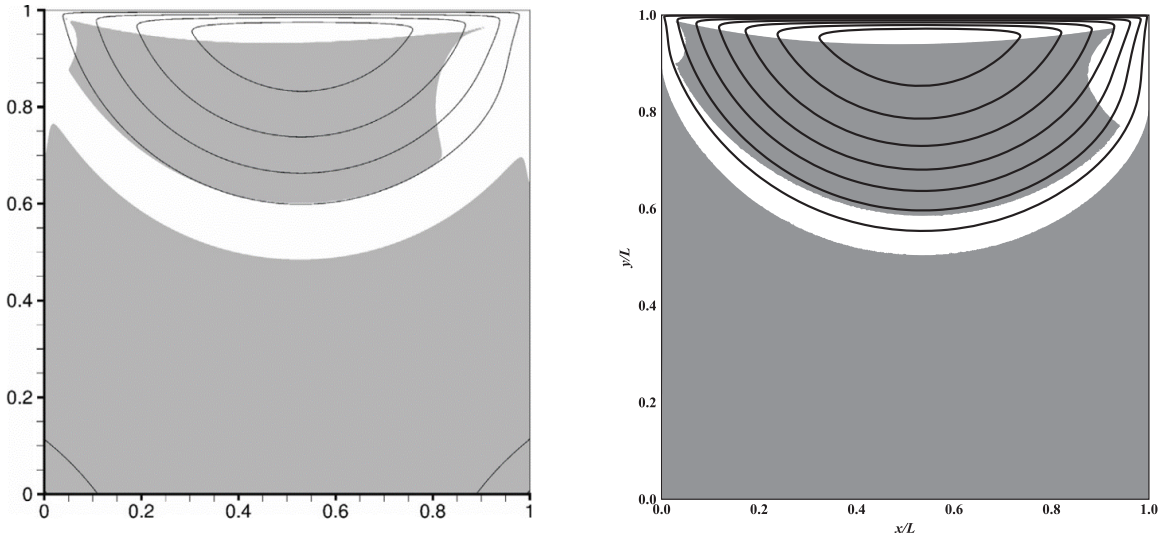

Source: the author and Syrakos et al. (2014).

Overall, the unyielded regions compare well with (SYRAKOS et al., 2014). Both shape and size of the unyielded portions are similar, except for the region joining the yield surface with the lateral walls. In the work of Syrakos et al. (2014) the yield surface did not connect tangentially to the lateral walls for $Bn = 10$ and $Bn = 100$. Based on experimental works that have investigated similar configurations (de Souza Mendes et al., 2007; LUU et al., 2017), there is no reason to suspect that such irregularity near the wall is a physical feature. ALM results of Dimakopoulos et al. (2018) also show a tangential connection to the walls (not plotted here because they neglected inertial terms). Therefore, it can be argued that the monotonic behavior is physically plausible and the yield surface shape obtained in the present work is credible. As a means to give a quantitative comparison, the vortex center locations and the maximum stream function were computed. Their comparison is shown in Table 4.1. The numerical agreement is clear, suggesting that the proposed LB scheme is able to solve inertial viscoplastic flow as well as FVM. In the reference works of Syrakos et al. their numerical method was subject to stringent stability and accuracy enhancements. It should be highlighted that both methods resulted in similar outcomes, even though they are intrinsically unrelated in terms of their fundamentals.

Table 4.1 – Vortex center position (x_c, y_c) and maximum stream function (ψ_{max}) normalized by U and L from Syrakos et al. (2014) and present work.

		Syrakos et al. (2014)			Present work		
Re_p	Bn	x_c	y_c	ψ_{max}	x_c	y_c	ψ_{max}
1000	0	0.531	0.564	0.119	0.529	0.565	0.119
1000	1	0.539	0.567	0.103	0.537	0.569	0.103
1000	10	0.796	0.850	0.047	0.796	0.851	0.047
1000	100	0.535	0.950	0.019	0.534	0.949	0.020

Source: the author.

4.2 Transient Problems

The transient character of the proposed LB scheme is assessed in this section. Unlike in the steady-state simulations, for the transient cases presented hereafter, the relaxation frequency is exactly solved in each time iteration by Equation 3.21. Analytical solutions for transient laminar flows of viscoplastic fluid are rare. However, an approximate solution for startup flow of Bingham fluid in parallel plates is used for transient assessment in Section 4.2.1. Moreover, in Section 4.2.2, the finite stopping time of a Bingham fluid flow is investigated with the proposed viscoplastic LB scheme.

4.2.1 Startup Flow in Parallel Plates

The definition of the startup flow in parallel plates is as follows. A Bingham fluid is initially at rest between two infinite parallel plates separated by a distance $2h$. At an instant $t = 0$ a force G is applied transversal to the wall-normal (y) direction, causing the viscoplastic fluid to accelerate, until steady-state is reached. The region of interest is too far away from any inlet or outlet. Thus, this flow is assumed to be fully developed. Also, the flow is symmetrical about the centerline, located at $y = 0$. At any instant $t > 0$ the velocity profile consists of a unyielded region with velocity $u_p(t)$, and a yielded region with velocity $u(y, t)$, such that the yield surface delimiting the two regions is located at $y/h = \delta < 1$.

Safronchik (1959) obtained an approximate solution for very short times. The location of the yield surface is

$$\delta(t^*) = 1 - 2a\sqrt{t^*}, \qquad t^* \leq t_1 \tag{4.9}$$

where $t^* = t/(\rho h^2/\eta_p)$, $t_1 = 1/4a^2$, and a is the solution for the following transcendental equation

$$e^{-a^2} - a\sqrt{\pi}\,[1 - \mathrm{erf}(a)] = Bn/G^* \tag{4.10}$$

The Bingham number is defined as $Bn = \sigma_y h/\eta_p\sqrt{\sigma_y/\rho}$, the non-dimensional force density is $G^* = G/(\eta_p\sqrt{\sigma_y/\rho}/h^2)$, and $\mathrm{erf}(\sim)$ is the error function.

In a recent work Huilgol et al. (2019) demonstrated that Equation 4.9 is actually valid for a shorter time $t \leq t_3 = (1 - Bn/G^*)^2/4a^2$. Moreover, they found alternative approximate solutions for the velocities in the yielded and plug regions. It was verified that the predicted plug velocity of Safronchik (1959) and Huilgol et al. (2019) only matched for very small Bn/G^* ratios. It is unclear which one is more accurate.

This problem was solved by the presently proposed viscoplastic LB scheme with regularization of ghost moments and D2Q9 lattice. The halfway bounce-back (HWBB) boundary condition was imposed on the stationary walls, and periodic condition on inlet/outlet. The spatial grid had 256 nodes in the normal direction in all simulations. The relaxation time at the plastic viscosity was approximately 0.65. The flow field was initialized according to the procedure of Section 3.1.2, with velocity and stress equal to zero. A constant force term was imposed from the beginning, determined such that the target steady-state average velocity U was 0.1.

Transient velocity profiles are shown in Figures 4.17 to 4.20 for various Bn/G^* ratios. The non-dimensional velocity was defined by $u^*(y, t) = u(y, t)/\sqrt{\sigma_y/\rho}$, and the non-dimensional vertical coordinate was defined by $y^* = y/h$. Since the approximate solutions presented above are only valid for

very short times, a time t_{09} was defined by how long the yield surface took to be at $\delta = 0.9$. The time to reach steady-state was denominated t_f. It can be seen from the figures that, in general, the numerical results were very regular. A plug region is clearly distinguishable from the profiles. Moreover, the correct steady-state solution was reached in all cases. For very small Bn/G^* ratios, both approximate solutions agree with the numerical results, as seen from Figure 4.17. However, in Figure 4.18, only Huilgol et al. (2019) gives a good match with the simulations, while the plug velocity approximation of Safronchik (1959) deviates from the numerical results as time advances.

Figure 4.17 – Velocity profile evolution of startup flow in parallel plates for $Bn/G^* = 0.001$. Markers are the numerical results from the present work. Time advances from lighter to darker blue. (a) Profiles at ten different times equally spaced up to t_{09}. The solid lines are approximate solutions of Safronchik (1959) in the plug region, and Huilgol et al. (2019) in the yielded region. (b) Profiles at ten different times with equal intervals up to t_f. The dashed line is the exact steady-state solution.

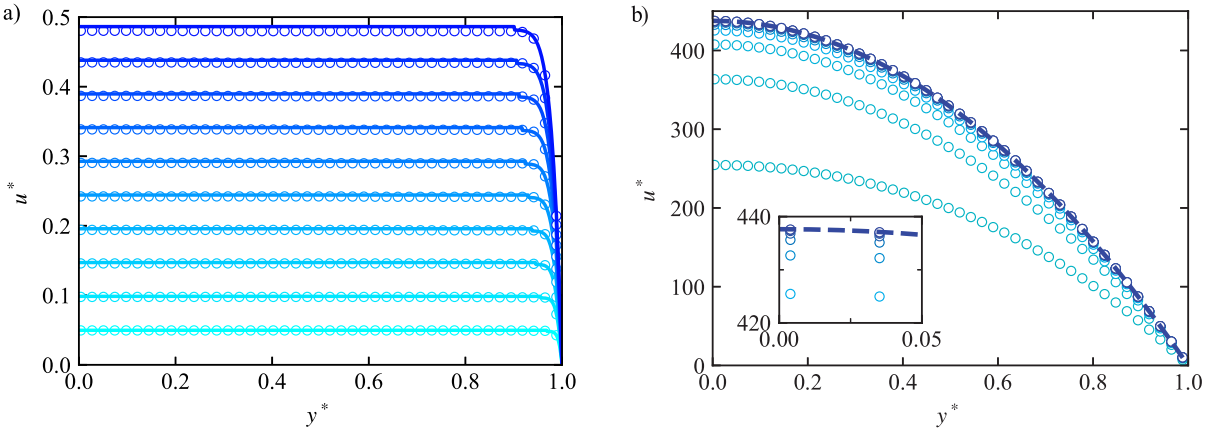

Source: the author.

The observation to be done in this case is that, with increasing Bn/G^*, the solutions of Safronchik (1959) and Huilgol et al. (2019) increase their discrepancies. In Figure 4.19, the solution of Huilgol et al. (2019) is still very well matched by the simulations. On the other hand, the solution of Safronchik (1959) does not match neither. It could be that Safronchik (1959) solution is good, while both Huilgol et al. (2019) and the present results are not. This can only be verified by another numerical method, such as ALM. Nevertheless, the smoothness of the profiles is generally a good sign in numerical methods. For the computationally stiff case of $Bn/G^* = 0.8$, shown in Figure 4.20, neither approximate solutions agree with the numerical results.

In Figure 4.19 it is seen that the velocity profile in the plug region is nor perfectly flat. Ideally, the unyielded region would be found in post-processing by checking for nodes with $\omega = 0$. It turns out that the ratio $\sigma_y/|\boldsymbol{T}|$ in Equation 3.21 is subject to inevitable numerical errors present in the populations that compose the tensor component $T_{\alpha\beta}$. The most significant of these errors are those due to time-space discretization. Even the slightest error will prompt Equation 3.21 to attribute a finite value for ω in a unyielded node. The numerical values that the relaxation frequency assumes in unyielded nodes were verified to be order-of-magnitude below typical ω values in yielded nodes. This inconvenience does not jeopardize the velocity field, as can be inferred from the quality of the transient profiles, and the accuracy of the steady-state profiles. However, the delimitation of the yield surface is not straightforward.

Figure 4.18 – Velocity profile evolution of startup flow in parallel plates for $Bn/G^* = 0.01$. Markers are the numerical results from the present work. Time advances from lighter to darker blue. (a) Profiles at ten different times equally spaced up to t_{09}. The solid lines are approximate solutions of Safronchik (1959) in the plug region, and Huilgol et al. (2019) in the yielded region. (b) Profiles at ten different times with equal intervals up to t_f. The dashed line is the exact steady-state solution.

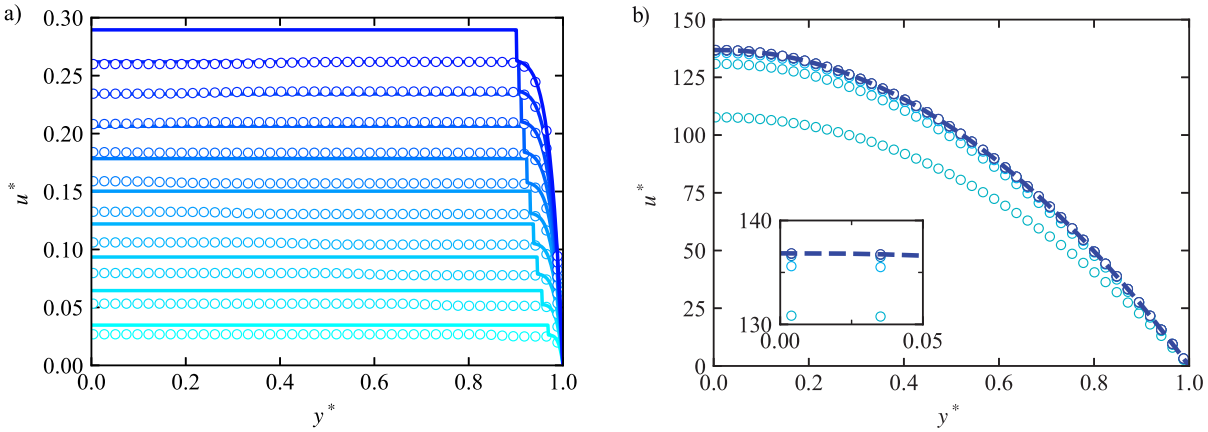

Source: the author.

Figure 4.19 – Velocity profile evolution of startup flow in parallel plates for $Bn/G^* = 0.1$. Markers are the numerical results from the present work. Time advances from lighter to darker blue. (a) Profiles at ten different times equally spaced up to t_{09}. The solid lines are approximate solutions of Safronchik (1959) in the plug region, and Huilgol et al. (2019) in the yielded region. (b) Profiles at ten different times with equal intervals up to t_f. The dashed line is the exact steady-state solution.

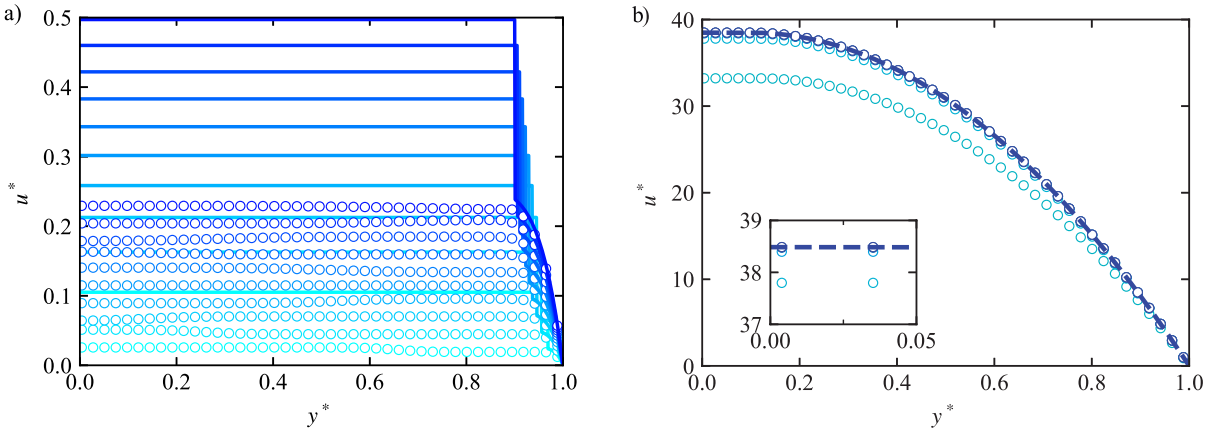

Source: the author.

Figure 4.20 – Velocity profile evolution of startup flow in parallel plates for $Bn/G^* = 0.8$. Markers are the numerical results from the present work. Time advances from lighter to darker blue. (a) Profiles at ten different times equally spaced up to t_{09}. The solid lines are approximate solutions of Safronchik (1959) in the plug region, and Huilgol et al. (2019) in the yielded region. (b) Profiles at ten different times with equal intervals up to t_f. The dashed line is the exact steady-state solution.

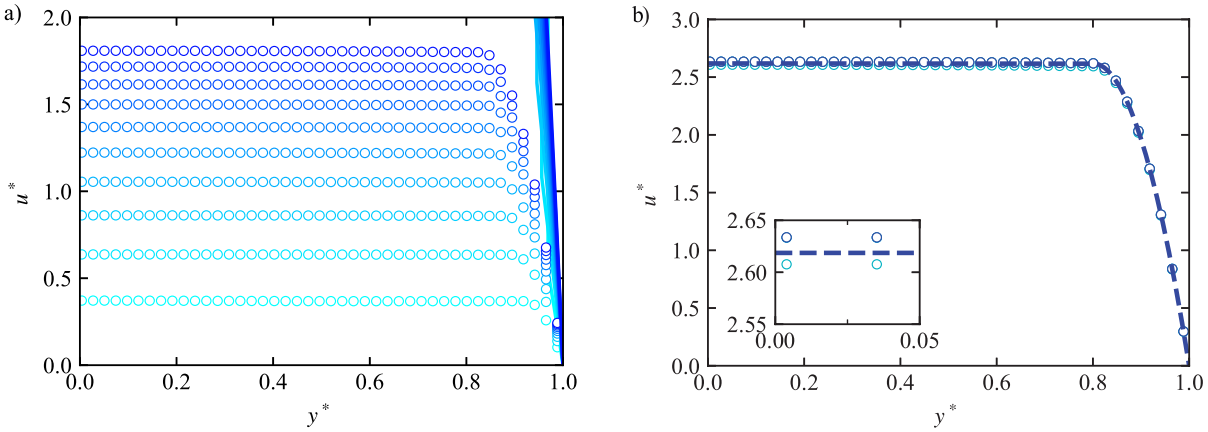

Source: the author.

A few alternatives were tested for the definition of a cut-off value for the relaxation frequency. What worked best was the idea that, in steady-state, the node located at $y^* = \delta + \Delta y^*$ must be yielded (Δy^* is the vertical grid spacing). So, the analytical solution for the viscosity profile provides a solution for $\eta(\delta + \Delta y^*)$, which is considered to be the cut-off value:

$$\eta_{\text{cut-off}} > \eta_p \left(1 + \frac{Bn/G^*}{\Delta y^*}\right) \tag{4.11}$$

Thus, $\omega_{\text{cut-off}}$ comes from inputting $\eta^- = 1/\eta_{\text{cut-off}}$ in Equation 3.14.

Figure 4.21 – Temporal evolution of plug velocity (blue) and yield surface location (magenta). Markers are the numerical results from the present work. The solid lines are approximate solutions of Safronchik (1959), while dashed lines are the exact steady-state solutions. Insets show numerical and theoretical behavior at very short times. (a) $Bn/G^* = 0.001$. (b) $Bn/G^* = 0.01$. (c) $Bn/G^* = 0.1$. (d) $Bn/G^* = 0.8$.

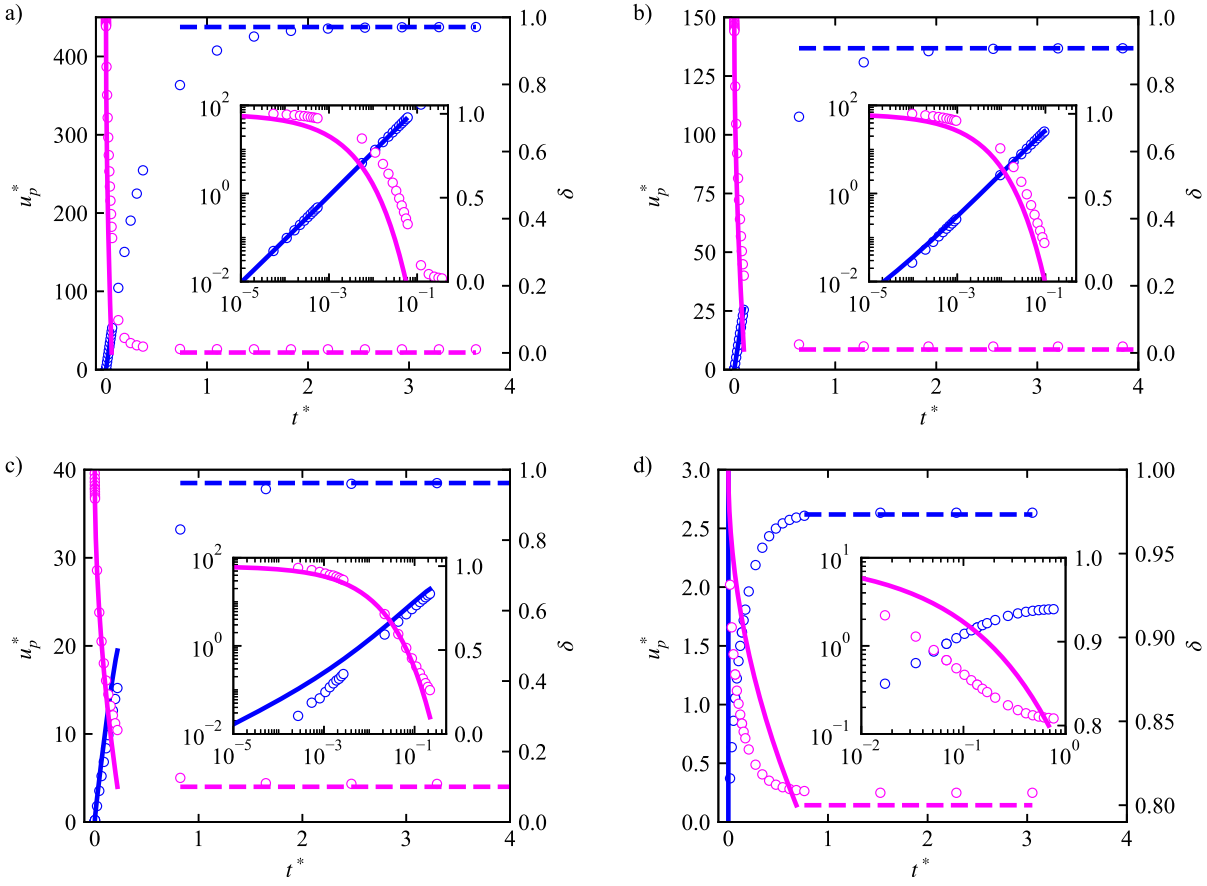

Source: the author.

The temporal evolution of plug velocity and yield surface location is shown in Figure 4.21, and a comparison is made against the approximate solution of Safronchik (1959). At very short times, the numerical results behave very much alike the approximate solutions, except for $Bn/G^* = 0.8$. The quantitative agreement varies for different Bn/G^* ratios and time ranges. It is interesting to note that the time to reach steady-state was approximately $t^* = 2$ for Bn/G^* up to 0.1, while for $Bn/G^* = 0.8$ it was about 1. Even though there was no good agreement with Safronchik's solution for the case $Bn/G^* = 0.8$, it is unclear whether his solution is valid for such a high ratio. In the work of Huilgol et al. (2019), the authors make it clear that their solution only matches Safronchik's for very small Bn/G^* ratios. The

numerical solutions obtained with the proposed viscoplastic LB scheme approach the steady-state quite smoothly, and do not show any worrisome irregularity.

4.2.2 Stopping Flow in Parallel Plates

When a Newtonian fluid undergoing steady motion in a pipe of arbitrary cross-section has its driving force suddenly removed, the flow velocity approaches zero as $t \to \infty$. A fundamental difference between a Newtonian and a Bingham fluid is that the Bingham fluid comes to a halt in a *finite* amount of time. This theoretical prediction was obtained by Glowinski (1984) using variational inequality of kinetic energy, and it was later refined by Huilgol et al. (2002). In this section the stopping flow of a Bingham fluid between parallel plates is numerically investigated. The problem definition is as follows. A Bingham fluid is initially flowing with steady-state properties, as given in Section 4.1.1. At an instant $t = 0$ the driving force is suddenly removed, causing the viscoplastic fluid to decelerate towards rest state. The same geometrical considerations and coordinates of the startup flow case are assumed (Sec. 4.2.1). The theoretical upper-bound for the stopping time (T_f), normalized by the time scale $\rho h^2/\eta_p$, is (HUILGOL et al., 2002)

$$T_f \leq \frac{4}{\pi^2} \ln \left[1 + \frac{\pi^2}{4} \frac{\|u(y,0)\|/U}{Bn} \right] \tag{4.12}$$

where $Bn = \sigma_y h/\eta_p U$, U is the average steady-state velocity, and

$$\|u(y,0)\| = \left[\frac{1}{h} \int_0^h u^2(y,0) dy \right]^{1/2} \tag{4.13}$$

This problem was solved by the presently proposed viscoplastic LB scheme with regularization of ghost moments and D2Q9 lattice. The halfway bounce-back (HWBB) boundary condition was imposed on the stationary walls, and periodic condition on inlet/outlet. The spatial grid had 256 nodes in the normal direction in all simulations. The relaxation time at the plastic viscosity was approximately 0.65. The flow field was initialized according to the procedure of Section 3.1.2, with velocity profile from Equations 4.4 and 4.5 with $U = 0.1$, and linear shear stress profile from the centerline to the wall.

The evolution of the volumetric flow rate Q is shown in Figure 4.22a. The Newtonian decay was constant up to the machine error level ($Q \geq 10^{-15}$). The viscoplastic material behaved differently. Their initial decay was Newtonian-like, but at some point it transitioned to a steep decrease, which characterizes the finite stopping time. Shorter transition times are seen for higher Bn, corresponding to higher yield stress. The viscoplastic curves in Figure 4.22a are truncated because the velocity values did not reach the machine error level. Instead, the velocities changed the signal at a residual value, due to some numerical artifact related to the periodic boundary condition. The numerical stopping time T_f was defined at the moment that the velocity had its signal changed. It is important to mention that, when this happened, ω was already zero throughout the entire domain.

Figure 4.22 – Numerical results for the influence of Bn on the finite stopping time. (a) Evolution of the volumetric flow rate normalized by $2hU$. The markers are ALM solutions of Muravleva et al. (2010), while the lines are LBM results from the present work. The black line is $Bn = 0$ (Newtonian). (b) Computed stopping time *versus* theoretical prediction.

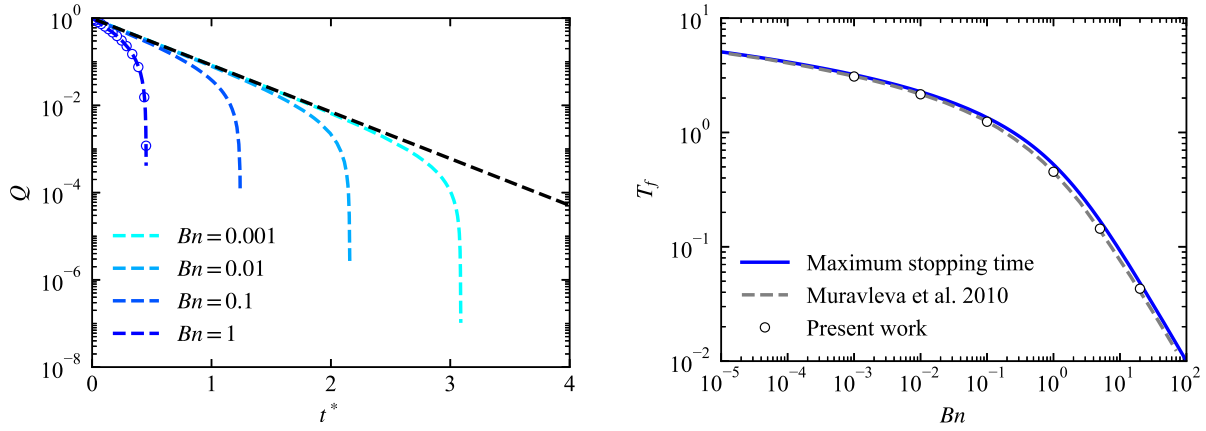

Source: the author.

Figure 4.23 – Velocity profile evolution of stopping flow in parallel plates ($u^* = u/U$). Markers are the numerical results from the present work and the lines are initial (steady-state) profiles. Time advances from lighter to darker blue. The numerical results are shown for three different times: one iteration, $T_f/10$, and $T_f/2$. (a) $Bn = 0.001$. (b) $Bn = 0.1$. (c) $Bn = 5$.

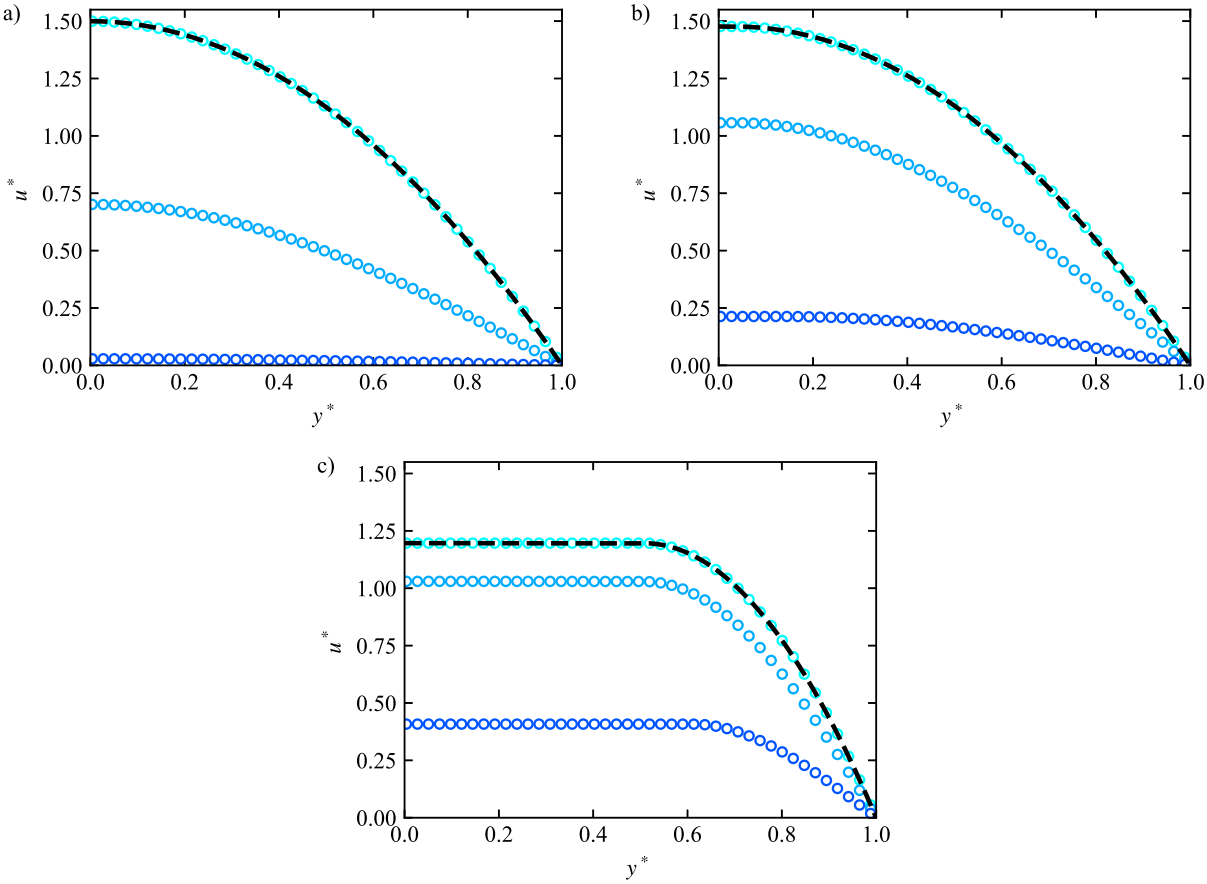

Source: the author.

The stopping times are plotted in Figure Figure 4.22b. The stopping times computed with the proposed viscoplastic LB scheme were always shorter than the theoretical upper-bound of Equation 4.12. A

very good agreement with ALM solutions of Muravleva et al. (2010) is verified. It is curious to note that, not only do the numerical stopping times obey the theoretical upper-bound, but they also conform to the shape of Equation 4.12. In Figure 4.23 the evolution of the velocity profiles is shown. There is no visible irregularity or unexpected behavior. It can be seen that a plug region develops and its size increases with time.

The evolution of the yield surface location δ was also relatively smooth, as seen in Figure 4.24. The yield surface delimitation criteria was the same as in the startup case, Equation 4.11. Initially, δ has its steady-state value. It increases slightly in the beginning. Then, when it is about 0.8, the expansion towards the wall is quite sudden. Numerical results of ALM are compared with the present LB scheme, for $Bn = 5$ and $Bn = 20$. The ALM is known to be a very accurate method for capturing yield surface location. The agreement with LBM was excellent, which indicates that the choice for $\eta_{\mathrm{cut-off}}$ was appropriate.

Figure 4.24 – Evolution of yield surface location of stopping flow in parallel plates. The markers are ALM solutions of Muravleva et al. (2010), while the lines are LBM results from the present work.

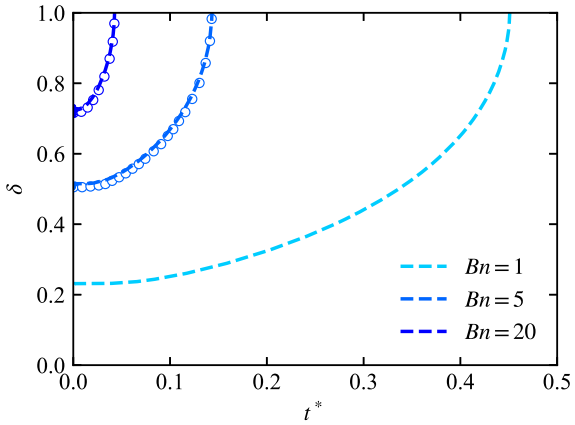

Source: the author.

4.3 Conclusions

In this chapter, the proposed viscoplastic LB scheme was put to the test in steady and transient flows of Bingham fluid. With respect to accuracy, the second-order error decay was verified, indicating that the discretization order of the standard LBM is sustained. A thorough comparison with ALM was not the scope of the present investigations. Nevertheless, for the cases solved, it is safe to say that the quality of the yield surfaces obtained was comparable with ALM. A cut-off viscosity value was defined in order to find the yield surfaces, which proved to perform well in the transient cases simulated. The viscosity treatment for the transient flows resulted in smooth velocity profiles. The theoretical predictions for transient flows were well represented.

The present method has excellent stability characteristics, thanks to the regularization of ghost moments. As far as computational efficiency is concerned, the most important characteristics of the standard LBM were kept. The locality of the method is respected, including in the stress tensor evaluation, which is obtained from moments of the non-equilibrium populations. As a consequence, the implementation in GPU resulted in a performance of around 400 million lattices updates per second. The three-dimensional

simulations of the square duct Poiseuille flow were typically executed in 90 minutes, for a computational domain of over two million nodes.

It is unlikely that the present viscoplastic LB scheme will outperform ALM in terms of yield surface location accuracy, because of its intrinsic formulation. However, the results presented in this chapter give many reasons to believe it can be a valuable engineering tool in the industry of viscoplastic materials. Further work is recommended to quantify and compare the numerical results of ALM and LBM in a set of benchmark Bingham flows.

5 TURBULENT CHANNEL FLOW

The LB scheme for viscoplastic fluid flow described in Chapter 3 and validated in Chapter 4, is now employed in direct numerical simulations (DNS) of turbulent flow in a channel filled with a Bingham fluid. As illustrated in Figure 5.1, the channel dimensions are $2\delta \times 2\delta \times 16\delta$ in the spanwise, normal and streamwise directions, respectively. The walls are separated by a distance 2δ, where δ is the channel half-height, and are represented by the halfway bounce-back boundary condition. The flow in the stream and spanwise directions is considered homogeneous in a fully turbulent flow. Hence, periodicity is imposed as boundary condition. The flow is driven by a constant body force density F_z (N/m ^{3}). The instantaneous and the time-averaged equations of the Bingham fluid turbulent flow have been given in Section 2.5.1.1.

Figure 5.1 – Channel's dimensions and coordinates. The flow is driven in the z direction (streamwise). The x direction is transversal (spanwise) and the normal direction is y.

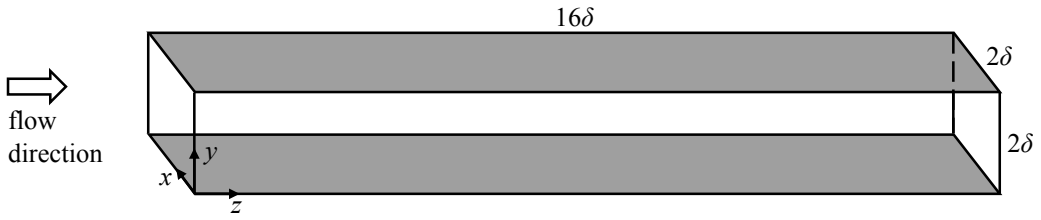

Source: the author.

5.1 Simulation Setup

In internal turbulent flows, it is conventional to use as non-dimensional parameter the friction Reynolds number, defined as $Re^* = \rho u^* \delta / \mu$, where u^* is the friction velocity (KIM et al., 1987; EGGELS et al., 1994; JIMENEZ and HOYAS, 2008). The friction velocity is representative of the mean wall shear stress $\overline{\sigma}_{\mathrm{w}}$:

$$u^* = \sqrt{\frac{\overline{\sigma}_{\mathrm{w}}}{\rho}} \tag{5.1}$$

However, the Newtonian viscosity μ has no place in this case study. In this work, the friction Reynolds number is defined with the plastic viscosity

$$Re^* = \frac{\rho u^* \delta}{\eta_p} \tag{5.2}$$

A bulk Reynolds number $Re_b = 2\rho U_b \delta / \eta_p$ can also be defined, where $U_b = (1/2\delta) \int_0^{2\delta} \overline{u}_{\mathrm{z}}\, dy$, but it is not known *a priori*. Some authors have defined Re^* with the mean wall viscosity $\overline{\eta}_{\mathrm{w}}$ (SINGH et al., 2017a). In contrast, the decision to use η_p allows the friction Reynolds number to be independent of the yield stress σ_y. In the present work, Re^* is fixed at 180. Since $Re^* = 180$ and $\rho = 1$ are determined, two of the three quantities in the right-hand side of Equation 5.2 are free to be set.

For the flow to stay in an incompressible regime, the Mach number $Ma = U/c_s$ must be low. A typical limit used in aerodynamics simulations is 0.3 (Anderson JR, 2010). In turbulent channel flow the highest velocity, on average, takes place at the centerline. For a Newtonian fluid at $Re^* = 180$, the mean centerline velocity U_c/u^* is approximately 18.2 (KIM et al., 1987). It is expected that the centerline velocity for a viscoplastic fluid will be a little higher (ROSTI et al., 2018). Hence, a possible centerline velocity U_c/u^* of 19 is considered. Velocity magnitudes higher than 0.2 (in lattice units, l.u.) must be avoided in LBM, due to its velocity space discretization. In the present work, the friction velocity is designed for a mean centerline velocity of 0.11 (l.u.), which gives $Ma = 0.11/(1/\sqrt{3}) = 0.19$ and $u^* = 0.11/19 = 0.00579$ (l.u.).

The smallest length scale in a turbulent flow is given by the Kolmogorov microscale $l^+ \sim (\varepsilon^+)^{-1/4}$, where ε is the dissipation rate of the turbulent kinetic energy and the superscript "+" refers to the Newtonian wall scales for velocity ($u^+ = u/u^*$) and space ($y^+ = y/(\mu/\rho u^*)$). It is expected that the viscoplastic fluid will have a lower ε than the Newtonian. Therefore, the spatial resolution is going to be designed as if the viscoplastic fluid was a Newtonian with $\mu = \eta_p$. This decision will be analyzed *a posteriori*. In Newtonian turbulent channel flow, the maximum dissipation rate ε^+ takes place at the walls and has an approximate value of 0.2 (KIM et al., 1987). Consequently, the grid size must be of the order $l^+ \sim 1.5$. Previous DNS of turbulent channel flows suggest that three grid nodes inside the viscous sublayer ($y^+ \leq 8$) give a sufficient spatial resolution (EGGELS et al., 1994; LAMMERS et al., 2006), which corresponds to $\Delta y^+ \approx 2.3$. The spatial resolution in wall units $\Delta y^+ = \rho u^* \Delta y/\mu$ is, according to the friction Reynolds number definition, equal to $Re^* \Delta y/\delta$. It must be noticed that in LBM $\Delta y = 1$. Thus, 2δ is equal to the number of grid nodes in the normal direction, so δ is an integer. In the present work δ is set to 98, which corresponds to $\Delta y^+ \approx 1.8$. With the halfway bounce-back boundary condition for the walls, the first grid node after the wall is at $\Delta y/2$ (see Fig. 3.2). This grid sizing provides five grid nodes within $y^+ \leq 8.2$.

An integral force balance in the domain gives

$$F_z = \frac{\overline{\sigma}_\mathrm{w}}{\delta} \tag{5.3}$$

Therefore, since both u^* and δ are constant, the driving force is also constant. Throughout the different cases investigated the fluid has the same plastic viscosity, determined by Equation 5.2, and only the yield stress is varied. The Bingham number is defined as

$$Bn = \frac{\sigma_y}{\overline{\sigma}_\mathrm{w}} \tag{5.4}$$

The Bn values investigated are 0 (Newtonian), 0.05, 0.10 and 0.15. A simulation with $Bn = 0.20$ was performed but it re-laminarized after a short time. It was then removed from the present discussion.

5.1.1 Computational Aspects

Regarding numerical stability, the broad spectrum that the relaxation frequency can assume in this viscoplastic turbulent flow was the most challenging aspect. The relaxation frequency was allowed to vary from 0 (unyielded material) to 1.9629 ($\tau_p = 1/1.9629 = 0.5095$). Fortunately, the implementation of regularization of ghost moments has proved effective in allowing stable simulations in all attempted

cases. The Courant–Friedrichs–Lewy number CFL = $\Delta t(u_x + u_y + u_z)/\Delta x$ is naturally low in LBM, because the velocity components are of order 10^{-1} and $\Delta x/\Delta t$ is unitary.

A Newtonian turbulent flow was initialized with the laminar solution (parabola) with $U_c = 0.11$, superposed with random perturbations in all components. Gaussian random values were generated with mean 0 and standard deviation 1, and then multiplied by 10% of the nominal bulk velocity, before being added to the velocity components. After approximately 40 eddy turn-over times (ETT $= \delta/u^*$) the flow became statistically fully developed. A different strategy was used to initialize the viscoplastic cases. The initial field of $Bn = 0.05$ was a fully developed field from $Bn = 0$, the initial field of $Bn = 0.10$ was a fully developed field from $Bn = 0.05$, and so on. The viscoplastic flow field became statistically fully developed in a similar period.

The numerical time-step corresponded to ETT/16927. In terms of flow-through time (FTT $= 16\delta/U_b$), the time-step was FTT/17411. In order to avoid massive data storage requirements, volume averages were taken during the simulation, at each 1000 time-steps. The volume averages were taken along the x and z directions, during additional 40ETTs. Then, in post-processing, the time averages were computed, resulting in the expected ensemble averages.

The large domain size required 24Gb of GPU memory. This is far beyond capacity of popular GPUs. The simulations presented in this chapter were executed in a NVIDIA Tesla V100 32Gb, through a cloud computing service. The efficiency of the LBM implementation in this GPU was 1500 MLUPs (million nodes updated per second). The execution time for a single case, considering flow development plus fully developed phases, was 15 hours.

5.2 Instantaneous Fields

This section is dedicated to the presentation and interpretation of instantaneous flow variables. Figure 5.2 shows instantaneous streamwise velocity in the z–x (top view) and x–y planes. The z–x plane is located at the buffer layer, where the highest velocity fluctuations are expected. Increasing Bn elongates the low speed streaks in the streamwise direction and reduces the amount of high speed regions. From the x–y visualization, it seems that the low speed streaks were able to reach the same vertical extent, independently of the yield stress value. Clearly, for higher Bn the core region of the flow is more uniform with a high velocity. Small unyielded spots are seen for $Bn = 0.05$ and 0.10, and a large one for $Bn = 0.15$. In the z–x plane located at the buffer layer, no unyielded spots are observable.

Instantaneous viscosity contours are exhibited in Figure 5.3. The viscosity values were calculated by Equation 2.36. The z–x plane is located at the centerline, where the highest viscosity values are expected. The size of the unyielded regions increases significantly with Bn. For $Bn = 0.15$, there is a large unyielded region that takes up the entire x direction. The unyielded spots are always surrounded by a high viscosity volume. It can be noticed from the x–y planes that there is a thin layer near the wall in which those high viscosity volumes do not penetrate.

Figure 5.4 shows contours of instantaneous vorticity. Unlike the previous figures, the panels on the left show z–y planes (side view). For $Bn = 0$ the classical Newtonian turbulent vorticity field is recognized. Vorticity is very high near the walls. Streaky structures lean and stretch towards the core, where diffusion dampens them down. The yield stress has an effect of elongating the vortical structures. Since the dissipation of vorticity takes place in the core region, where the viscoplastic fluid's viscosity

is considerably high, the amount and intensity of vortical structures in this region are suppressed. It is worth noting that inside the unyielded spots the material experiences a rigid-body motion ($\dot{\gamma}_{\alpha\beta} = 0$), what does not necessarily imply zero vorticity.

Figure 5.2 – Contours of instantaneous streamwise velocity u_z. Magnitude increases from dark purple to light yellow. Left: z–x plane located at $y^+ \approx 10$ with u_z ranging from $2u^*$ to $16u^*$. Right: x–y plane with u_z ranging from 0 to $20u^*$. From top to bottom: $Bn = 0$, 0.05, 0.10 and 0.15. Black spots are unyielded regions.

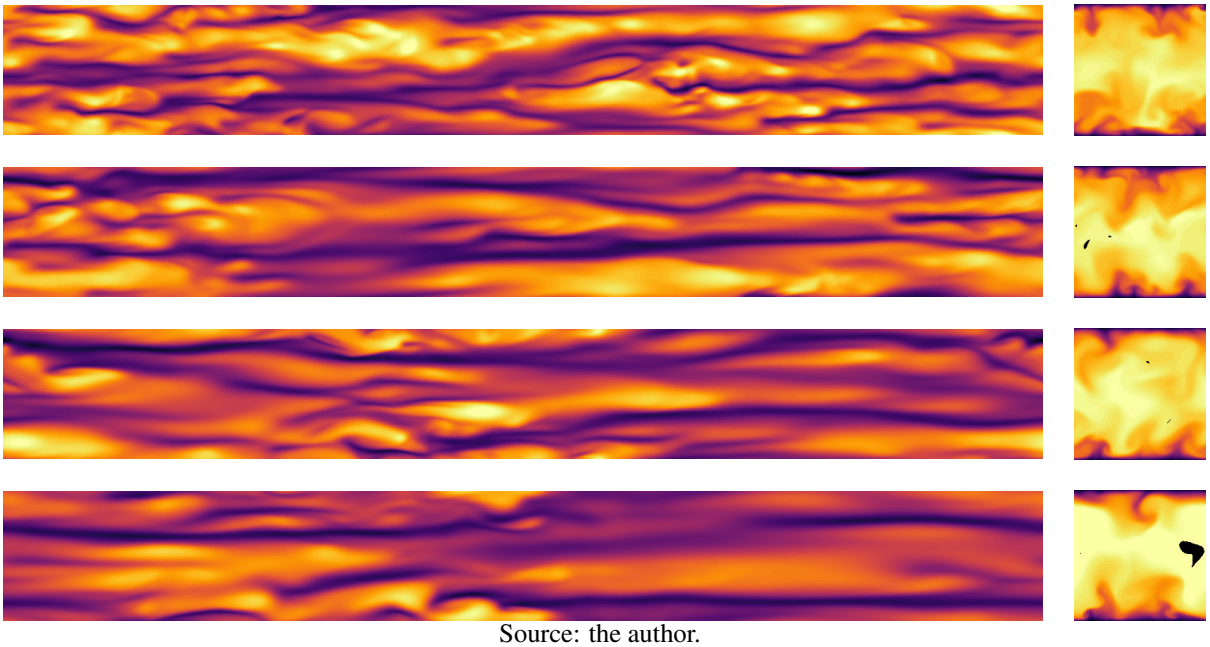

Source: the author.

Figure 5.3 – Contours of instantaneous viscosity η ranging from $1\overline{\eta}_{\mathrm{w}}$ to $5\overline{\eta}_{\mathrm{w}}$. Magnitude increases from cyan to magenta. Left: z–x plane located at the centerline. Right: x–y plane. From top to bottom: $Bn = 0$, 0.05, 0.10 and 0.15. Black spots are unyielded regions.

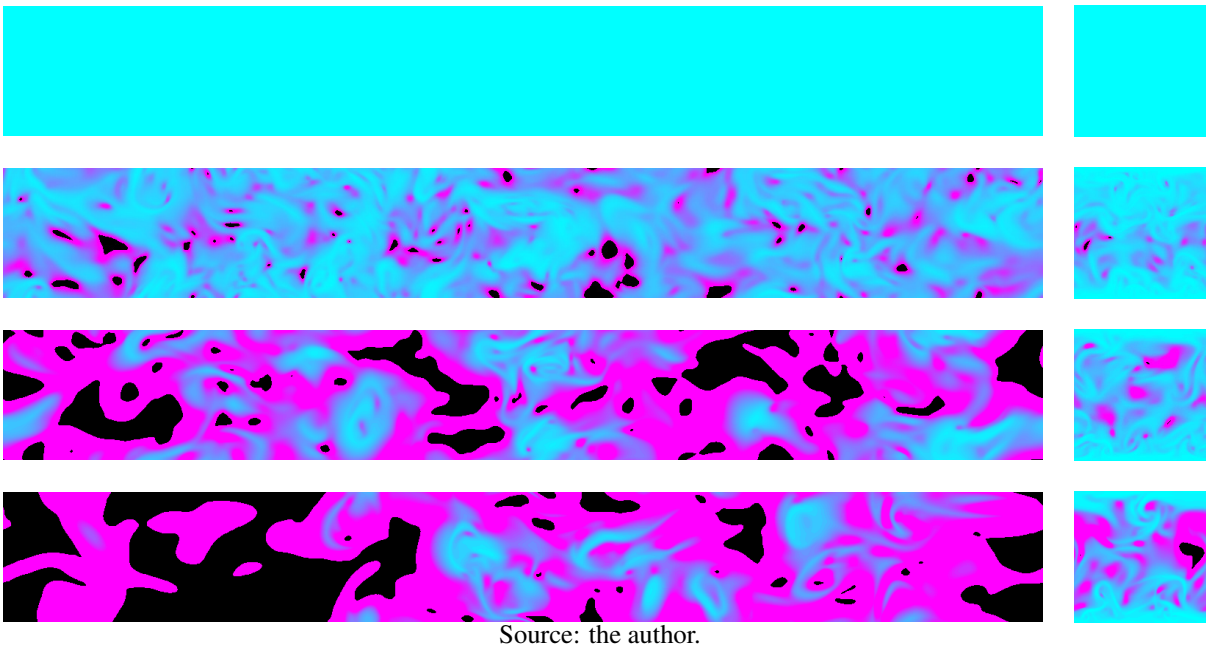

Source: the author.

The unyielded spots shown so far reveals that they are mostly disconnected and are positioned around the centerline. Three-dimensional views of the instantaneous yield surfaces are shown in Figure 5.5. The

unyielded spots are tiny and fragmented for $Bn = 0.05$. As the yield stress increases, these structures grow in size and elongate in the streamwise direction. Even though Bn varies, they seem to be confined to the same vertical extent. It has been argued in fundamental and experimental studies that the stress level in a viscoplastic turbulent flow was always higher than the yield stress, and any instantaneous appearance of a spot with $|\boldsymbol{\sigma}| < \sigma_y$ would not allow enough time for microstructural cross-link formation and true unyielding (FRIGAARD et al., 1994; GÜZEL et al., 2009). However, the present results show otherwise. The unyielded spots do not disappear quickly, but rather have a significant life-time. These structures are advected with the mean flow, change in shape and size, split or merge with others. Animations are available in a YouTube playlist at https://bit.ly/3mHrWrK.

Figure 5.4 – Contours of instantaneous vorticity ranging from $-5U_b/\delta$ to $+5U_b/\delta$. Magnitude increases from blue to red. Left: spanwise vorticity in the z–y plane. Right: streamwise vorticity in the x–y plane. From top to bottom: $Bn = 0$, 0.05, 0.10 and 0.15. Black spots are unyielded regions.

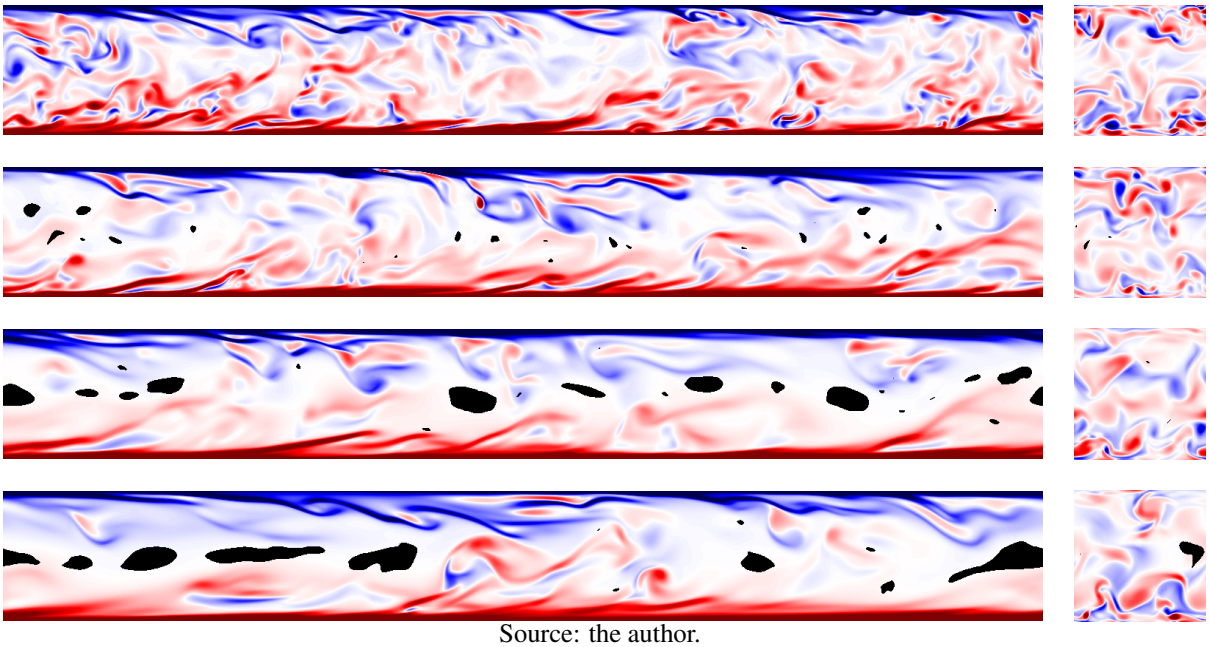

Source: the author.

Figure 5.5 – Isosurfaces of instantaneous viscosity η at the cutoff value $\eta_{\mathrm{cut-off}}$, representing the yield surfaces. The flow is from front to back of the frames. From left to right: $Bn = 0.05$, 0.10 and 0.15.

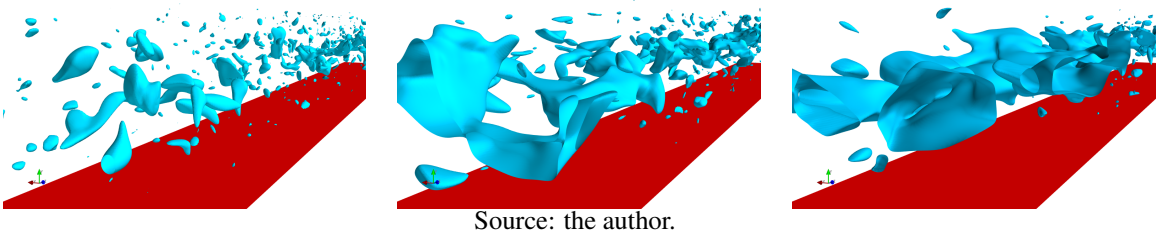

Source: the author.

5.3 Means

Some significant mean quantities obtained by DNS are summarized in Table 5.1. The actual friction Reynolds number Re^*_{actual} was calculated from the mean velocity gradient at the wall. Interestingly, the

bulk Reynolds number Re_b increased with Bn. This caused a drag reduction evidenced by the Fanning friction factor, defined as $f = \overline{\sigma}_\mathrm{w}/0.5\rho U_b^2 = 8(Re^*/Re_b)^2$. The same yield stress trend has been observed in other DNS studies (SINGH et al., 2017a; ROSTI et al., 2018). The mean wall viscosity $\overline{\eta}_\mathrm{w}$ increased with Bn in a higher proportion than any other quantity of interest.

An absolute wall scaling could be defined with the plastic viscosity, because it would not depend on the yield stress value. The wall units $u^\oplus = u/u^*$ and $y^\oplus = \rho u^* y/\eta_p$ are used in the mean streamwise ($\overline{u}_z^\oplus$) profiles of Figure 5.6a. It can be noticed that near the wall $\overline{u}_z^\oplus$ is lower for a higher Bn fluid, which was apparent from Figure 5.2. This behavior turns over at $y^\oplus \approx 25$. Curiously, the turn over location appears to be the same for all fluids. The portion where a higher Bn fluid has a higher mean streamwise velocity corresponds to 86% of the cross section area. This explains the considerable increase in bulk Reynolds number.

Table 5.1 – Summary of mean quantities of interest obtained by DNS.

Bn	Re^*_actual	Re_b	$f \times 10^3$	U_c/u^*	$\overline{\eta}_\mathrm{w}/\eta_p$
0	178	5628	8.010	18.452	1.000
0.05	179	5752	7.764	18.858	1.059
0.10	179	5862	7.510	19.241	1.124
0.15	180	6068	7.038	20.064	1.198

Source: the author.

A more appropriate wall scaling would use the actual wall viscosity. In Figure 5.6b, the wall units $u^+ = u/u^*$ and $y^+ = \rho u^* y/\overline{\eta}_\mathrm{w}$ are used in the mean streamwise ($\overline{u}_z^+$) profiles. The law-of-the-wall $u^+ = y^+$ is nicely recovered. Comparing with the absolute wall scaling of Figure 5.6a, the curves in Figure 5.6b have been shifted to the left. Even though a sense of actual location is impaired, the new scaling makes more justice to the concept of wall scaling. The viscous sublayer ($y^+ \leq 5$) is better distinguished, as well as the beginning of a log-law region ($y^+ > 30$). As a drawback, this scaling does not make a good delimiter for the core region, since the various Bn curves depart from the log-law at different y^+.

Figure 5.6 – Profiles of mean streamwise velocity. The KMM curve is the DNS result of Kim et al. (1987). The dotted lines correspond to the law-of-the-wall and log-law. (a) Absolute wall units $u^\oplus$ and $y^\oplus$, in which the law-of-the-wall is $\overline{u}_z^\oplus = y^\oplus$ and log-law is $\overline{u}_z^\oplus = 2.5\log(y^\oplus) + 5.5$. (b) Actual wall units u^+ and y^+, in which the law-of-the-wall is $\overline{u}_z^+ = y^+$ and log-law is $\overline{u}_z^+ = 2.5\log(y^+) + 5.5$.

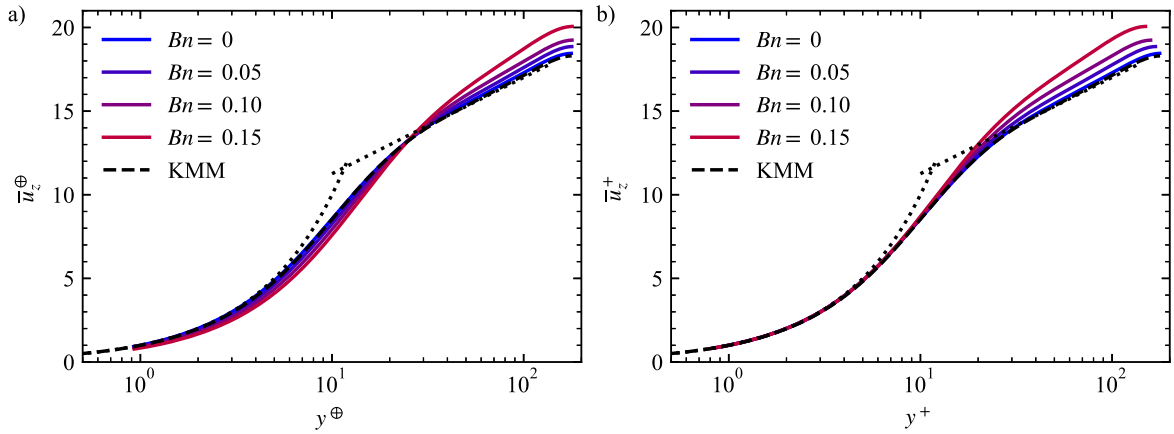

Source: the author.

The log-law region, also known as inertial sublayer, is predicted by scale arguments in a range where y is too large in wall units ($y^+ \gg 1$), but too small in integral units ($y/\delta \ll 1$). Even though it is called log-"law", the solution $\overline{u}_z^+ = A\log(y^+) + B$ is an approximation (DAVIDSON, 2015). A log-law indicator function is exhibited in Figure 5.7a. The indicator function is constant in a proper logarithmic region. It can be seen that the possible range for a log-law is too narrow, and the coefficient A has a strong Bn dependency. The existence of a power-law $\overline{u}_z^+ = B\,(y^+)^A$ in the inertial sublayer has been defended (BUSCHMANN and GAD-EL-HAK, 2003). The power-law indicator function, which is constant in a proper power region, is exhibited in Figure 5.7b. In terms of the extent of a power-law region, it seems moderately superior to the log-law, except for $Bn = 0.15$. However, the power-law coefficient is practically independent of Bn, with a value $A \approx 0.15$.

Figure 5.7 – Indicator functions for log- and power-law fitness. (a) Log-law indicator function for $\overline{u}_z^+ = A\log(y^+) + B$. (b) Power-law indicator function for $\overline{u}_z^+ = B\,(y^+)^A$.

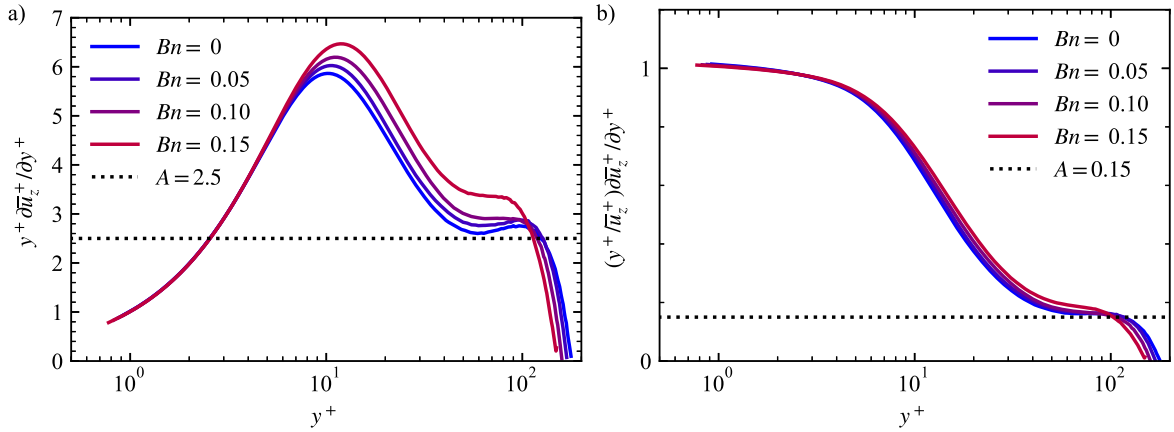

Source: the author.

Figure 5.8 – Profiles of (a) mean streamwise velocity gradient and (b) mean smoothed viscosity. Results are presented in absolute wall units in order to be distinguished in the viscous sublayer. If displayed in actual wall units, the curves would collapse in this region.

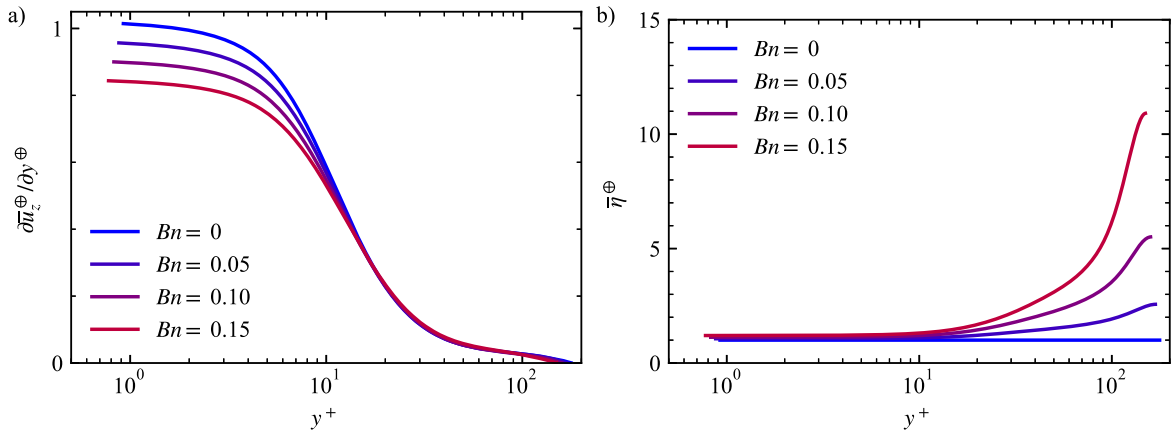

Source: the author.

Figure 5.8a shows the mean streamwise velocity gradient in absolute wall units. The yield stress has a significant effect on $\partial\overline{u}_z^\oplus/\partial y^\oplus$ inside the viscous sublayer and in the lower part of the buffer layer ($5 < y^+ < 30$). This is a compensation for the increased mean wall viscosity caused by the yield stress (see Table 5.1). Regarding the definition of mean viscosity (Eq. 2.44), the procedure for calculating it

could not use the time-average of the inverse rate-of-strain ($\overline{\dot{\gamma}}^{-1}$). This average is subject to instantaneous unyielded spots, where the instantaneous viscosity tends to infinity, so the average viscosity would become indeterminate. Instead, a smoothed mean viscosity can be calculated by ignoring those unyielded spots, i.e., not computing them whenever they appear. The result is a smooth quantity that corresponds to the real mean viscosity in the viscous and buffer layers, because no unyielded spot appearance in these locations have been registered, but which is artificially low in the core region. From this point on, the symbol $\overline{\eta}$ will be used for the smoothed mean viscosity. Figure 5.8b shows $\overline{\eta}$ profile in absolute wall units. In the upper part of the buffer layer $\overline{\eta}^{\oplus}$ starts to grow, reaching its maximum at the centerline. For reference, in a DNS of Bingham turbulent flow in a pipe with $Re^* = 323$, Singh et al. (2017a) obtained $\overline{\eta}_\mathrm{c}/\overline{\eta}_\mathrm{w} = 2.5$ for $Bn = 0.05$, $\overline{\eta}_\mathrm{c}/\overline{\eta}_\mathrm{w} = 5.5$ for $Bn = 0.10$ and $\overline{\eta}_\mathrm{c}/\overline{\eta}_\mathrm{w} \approx 15$ for $Bn = 0.20$.

The mean streamwise velocity gradient shown in Figure 5.8a reveals a wide range for $\dot{\gamma}$. In the core region $\dot{\gamma}$ can be zero. This switches a real fluid's dynamic response and provokes microstructural consequences for a thixotropic material. On the other end of the spectrum, $\partial\overline{u}_z^{\oplus}/\partial y^{\oplus} \approx 0.85$ for $Bn = 0.15$. What this means for rheometry is that a very high shear rate measurement must be made if one is to calibrate a constitutive equation for DNS. For example, considering the non-dimensional parameters of the present work, a water-based solution, and a channel gap of 20 cm, the mean shear rate at the wall should be:

$$\dot{\gamma}_{yz,\mathrm{w}} = \left(\frac{\partial\overline{u}_z^{\oplus}}{\partial y^{\oplus}}\right)\frac{\rho(u^*)^2}{\overline{\eta}_\mathrm{w}} = 0.85\rho\eta_p\left(\frac{\eta_p}{\overline{\eta}_\mathrm{w}}\right)\left(\frac{Re^*}{\delta}\right)^2 = 3.25\times10^6\ \mathrm{s}^{-1} \tag{5.5}$$

The unyielding probability was calculated as the fraction of time a certain y-location was unyielded, considering the entire channel volume. The profiles are shown in Figure 5.9. The unyielded spots emerge in locations with high viscosity, and are most frequent in the core region. Nonetheless, a non-zero unyielding probability was calculated in the upper part of the inertial subrange. In the specialized literature, there is controversy on whether unyielded spots exist in viscoplastic turbulent flow. For instance, in the DNS study of Singh et al. (2017a) no such feature was identified, while in the work of Rosti et al. (2018) there was plenty. It must be pointed out that the present work is the only one employing the exact Bingham model. The unyielded spots found by the present work are abundant, but they are definitely more moderate than in Rosti et al. (2018). For reference, Rosti et al. (2018) obtained at the centerline 13% for $Bn = 0.025$, 59% for $Bn = 0.064$ and 91% for $Bn = 0.135$.

Figure 5.9 – Unyielding probability as an ensemble average. (a) In wall scale. (b) In integral scale.

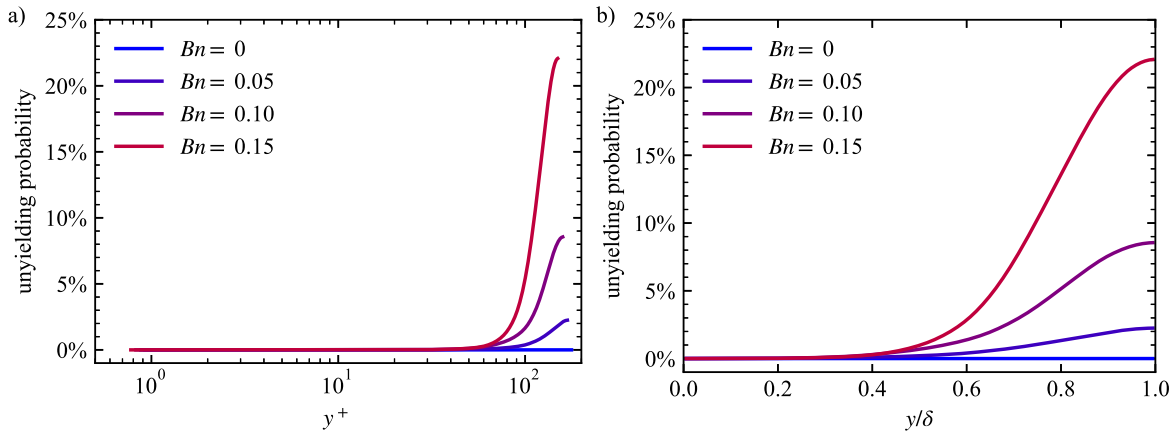

Source: the author.

5.3.1 Friction Factor

The decrease in the friction factor f revealed in Table 5.1 is a minor drag reduction. The most popular form of non-Newtonian drag reduction is the one caused by dilute polymer solutions. In such cases, the turbulent drag reduction relative to the solvent can be as high as 70% (LI et al., 2006; OWOLABI et al., 2017). In the present work, the fluid has no elasticity, and the drag reduction was caused by yield stress alone. For $Bn = 0.15$ the drag reduction was approximately 12% relative to $Bn = 0$ (solvent). Hence, the choice to call it a "minor" drag reduction.

An experimental study equivalent to the present DNS would require isolating the yield stress effect. This is practically impossible because real fluids combine many other rheological characteristics, such as elasticity and thixotropy. Therefore, the friction factor obtained by the present work is compared with another DNS in Figure 5.10. The present results have a good agreement with the DNS of Rosti et al. (2018), which was expected since they implemented an elastoviscoplastic fluid with low elasticity. For Newtonian fluid the relative difference with the experimental correlation of Dean (1978) was 4.9%. The theoretical correlation of Anbarlooei et al. (2018) is also shown for comparison. It is common in many theories of high-Re viscoplastic turbulent flow to suppose the various Bn will approach the Newtonian curve asymptotically. If this asymptotic approximation does happen, the Bn curves will approach the Newtonian curve from below, unlike the correlation shows. In this sense, Wilson and Thomas (1985) correlation (Fig. 1.4) seems more truthful.

Figure 5.10 – Friction factor f as a function of bulk Reynolds number Re_b. The filled circles are from the present work. Empty circles are from Rosti et al. (2018). The empty square is from the experimental correlation of Dean (1978) taken at $Re_b = 5636$. The lines are from the theoretical correlation of Anbarlooei et al. (2018).

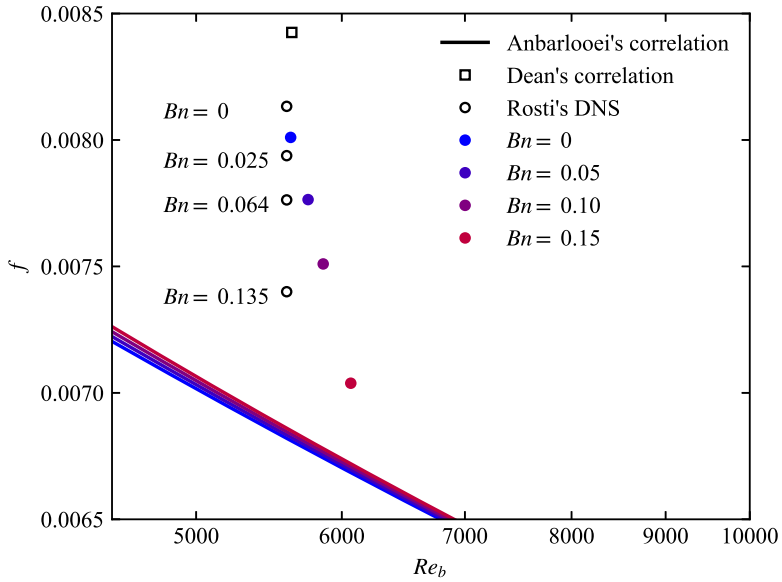

Source: the author.

5.4 Second-Order Statistics

A deeper understanding of the turbulent flow can be achieved with statistical correlations. The velocity correlation function is defined as (DAVIDSON, 2015)

$$R_{ii}\left(\boldsymbol{r}\right) = \overline{u_i'\left(\boldsymbol{x}\right) u_i'\left(\boldsymbol{x}+\boldsymbol{r}\right)} \tag{5.6}$$

where $\boldsymbol{r}$ is a position vector. R_{ii} represents how much a velocity component u_i is auto-correlated within a distance r in a given direction. Figure 5.11 shows velocity correlations taken in the spanwise direction. By standard, velocity correlation functions are normalized by $R_{ii}(0)$. Only half the spanwise length is depicted, because R_{ii} is symmetrical. When the velocity components are completely uncorrelated within the domain confines, it is considered that the computational boundaries do not have a significant influence on the large eddy dynamics. This seems to be the case for the spanwise and normal velocity components in Figure 5.11, because the correlations dropped to near zero. Judging from their values at $r_x/\delta = 1$, the streamwise velocity correlations are not so satisfactory. The general Bn effect is to extend the correlations' reach.

Figure 5.11 – Normalized spanwise velocity correlations in selected normal positions. From left to right: viscous sublayer, buffer layer and inertial sublayer. The dashed black lines are DNS results by Kim et al. (1987), shown here for reference. (a) R_{xx}. (b) R_{yy}. (c) R_{zz}.

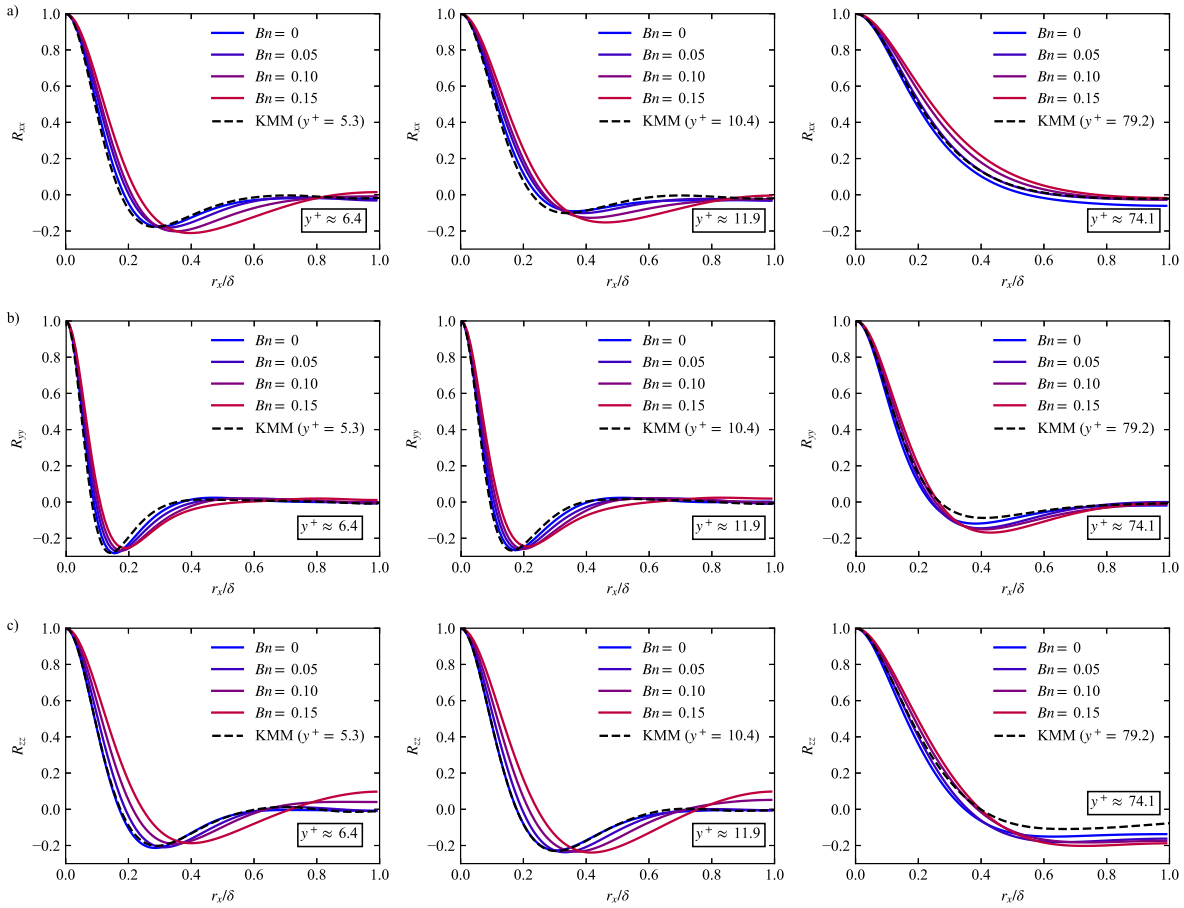

Source: the author.

Figure 5.12 shows the velocity correlations taken in the streamwise direction. Spanwise and normal velocity components are practically uncorrelated at $r_z = 3$, in any y location. However, the streamwise

velocity component is correlated for much further. This is a consequence of more elongated flow structures, such as the low speed and vortical streaks observed in Figures 5.2 and 5.4, respectively. The case $Bn = 0.15$ was the most difficult to reach $R_{zz} = 0$. Even though a wider and longer channel would be desirable to mitigate boundary effects as much as possible, it is unlikely that the flow structures and long-time averages presented here would be significantly changed. Overall, the velocity correlations of the present work agree well with the DNS of Kim et al. (1987), who used a spanwise length of $2\pi\delta$.

Figure 5.12 – Normalized streamwise velocity correlations in selected normal positions. From left to right: viscous sublayer, buffer layer and inertial sublayer. The dashed black lines are DNS results by Kim et al. (1987), shown here for reference. (a) R_{xx}. (b) R_{yy}. (c) R_{zz}.

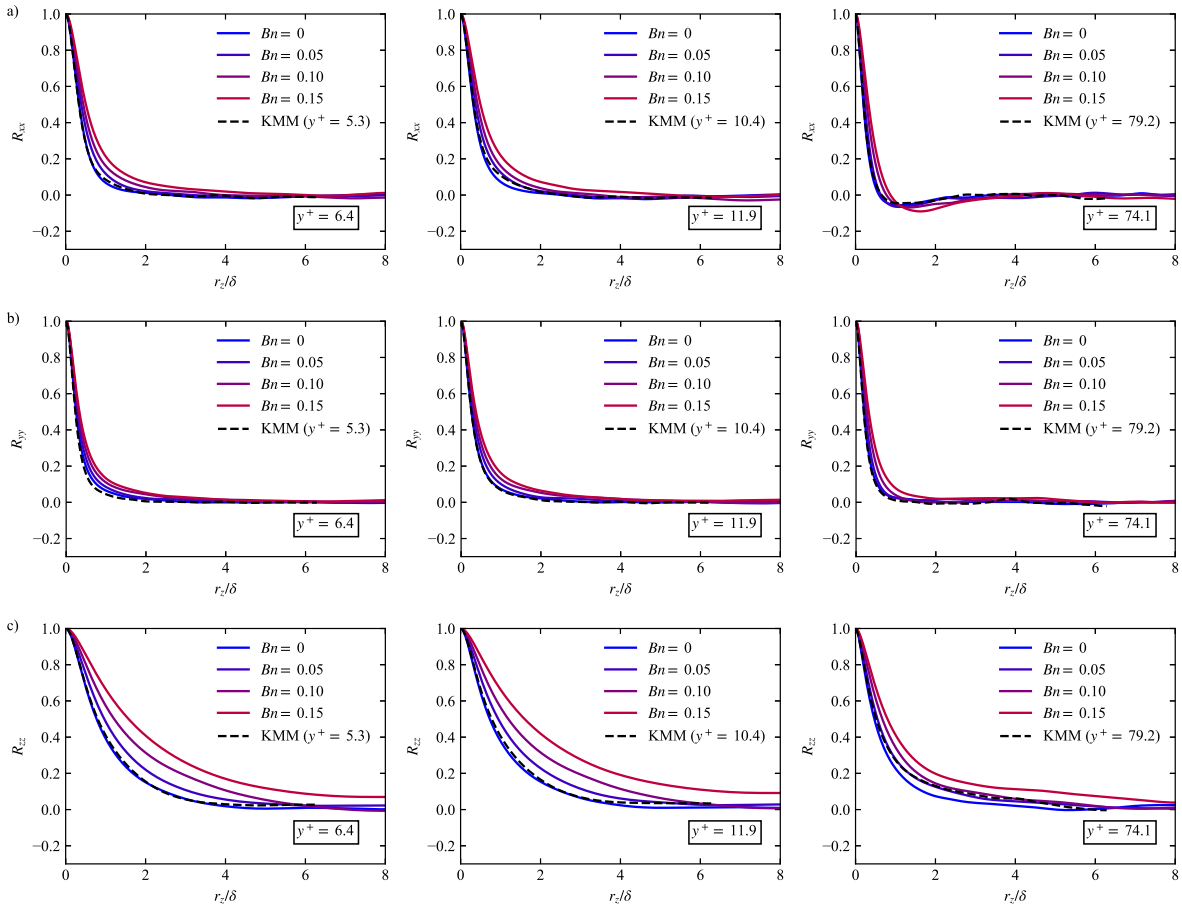

Source: the author.

A measure of the length scale of the turbulent structures can be obtained by

$$\boldsymbol{L} = \int_0^\infty \frac{R_{ii}(\boldsymbol{r})}{R_{ii}(0)}\, d\boldsymbol{r} \tag{5.7}$$

The integral length scales calculated from the velocity correlations presented above are exhibited in Figure 5.13. In the spanwise direction, the correlations drop to zero in a short distance, so L_x is quite small. On the other hand, the streamwise length scale is large. Notice that in the viscous sublayer and buffer layer L_z achieves its highest values. It is also essential to observe that L_z was increased from 1δ to 2.5δ with increasing the yield stress.

Figure 5.13 – Integral length scale calculated from (a) spanwise and (b) streamwise velocity correlations. In both cases Equation 5.7 was calculated with u_z correlation.

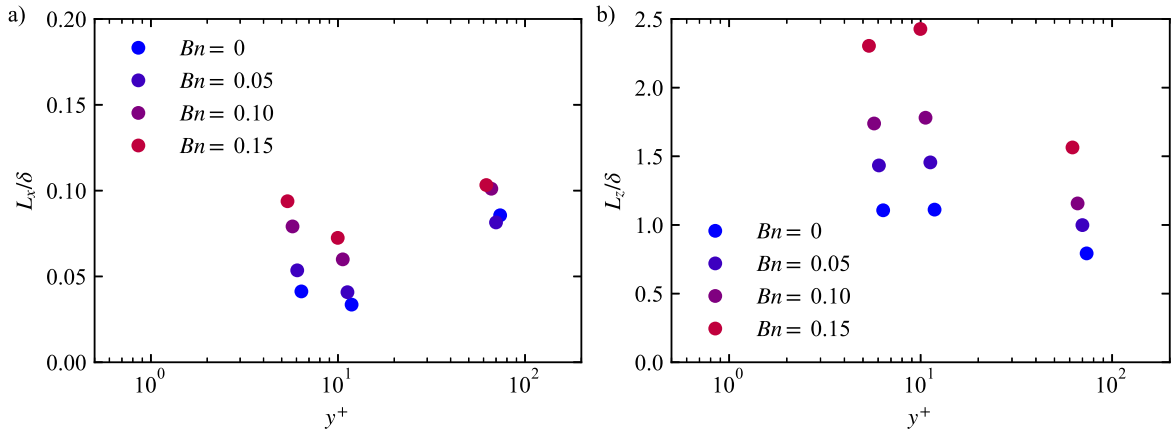

Source: the author.

Figure 5.14 – Profile of stress components in wall units. The black lines are DNS results by Kim et al. (1987). (a) Normal stresses. The dashed lines are normal Reynolds stress, the dotted lines are pressure, and the solid lines are the sum of both components. (b) Shear stresses. The dashed lines are Reynolds stress, the dash-dot lines are the mean viscous stress and the dotted lines are turbulent viscous stress.

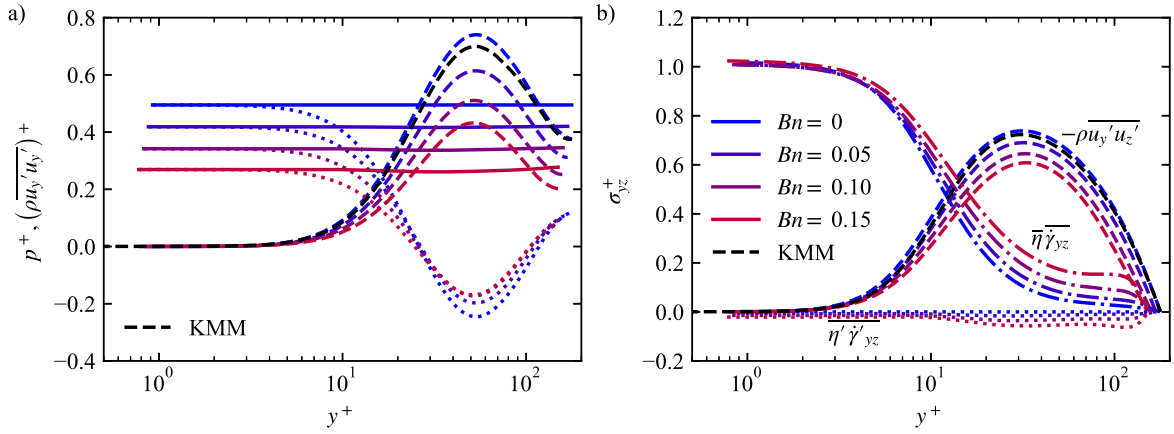

Source: the author.

The mean flow equations have been presented in Section 2.5.1.1. From Equation 2.43, the momentum balance equation in the normal direction is

$$0 = \partial_y \left(p - \rho\overline{u_y' u_y'}\right) \tag{5.8}$$

The viscous stress component $\overline{\sigma}_{yy}$ has been verified to be negligible with respect to the terms above. Equation 5.8 implies that the sum of pressure and the yy component of the Reynolds stress must be a constant. Figure 5.14a present a verification of the mean normal stress balance. The pressure is high in the viscous sublayer, while the normal Reynolds stress is zero. However, in the inertial sublayer the normal Reynolds stress is dominant.

In the z coordinate, Equation 2.43 becomes

$$0 = \partial_y \left(\overline{\bar{\eta}\dot{\gamma}}_{yz} + \overline{\eta'\dot{\gamma}'_{yz}} - \rho\overline{u_y' u_z'}\right) + F_z \tag{5.9}$$

The terms inside the divergent are, in order of appearance, mean viscous stress, turbulent viscous stress and Reynolds stress. The mean shear stress profile is shown in Figure 5.14b. According to Equation

5.9, the sum of shear stress terms must be a linear function of y. This sum is not shown in the figure for clarity. The mean viscous stress is dominant in the viscous sublayer, while the Reynolds stress dominates in the inertial sublayer and above it. However, the dominance of the Reynolds shear stress is not so great when Bn is elevated. At $y^+ = 32$, where $-\rho\overline{u'_y u'_z}$ peaks, the Reynolds shear stress of $Bn = 0.15$ is 140% higher than the mean viscous stress, while for the Newtonian fluid this superiority is 650%. The turbulent viscous stress is very low near the wall, but it can be significant in the core region if the yield stress is high. At $y^+ = 120$, its ratio to the total mean shear stress is 4% for $Bn = 0.05$, 12% for $Bn = 0.10$ and 28% for $Bn = 0.15$. This has implications for turbulence modeling of viscoplastic fluids. At a first look, neglecting $\overline{\eta'\dot{\gamma}'_{yz}}$ will not jeopardize the near-wall dynamics. On the other hand, many important flow features take place in the core region.

Figure 5.15 – Root mean squares of turbulent fluctuations in wall units. The dashed black lines are DNS results by Kim et al. (1987). (a) Spanwise velocity. (b) Normal velocity. (c) Streamwise velocity. (d) Smoothed viscosity.

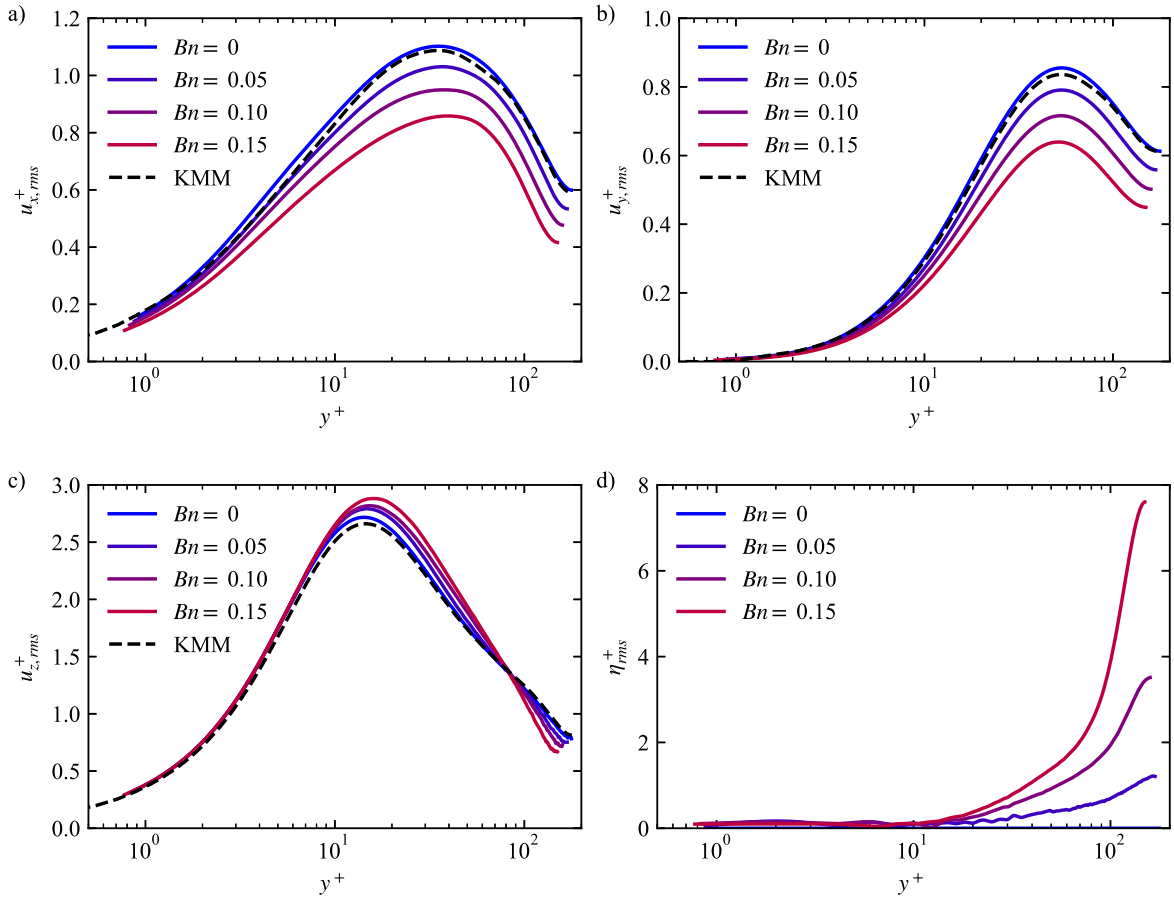

Source: the author.

A measure of the statistical dispersion of turbulent variables is obtained by the root mean square (rms):

$$u_{i,rms} = \sqrt{\overline{u'_i u'_i}} \tag{5.10}$$

The rms quantities are commonly refereed to as turbulent intensities. Figure 5.15 shows root mean squares of the velocity components and viscosity. The maximum locations are not significantly changed with Bn, but their values are. The spanwise and normal turbulent intensities are decreased with Bn,

while the streawise intensity is increased. Thus, the yield stress has an effect of increasing turbulence anisotropy. The variations of the turbulent intensities with Bn are relevant from the buffer layer and above. In the core region, all rms velocity components are decreased with Bn. The smoothed viscosity's rms are shown in Figure 5.15d. The viscosity fluctuations start to be important from $y^+ = 10$. It indicates that the viscosity remains exceptionally stable inside the viscous sublayer, even though there is considerable velocity fluctuation.

5.4.1 Budgets of Turbulent Kinetic Energy

The turbulent kinetic energy is defined by $k = \left(\overline{u'_x u'_x} + \overline{u'_y u'_y} + \overline{u'_z u'_z}\right)/2$. Interpreting its budgets is an effective way to understand turbulent flows. By subtracting the mean flow momentum balance equation (Eq. 2.43) from its instantaneous counterpart (Eq. 2.42), one gets an equation for the fluctuating parcel u'_α:

$$\rho\partial_t u'_\alpha + \rho\overline{u}_\beta\partial_\beta u'_\alpha + \rho u'_\beta\partial_\beta\overline{u}_\alpha + \rho u'_\beta\partial_\beta u'_\alpha = -\partial_\alpha p' + \partial_\beta\sigma'_{\alpha\beta} + \rho\partial_\beta\left(\overline{u'_\alpha u'_\beta}\right) \tag{5.11}$$

where the mean and turbulent viscous stress components were replaced by the total viscous stress $\boldsymbol{\sigma}$, for convenience. Equation 5.11 can be used to write expressions for u'_α and u'_β. By summing both expressions and then making $\alpha = \beta$, the following turbulent kinetic energy equation is obtained

$$\rho\overline{u}_\beta\partial_\beta k = \partial_\beta\left(-\frac{1}{2}\rho\overline{u'_\alpha u'_\alpha u'_\beta} - \overline{u'_\beta p'} + \overline{u'_\alpha\sigma'_{\alpha\beta}}\right) + \frac{1}{2}\sigma^R_{\alpha\beta}\bar{\dot{\gamma}}_{\alpha\beta} - \frac{1}{2}\overline{\sigma'_{\alpha\beta}\dot{\gamma}'_{\alpha\beta}} \tag{5.12}$$

where $\sigma^R_{\alpha\beta} = -\rho\overline{u'_\alpha u'_\beta}$ is the Reynolds stress. On the account of homogeneity and null mean normal velocity, the term on the left-hand side is zero. The first term on the right-hand side represents diffusive *transport* (T). The second term, *generation* (G), transfers energy from the mean flow to the turbulence (DAVIDSON, 2015). The last one is dissipation (ε), which removes energy from the turbulence and turns it into internal energy.

The k profile is shown in Figure 5.16a and its budgets are seen in Figure 5.16b. The turbulent kinetic energy is unaltered by the yield stress in the viscous sublayer, because dissipation is balanced out by transport. In the buffer layer the viscoplastic fluid has more turbulent kinetic energy than the Newtonian. At $y^+ = 45$ there is a switch. The viscoplastic fluid has progressively less k than the Newtonian, as y increases. The reason for it is that the dissipation profile also switched. In the lower part of the inertial sublayer the viscoplastic fluid's dissipation becomes slightly higher than the Newtonian's, and the region above it corresponds to the vast majority of the channel cross section area. Hence, in the core region the viscoplastic fluid flow is significantly less turbulent than the Newtonian. It may seem counter intuitive that, even though the viscosity of a yield stress fluid is higher in the viscous sublayer, the turbulence dissipation is lower. The reason is likely to be the less intense mean shear rate $\partial\overline{u}_z/\partial y$ in the region (Fig. 5.8a).

The location where the mean streamwise velocity of the viscoplastic fluid begins to surpass the Newtonian coincides with the peak generation at $y^+ \approx 10$. The term G takes kinetic energy away from the mean flow, and converts it to turbulent fluctuations. The lower k-generation of a yield stress fluid is a plausible explanation for the higher bulk velocity. Even though the yield stress causes an increased turbulent activity in the buffer layer, the anisotropy of the velocity fluctuations has a net effect

of decreasing the main contribution term $-\rho\overline{u'_y u'_z}$ (see Fig. 5.14b). In the buffer layer, the generation takes place in a relatively short area, but with much higher intensity than in the core region.

It is interesting to make *a posteriori* analysis of the numerical resolution. It has been considered that the dissipation in the viscous sublayer was $\varepsilon^+ = 0.2$. Indeed, this is very close to the value obtained in the present work. The low dissipation of the viscoplastic fluid indicates that a grid designed with a proper resolution for a Newtonian fluid is naturally adequate for a Bingham fluid with $\eta_p = \mu$.

Figure 5.16 – Turbulent kinetic energy profile (a) and budgets (b). The solid lines are dissipation, the dashed lines are generation and the dotted lines are transport components.

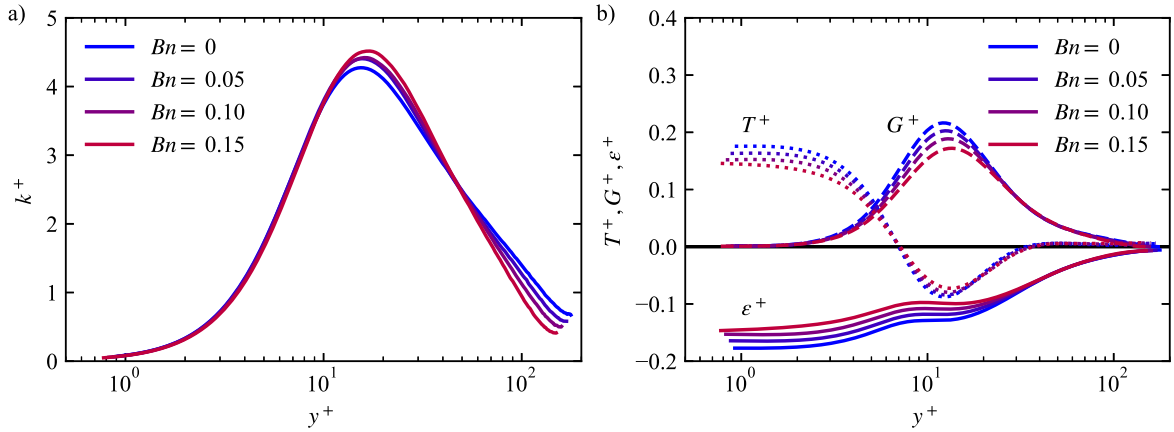

Source: the author.

5.5 Chapter Summary

In this Chapter, the viscoplastic LB scheme developed in the present work has been applied in a case study of viscoplastic turbulent flow. A turbulent channel flow with a Bingham fluid has been solved by direct numerical simulations. The friction Reynolds number was fixed at 180, while the Bingham number varied from 0 to 0.15. The non-dimensional parameter choice was such that the driving force and the plastic viscosity were the same in all cases investigated. Surprisingly, increasing the yield stress caused an increase in the bulk velocity, resulting in a minor drag reduction. It was shown that unyielded spots are present in the upper inertial sublayer and core region of the flow. Contrary to some widespread ideas, these unyielded spots do not disappear quickly, i.e., they move along with the mean flow and interact with each other for a significant amount of time.

Another yield stress effect in this turbulent flow is to increase anisotropy of the velocity fluctuations. A net outcome of that is a considerable decrease in the Reynolds shear stress. In the buffer layer, where the most intense turbulent activity happens, the low Reynolds shear stress keeps the mean kinetic energy elevated. In the present author's opinion, this is a plausible explanation for the increased bulk velocity of the viscoplastic fluid. This effect has nothing to do with the unyielded spots, because they only appear in locations further away from the wall.

As a final note, it is worth to remember that the continuum fluid mechanics is valid only when the Kolmogorov scale $l^{\oplus} \sim (\varepsilon^{\oplus})^{-1/4}$ is at least an order of magnitude larger than the microstructural particles that compose a real viscoplastic solution. Considering the non-dimensional parameters of the present work, a water-based solution and a channel gap of 20 cm, the Kolmogorov scale is $l \sim 850$ μm.

This is much larger than bentonite or Carbopol particles (BAUDONNET et al., 2004; MESBOUA et al., 2018), which compose some model fluids. Nevertheless, a continuum validity check must be carried out when comparing DNS and experimental results.

6 FINAL REMARKS

This thesis document was opened with a literature review of viscoplastic turbulent flows. This topic has been subject of studies for decades. Yet, technical difficulties amount and there are still many open questions and debates. The development of a direct numerical simulation (DNS) tool was defined as the main objective, with the hope it could provide meaningful physical insights. The lattice Boltzmann method (LBM) was adopted due to its remarkable efficiency in parallel computation. However, the existing numerical schemes in LBM for viscoplastic fluid flows had many limitations. Before diving into viscoplastic turbulent flow, it was necessary to develop a particular scheme for the numerical treatment of yield stress fluids.

The viscoplastic LB scheme had a very simple proposition. In LBM, the relaxation frequency has an inverse proportionality with the viscosity, and setting it to zero would not lead to any indetermination. Some of the most popular viscoplastic models, such as the Bingham constitutive equation, have a singularity ($\eta \to \infty$) in the unyielded portion of material. Thus, setting a null relaxation frequency in these portions would represent the exact viscoplastic model without resorting to a viscosity regularization. The method was made numerically stable with the regularization of ghost moments. Successful simulations were carried out with a wide range of relaxation frequencies.

Validation was pursued by solving some benchmark viscoplastic laminar flows. In the steady-state parallel plates Poiseuille problem, the error decay was observed to follow the second-order with the spatial grid refinement. Overall, the steady-state laminar cases resulted in excellent agreements with conventional numerical methods, such as finite volume and augmented Lagrangian methods. Usually, the coupling between rate-of-strain and stress for a Bingham fluid has to be solved with inner-iterations, because they have an implicit relationship. Fortunately, an exact solution for this relationship was found for the Bingham fluid, due to the nature of how the stress tensor is evaluated in LBM. This feature improved the simulations' stability and accuracy even further. Startup and stopping viscoplastic flows were solved to provide an assessment of the transient behavior. These case studies resulted in excellent agreement with theoretical solutions available.

Finally, a case of viscoplastic turbulent flow was solved with direct numerical simulations. The classical turbulent channel flow was chosen for this task. The viscoplastic LB scheme behave well under the challenging circumstances of this type of problem. Some expected results were confirmed, such as the minor drag reduction and the increased turbulence anisotropy caused by the yield stress. Some other results tip the balance towards an idea that has been less in vogue, namely, the presence of unyielded spots in the turbulent flow is possible. As an indication of that, unyielded spots were observed in the core region of the flow in vast quantities and with significant life-times. Moreover, the yield stress had a significant impact in the turbulent intensities, meaning that conventional Reynolds-averaged Navier-Stokes (RANS) models have to be modified for this type of material. The numerical data revealed interesting implications for rheometry and experimentation with viscoplastic turbulent flows. The mean wall shear rate exceeds the range of common rheometers and viscometers. The Kolmogorov scale, which represents the smallest turbulent eddies, was estimated for a prototypical flow. Clearly, for Reynolds numbers higher than the one used in the present work, the microstructural particle size of real suspensions will be of the same

order of the Kolmogorov scale, and the continuum approach will fail.

6.1 Pondering on Goals and Challenges

During the final sprint of this work the world was hit by the COVID-19 pandemic. Unfortunately, this crisis had a direct impact on one of this thesis' original goals. Viscoplastic turbulent flow in a pipe was also intended to be solved by DNS. A GPU server was purchased in December 2019. It was supposed to have arrived in April 2020. However, a series of factors made this impossible. The way around it was to rent a cloud computing service for the direct numerical simulations, so it was done for the turbulent channel flow case. The feeling of the present author and his advisors is that the channel flow case was successful in the mission of substantiating this thesis and demonstrating the qualities of the proposed numerical scheme.

During the project elaboration, a third goal was desired. At the time it seemed possible to work on the development of closure models for the turbulent viscous stress in large eddy simulations, besides the already mentioned goals. Indeed, as pointed out by one of the examiners, the amount of time needed for this was underestimated, so it was left out. This decision was made even before the pandemic. Cutting it out seemed to have made the thesis pursuit even stronger, because there was more time available to dedicate on careful implementation and physical assessments (validation).

6.2 Future Work

In this section, some suggestions for future work are given. The DNS of turbulent viscoplastic flow in a pipe is strongly recommended for future investigations, because there is greater availability of experimental data. Even so, the formulation of model viscoplastic fluids and the visualization of unyielded spots will continue to be challenging tasks in the experimental area in the next years. It would be important to solve viscoplastic turbulent flows at higher Reynolds number to see if the yield stress effects are suppressed. There are many other ways to take advantage of direct numerical simulations that, due to time restrictions, were not done in the present work. Higher-order statistics, such as skewness and flatness factors, could quantify asymmetry and intermittency, respectively. Moreover, the methodology presented in this thesis would be an excellent tool for a deeper investigation of coherent structures and how they are changed by yield stress.

The availability of DNS data of viscoplastic turbulent flows might prompt the development of turbulence models for Reynolds-averaged Navier-Stokes (RANS) and large eddy simulations (LES). One of the things to deal with is the turbulent viscous stress. In the present work, it was shown that this stress has a negligible magnitude in the viscous and buffer layers, although it might be relevant in the core region. It seems that the real challenge is related to the turbulence anisotropy caused by the viscoplastic fluid, and the related decrease in the turbulent kinetic energy in the core region. In RANS, the turbulence is considered isotropic, so a workaround might be damping the Reynolds stresses. In LES, turbulence is considered isotropic only in the dissipative scales. However, a LES grid is typically truncated in a length scale lying in the inertial sublayer. So, the challenge is to develop a sub-grid stress that correctly produces the excess generation of turbulent kinetic energy caused by the viscoplastic fluid.

It has been discussed throughout this work that the LBM grid uniformity was the most limiting aspect of the method. The same statistical outcome presented in Chapter 5 could have been obtained with ten times fewer grid nodes if a non-uniform grid was employed. The consequences would be tremendous. A typical turbulent channel flow simulation could be solved in 90 minutes with a NVIDIA Tesla V100 (flow development plus fully developed phases). With a NVIDIA Tesla K20x, which is approximately ten times cheaper, this case would take around 6 hours. The rectangular lattice that can make this possible is illustrated in Figure 6.1. It looks as if a cubic lattice was stretched in one direction, and then, in another direction. In the present author's opinion, an aspect ratio of 5 would make this feature very appealing and a game changer for computational fluid dynamics. Logically, this idealized rectangular lattice should be free from numerical issues such as artificial dissipation and instability.

Figure 6.1 – Illustration of a rectangular lattice.

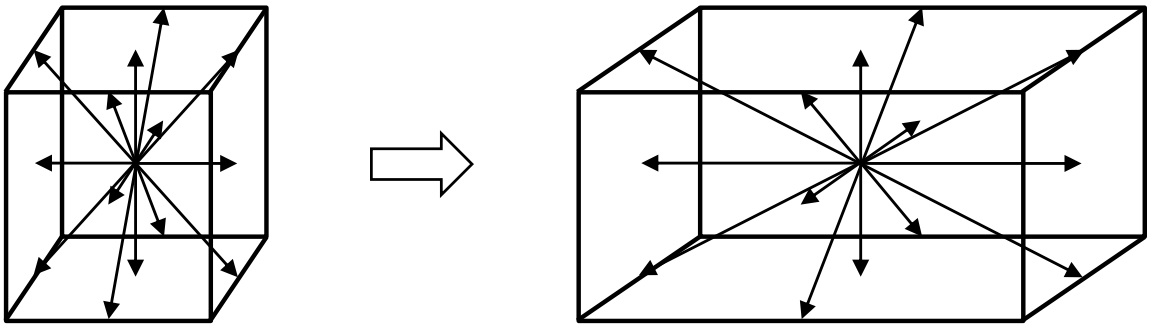

Source: the author.

6.3 Publications, Patents and Derivations

During the course of this thesis, journal articles, conference papers and software copyright have been produced. The steady-state laminar results from Section 4.1 were published in the *Journal of Non-Newtonian Fluid Mechanics* (LUGARINI et al., 2020). The present author had the opportunity to speak in relevant international conferences, such as the *VPF8 Viscoplastic Fluids: from Theory to Application* (VPF8 2019, Cambridge, UK) and the *18th International Congress on Rheology* (ICR 2020, Rio de Janeiro). Encouraging feedback has been received from the scientific community.

The contents of this work have been applied in other research projects being executed in the Research Center for Rheology and Non-Newtonian Fluids of the Federal University of Technology – Paraná. The regularization of ghost moments for the forcing LBM was used in a paper on particle settling, which is currently under review in the *Computers & Fluids* journal. Two other papers using the viscoplastic LB scheme in particle settling investigations are being prepared for submission. The exact solution for the stress/rate-of-strain coupling and the DNS results for the viscoplastic turbulent channel flow are also being prepared for submission.

A software copyright was obtained by the working group responsible for the GPU implementation, of which the present author was part of. It was registered in the Brazilian Institute of Intellectual Property under the number BR512020000669-8. A new version of this software is under way for particle-laden turbulent flows.

BIBLIOGRAPHY

ANBARLOOEI, H.; CRUZ, D.; RAMOS, F.; SANTOS, C.; Silva Freire, A. On the connection between Kolmogorov microscales and friction in pipe flows of viscoplastic fluids. *Physica D: Nonlinear Phenomena*, North-Holland, v. 376-377, p. 69–77, 2018.

ANBARLOOEI, H. R.; CRUZ, D. O. A.; RAMOS, F.; SANTOS, C. M. M.; Silva Freire, A. P. Phenomenological friction equation for turbulent flow of Bingham fluids. *Physical Review E*, v. 96, n. 2, p. 023107, 2017.

Anderson JR, J. D. *Fundamentals of aerodynamics*. Tata McGraw-Hill Education, 2010.

API. *Rheology and Hydraulics of Oil-well Fluids - API Recommended Practice 13D*. 2010. 1–94 p.

BAHRANI, S. A.; NOUAR, C. Intermittency in the transition to turbulence for a shear-thinning fluid in Hagen-Poiseuille flow. *Journal of Applied Fluid Mechanics*, v. 7, n. 01, p. 1–6, 2014.

BALMFORTH, N. J.; FRIGAARD, I. A.; OVARLEZ, G. Yielding to stress: Recent developments in viscoplastic fluid mechanics. *Annual Review of Fluid Mechanics*, v. 46, n. 1, p. 121–146, 2014.

BARNES, H. A.; WALTERS, K. The yield stress myth? *Rheologica Acta*, v. 24, n. 4, p. 323–326, 1985.

BAUDONNET, L.; GROSSIORD, J.; RODRIGUEZ, F. Effect of dispersion stirring speed on the particle size distribution and rheological properties of three carbomers. *Journal of Dispersion Science and Technology*, v. 25, n. 2, p. 183–192, 2004.

BHATNAGAR, P. L.; GROSS, E. P.; KROOK, M. A model for collision processes in gases. I. Small amplitude processes in charged and neutral one-component systems. *Physical Review*, v. 94, n. 3, p. 511–525, 1954.

BINGHAM, E. C. *Fluidity and plasticity*. McGraw-Hill, 1922. 215–218 p.

BIRD, R. B.; ARMSTRONG, R. C.; HASSAGER, O. *Dynamics of polymeric liquids, Vol. 1 Fluid Mechanics*. New York, USA: John Wiley & Sons, 1987.

BIRD, R. B.; STEWART, W. E.; LIGHTFOOT, E. N. *Transport phenomena*. 2. ed. New York, USA: John Wiley & Sons, Inc., 2002. 259–260 p.

BOTELLA, O.; PEYRET, R. Benchmark spectral results on the lid-driven cavity flow. *Computers & Fluids*, Pergamon, v. 27, n. 4, p. 421–433, 1998.

BUICK, J. M.; GREATED, C. A. Gravity in a lattice Boltzmann model. *Physical Review E*, v. 61, n. 5, p. 5307–5320, 2000.

BUSCHMANN, M. H.; GAD-EL-HAK, M. Debate concerning the mean-velocity profile of a turbulent boundary layer. *AIAA Journal*, v. 41, n. 4, p. 565–572, 2003.

CALDWELL, D. H.; BABBITT, H. E. Flow of muds, sludges, and suspensions in circular pipe. *Industrial & Engineering Chemistry*, v. 33, n. 2, p. 249–256, 1941.

CHAPMAN, S.; COWLING, T. *The mathematical theory of non-uniform gases*. 3rd. ed. New York, USA: Cambridge University Press, 1970.

DARBY, R.; MELSON, J. How to predict the friction factor for flow of Bingham plastics. *Chemical Engineering*, n. 28, p. 59–61, 1987.

DAVIDSON, P. A. *Turbulence: an introduction for scientists and engineers*. New York, USA: Oxford university press, 2015.

de Souza Mendes, P. R.; NACCACHE, M. F.; VARGES, P. R.; MARCHESINI, F. H. Flow of viscoplastic liquids through axisymmetric expansions–contractions. *Journal of Non-Newtonian Fluid Mechanics*, v. 142, n. 1-3, p. 207–217, 2007.

DEAN, R. B. Reynolds number dependence of skin friction and other bulk flow variables in two-dimensional rectangular duct flow. *Journal of Fluids Engineering*, v. 100, n. 2, p. 215–223, 1978.

D'HUMIÈRES, D.; GINZBURG, I. Viscosity independent numerical errors for lattice Boltzmann models: From recurrence equations to "magic" collision numbers. *Computers & Mathematics with Applications*, v. 58, n. 5, p. 823–840, 2009.

DIMAKOPOULOS, Y.; MAKRIGIORGOS, G.; GEORGIOU, G.; TSAMOPOULOS, J. The PAL (Penalized Augmented Lagrangian) method for computing viscoplastic flows: A new fast converging scheme. *Journal of Non-Newtonian Fluid Mechanics*, Elsevier, v. 256, n. March, p. 23–41, 2018.

DODGE, D. W.; METZNER, A. B. Turbulent flow of non-Newtonian systems. *AIChE Journal*, v. 5, n. 2, p. 189–204, 1959.

DUAN, M.; MISKA, S. Z.; YU, M.; TAKACH, N. E.; AHMED, R. M.; ZETTNER, C. M. Transport of small cuttings in extended-reach drilling. *SPE Drilling & Completion*, v. 23, n. 03, p. 258–265, 2008.

EGGELS, J. G. M.; UNGER, F.; WEISS, M. H.; WESTERWEEL, J.; ADRIAN, R. J.; FRIEDRICH, R.; NIEUWSTADT, F. T. M. Fully developed turbulent pipe flow: a comparison between direct numerical simulation and experiment. *Journal of Fluid Mechanics*, v. 268, p. 175–210, 1994.

ESCUDIER, M.; POOLE, R.; PRESTI, F.; DALES, C.; NOUAR, C.; DESAUBRY, C.; GRAHAM, L.; PULLUM, L. Observations of asymmetrical flow behaviour in transitional pipe flow of yield-stress and other shear-thinning liquids. *Journal of Non-Newtonian Fluid Mechanics*, Elsevier, v. 127, n. 2-3, p. 143–155, 2005.

ESMAEL, A.; NOUAR, C. Transitional flow of a yield-stress fluid in a pipe: Evidence of a robust coherent structure. *Physical Review E*, v. 77, n. 5, p. 057302, 2008.

FRIGAARD, I.; NOUAR, C. On the usage of viscosity regularisation methods for visco-plastic fluid flow computation. *Journal of Non-Newtonian Fluid Mechanics*, v. 127, n. 1, p. 1–26, 2005.

FRIGAARD, I. a.; HOWISON, S. D.; SOBEY, I. J. On the stability of Poiseuille flow of a Bingham fluid. *Journal of Fluid Mechanics*, v. 263, n. -1, p. 133, 1994.

GEHRKE, M.; JANSSEN, C.; RUNG, T. Scrutinizing lattice Boltzmann methods for direct numerical simulations of turbulent channel flows. *Computers & Fluids*, v. 156, p. 247–263, 2017.

GHIA, U.; GHIA, K.; SHIN, C. High-Re solutions for incompressible flow using the Navier-Stokes equations and a multigrid method. *Journal of Computational Physics*, v. 48, n. 3, p. 387–411, 1982.

GINZBURG, I.; D'HUMIÈRES, D. Multireflection boundary conditions for lattice Boltzmann models. *Physical Review E - Statistical Physics, Plasmas, Fluids, and Related Interdisciplinary Topics*, v. 68, n. 6, p. 1–30, 2003.

GINZBURG, I.; STEINER, K. A free-surface lattice Boltzmann method for modelling the filling of expanding cavities by Bingham fluids. *Philosophical Transactions of the Royal Society of London. Series A: Mathematical, Physical and Engineering Sciences*, v. 360, n. 1792, p. 453–466, 2002.

GINZBURG, I.; VERHAEGHE, F.; D'HUMIÈRES, D. Study of simple hydrodynamic solutions with the two-relaxation-times lattice Boltzmann scheme. *Communications In Computational Physics*, v. 3, n. 3, p. 519–581, 2008.

GLOWINSKI, R. *Numerical methods for nonlinear variational problems*. New York, USA: Springer-Verlag, 1984.

GOMBOSI, T.; GOMBOSI, A. *Gaskinetic theory*. Cambridge: Cambridge University Press, 1994.

GOVIER, G. W.; AZIZ, K. *The flow of complex mixtures in pipes*. New York, USA: Van Nostrand Reinhold Company, 1972.

GRASINGER, M.; OVERACKER, S.; BRIGHAM, J. Numerical investigation of the accuracy, stability, and efficiency of lattice Boltzmann methods in simulating non-Newtonian flow. *Computers & Fluids*, Pergamon, v. 166, p. 253–274, 2018.

GUANG, R.; RUDMAN, M.; CHRYSS, A.; SLATTER, P.; BHATTACHARYA, S. A DNS investigation of the effect of yield stress for turbulent non-Newtonian suspension flow in open channels. *Particulate Science and Technology*, v. 29, n. 3, p. 209–228, 2011.

GUO, Z.; ZHENG, C.; SHI, B. Discrete lattice effects on the forcing term in the lattice Boltzmann method. *Physical Review E*, v. 65, n. 4, p. 046308, 2002.

GÜZEL, B.; BURGHELEA, T.; FRIGAARD, I. A.; MARTINEZ, D. M. Observation of laminar–turbulent transition of a yield stress fluid in Hagen–Poiseuille flow. *Journal of Fluid Mechanics*, Cambridge University Press, v. 627, p. 97, 2009.

HALLBOM, D. *Pipe flow of homogeneous slurry*. 260 p. Thesis (PhD) — The University of British Columbia, 2008.

HALLBOM, D.; KLEIN, B. A physical model for yield plastic fluids. *Particulate Science and Technology*, v. 27, n. 1, p. 1–15, 2009.

HANKS, R. W. The laminar-turbulent transition for fluids with a yield stress. *AIChE Journal*, v. 9, n. 3, p. 306–309, 1963.

HANKS, R. W. On the flow of Bingham plastic slurries in pipes and between parallel plates. *Society of Petroleum Engineers Journal*, v. 7, n. 04, p. 342–346, 1967.

HANKS, R. W. Low Reynolds number turbulent pipeline flow of pseudohomogeneous slurries. In: *Fifth International Conference on the Hydraulic Transport of Solids in Pipes (Hydrotransport 5)*. Hannover, Germany: BHRA Fluid Engineering, 1978. p. 23–34.

HANKS, R. W.; DADIA, B. H. Theoretical analysis of the turbulent flow of non Newtonian slurries in pipes. *AIChE Journal*, v. 17, n. 3, p. 554–557, 1971.

HANKS, R. W.; RICKS, B. L. Transitional and turbulent pipeflow of pseudoplastic fluids. *Journal of Hydronautics*, v. 9, n. 1, p. 39–44, 1975.

HE, X.; CHEN, S.; DOOLEN, G. D. A novel thermal model for the lattice Boltzmann method in incompressible limit. *Journal of Computational Physics*, v. 146, n. 1, p. 282–300, 1998.

HE, X.; LUO, L.-S.; DEMBO, M. Some Progress in Lattice Boltzmann Method. Part I. Nonuniform Mesh Grids. *Journal of Computational Physics*, v. 129, n. 2, p. 357–363, 1996.

HEDSTRÖM, B. O. A. Flow of plastic materials in pipes. *Industrial & Engineering Chemistry*, v. 44, n. 3, p. 651–656, 1952.

Hegele Jr, L. A.; MATTILA, K.; PHILIPPI, P. C. Rectangular lattice-Boltzmann schemes with BGK-collision operator. *Journal of Scientific Computing*, v. 56, n. 2, p. 230–242, 2013.

Hegele Jr, L. A.; SCAGLIARINI, A.; SBRAGAGLIA, M.; MATTILA, K. K.; PHILIPPI, P. C.; PULERI, D. F.; GOUNLEY, J.; RANDLES, A. High-Reynolds-number turbulent cavity flow using the lattice Boltzmann method. *Physical Review E*, American Physical Society, v. 98, n. 4, p. 043302, 2018.

HUILGOL, R.; MENA, B.; PIAU, J. Finite stopping time problems and rheometry of Bingham fluids. *Journal of Non-Newtonian Fluid Mechanics*, v. 102, n. 1, p. 97–107, 2002.

HUILGOL, R. R.; ALEXANDROU, A. N.; GEORGIOU, G. C. Start-up plane Poiseuille flow of a Bingham fluid. *Journal of Non-Newtonian Fluid Mechanics*, Elsevier B.V., v. 265, n. July 2018, p. 133–139, 2019.

JANUSZEWSKI, M.; KOSTUR, M. Sailfish: A flexible multi-GPU implementation of the lattice Boltzmann method. *Computer Physics Communications*, North-Holland, v. 185, n. 9, p. 2350–2368, 2014.

JIMENEZ, J.; HOYAS, S. Turbulent fluctuations above the buffer layer of wall-bounded flows. *Journal of Fluid Mechanics*, v. 611, p. 215–236, 2008.

KANG, S. K.; HASSAN, Y. A. The effect of lattice models within the lattice Boltzmann method in the simulation of wall-bounded turbulent flows. *Journal of Computational Physics*, Elsevier Inc., v. 232, n. 1, p. 100–117, 2013.

KHABAZI, N.; TAGHAVI, S.; SADEGHY, K. Peristaltic flow of Bingham fluids at large Reynolds numbers: A numerical study. *Journal of Non-Newtonian Fluid Mechanics*, Elsevier, v. 227, p. 30–44, 2016.

KIM, J.; MOIN, P.; MOSER, R. Turbulence statistics in fully developed channel flow at low Reynolds number. *Journal of Fluid Mechanics*, v. 177, p. 133–166, 1987.

KRÜGER, T.; KUSUMAATMAJA, H.; KUZMIN, A.; SHARDT, O.; SILVA, G.; VIGGEN, E. M. *The lattice Boltzmann method*. Cham, Switzerland: Springer International Publishing, 2017. (Graduate Texts in Physics).

KRÜGER, T.; VARNIK, F.; RAABE, D. Shear stress in lattice Boltzmann simulations. *Physical Review E*, v. 79, n. 4, p. 046704, 2009.

LADD, A. J. C. Numerical simulations of particulate suspensions via a discretized Boltzmann equation. Part 1. Theoretical foundation. *Journal of Fluid Mechanics*, v. 271, n. 1994, p. 285–309, 1994.

LAMMERS, P.; BERONOV, K.; VOLKERT, R.; BRENNER, G.; DURST, F. Lattice BGK direct numerical simulation of fully developed turbulence in incompressible plane channel flow. *Computers & Fluids*, v. 35, n. 10, p. 1137–1153, 2006.

LATT, J.; CHOPARD, B. Lattice Boltzmann method with regularized pre-collision distribution functions. *Mathematics and Computers in Simulation*, North-Holland, v. 72, n. 2-6, p. 165–168, 2006.

LATT, J.; CHOPARD, B.; MALASPINAS, O.; DEVILLE, M.; MICHLER, A. Straight velocity boundaries in the lattice Boltzmann method. *Physical Review E*, v. 77, n. 5, p. 056703, 2008.

LAURENDEAU, N. M. *Statistical thermodynamics: fundamentals and applications*. Cambridge, UK: Cambridge University Press, 2005.

LI, C.-F.; SURESHKUMAR, R.; KHOMAMI, B. Influence of rheological parameters on polymer induced turbulent drag reduction. *Journal of Non-Newtonian Fluid Mechanics*, v. 140, n. 1-3, p. 23–40, 2006.

LUGARINI, A.; FRANCO, A. T.; PHILIPPI, P. C. Lattice Boltzmann method for viscoplastic fluid flow based on regularization of ghost moments. *Journal of Non-Newtonian Fluid Mechanics*, Elsevier B.V., v. 286, n. November 2019, p. 104413, 2020.

LUO, L.-S.; LIAO, W.; CHEN, X.; PENG, Y.; ZHANG, W. Numerics of the lattice Boltzmann method: Effects of collision models on the lattice Boltzmann simulations. *Physical Review E*, v. 83, n. 5, p. 056710, 2011.

LUU, L.-H.; PHILIPPE, P.; CHAMBON, G. Flow of a yield-stress fluid over a cavity: Experimental study of the solid–fluid interface. *Journal of Non-Newtonian Fluid Mechanics*, Elsevier B.V., v. 245, p. 25–37, 2017.

MARTYS, N. S.; SHAN, X.; CHEN, H. Evaluation of the external force term in the discrete Boltzmann equation. *Physical Review E*, v. 58, n. 5, p. 6855–6857, 1998.

MATTILA, K. K.; PHILIPPI, P. C.; Hegele Jr, L. A. High-order regularization in lattice-Boltzmann equations. *Physics of Fluids*, v. 29, n. 4, p. 046103, 2017.

MESBOUA, N.; BENYOUNES, K.; BENMOUNAH, A. Study of the impact of bentonite on the physico-mechanical and flow properties of cement grout. *Cogent Engineering*, Cogent, v. 5, n. 1, p. 1–12, 2018.

MITCHELL, R.; MISKA, S. *Fundamentals of drilling engineering*. Richardson, USA: Society of Petroleum Engineers, 2011.

MOLLA, M. M.; PAUL, M. C. LES of non-Newtonian physiological blood flow in a model of arterial stenosis. *Medical Engineering and Physics*, Institute of Physics and Engineering in Medicine, v. 34, n. 8, p. 1079–1087, 2012.

MORRISON, F. A. *Understanding rheology*. New York, USA: Oxford University Press, 2001.

MURAVLEVA, L.; MURAVLEVA, E.; GEORGIOU, G. C.; MITSOULIS, E. Numerical simulations of cessation flows of a Bingham plastic with the augmented Lagrangian method. *Journal of Non-Newtonian Fluid Mechanics*, Elsevier B.V., v. 165, n. 9-10, p. 544–550, 2010.

NATHEN, P.; GAUDLITZ, D.; KRAUSE, M. J.; ADAMS, N. A. On the stability and accuracy of the BGK, MRT and RLB Boltzmann schemes for the simulation of turbulent flows. *Communications in Computational Physics*, v. 23, n. 3, p. 1–31, 2018.

OHTA, M.; NAKAMURA, T.; YOSHIDA, Y.; MATSUKUMA, Y. Lattice Boltzmann simulations of viscoplastic fluid flows through complex flow channels. *Journal of Non-Newtonian Fluid Mechanics*, v. 166, n. 7-8, p. 404–412, 2011.

OHTA, T.; MIYASHITA, M. DNS and LES with an extended Smagorinsky model for wall turbulence in non-Newtonian viscous fluids. *Journal of Non-Newtonian Fluid Mechanics*, v. 206, p. 29–39, 2014.

OKRAJNI, S.; AZAR, J. The effects of mud rheology on annular hole cleaning in directional wells. *SPE Drilling Engineering*, v. 1, n. 04, p. 297–308, 1986.

Oliveira Jr, W. B.; LUGARINI, A.; FRANCO, A. T. Performance analysis of the lattice Boltzmann method implementation on GPU. In: *XL Ibero-Latin-American Congress on Computational Methods in Engineering (CILAMCE 2019)*. Natal, Brazil: [s.n.], 2019.

OWOLABI, B. E.; DENNIS, D. J. C.; POOLE, R. J. Turbulent drag reduction by polymer additives in parallel-shear flows. *Journal of Fluid Mechanics*, v. 827, p. R4, 2017.

PAPANASTASIOU, T. C. Flows of materials with yield. *Journal of Rheology*, v. 31, n. 5, p. 385–404, 1987.

PEIXINHO, J.; NOUAR, C.; DESAUBRY, C.; THÉRON, B. Laminar transitional and turbulent flow of yield stress fluid in a pipe. *Journal of Non-Newtonian Fluid Mechanics*, Elsevier, v. 128, n. 2-3, p. 172–184, 2005.

PENG, C.; GENEVA, N.; GUO, Z.; WANG, L.-P. Direct numerical simulation of turbulent pipe flow using the lattice Boltzmann method. *Journal of Computational Physics*, Academic Press, v. 357, p. 16–42, 2018.

PENG, C.; GUO, Z.; WANG, L.-P. A lattice-BGK model for the Navier–Stokes equations based on a rectangular grid. *Computers & Mathematics with Applications*, Elsevier Ltd, v. 78, n. 4, p. 1076–1094, 2019.

PENG, C.; WANG, L. P. Direct numerical simulations of turbulent pipe flow laden with finite-size neutrally buoyant particles at low flow Reynolds number. *Acta Mechanica*, p. 1–23, 2018.

PEREIRA, A.; PINHO, F. Turbulent pipe flow characteristics of low molecular weight polymer solutions. *Journal of Non-Newtonian Fluid Mechanics*, Elsevier, v. 55, n. 3, p. 321–344, 1994.

PEREIRA, A.; PINHO, F. Turbulent pipe flow of thixotropic fluids. *International Journal of Heat and Fluid Flow*, v. 23, n. 1, p. 36–51, 2002.

PHILIPPI, P. C.; Hegele Jr, L. A.; SANTOS, L. O. E. dos; SURMAS, R. From the continuous to the lattice Boltzmann equation: The discretization problem and thermal models. *Physical Review E*, v. 73, n. 5, p. 056702, 2006.

PICART, C.; PIAU, J.-M.; GALLIARD, H.; CARPENTIER, P. Human blood shear yield stress and its hematocrit dependence. *Journal of Rheology*, v. 42, n. 1, p. 1–12, 1998.

PINHO, F.; WHITELAW, J. Flow of non-Newtonian fluids in a pipe. *Journal of Non-Newtonian Fluid Mechanics*, v. 34, n. 2, p. 129–144, 1990.

PRASHANT; DERKSEN, J. Direct simulations of spherical particle motion in Bingham liquids. *Computers and Chemical Engineering*, Elsevier Ltd, v. 35, n. 7, p. 1200–1214, 2011.

REGULSKI, W.; LEONARDI, C. R.; SZUMBARSKI, J. On the spatial convergence and transient behaviour of lattice Boltzmann methods for modelling fluids with yield stress. *Journal of Computational Physics, under review*, 2016.

ROSTI, M. E.; IZBASSAROV, D.; TAMMISOLA, O.; HORMOZI, S.; BRANDT, L. Turbulent channel flow of an elastoviscoplastic fluid. *Journal of Fluid Mechanics*, Cambridge University Press, v. 853, p. 488–514, 2018.

RUDMAN, M.; BLACKBURN, H.; GRAHAM, L.; PULLUM, L. Turbulent pipe flow of shear-thinning fluids. *Journal of Non-Newtonian Fluid Mechanics*, Elsevier, v. 118, n. 1, p. 33–48, 2004.

RUDMAN, M.; BLACKBURN, H. M. Direct numerical simulation of turbulent non-Newtonian flow using a spectral element method. *Applied Mathematical Modelling*, Elsevier, v. 30, n. 11, p. 1229–1248, 2006.

SAFRONCHIK, A. I. Non-steady flow of a visco-plastic material between parallel walls. *Journal of Applied Mathematics and Mechanics*, v. 23, n. 5, p. 1314–1327, 1959.

SARAMITO, P. A new constitutive equation for elastoviscoplastic fluid flows. *Journal of Non-Newtonian Fluid Mechanics*, Elsevier, v. 145, n. 1, p. 1–14, 2007.

SARAMITO, P.; ROQUET, N. An adaptive finite element method for viscoplastic fluid flows in pipes. *Computer Methods in Applied Mechanics and Engineering*, v. 190, n. 40-41, p. 5391–5412, 2001.

SHAH, S. N.; SUTTON, D. L. New friction correlation for cements from pipe and rotational-viscometer data. *SPE Production Engineering*, v. 5, n. 04, p. 415–424, 1990.

SILVA, G.; SEMIAO, V. First- and second-order forcing expansions in a lattice Boltzmann method reproducing isothermal hydrodynamics in artificial compressibility form. *Journal of Fluid Mechanics*, Cambridge University Press, v. 698, p. 282–303, 2012.

SINGH, J.; RUDMAN, M.; BLACKBURN, H.; CHRYSS, A.; PULLUM, L.; GRAHAM, L. The importance of rheology characterization in predicting turbulent pipe flow of generalized Newtonian fluids. *Journal of Non-Newtonian Fluid Mechanics*, v. 232, p. 11–21, 2016.

SINGH, J.; RUDMAN, M.; BLACKBURN, H. M. The effect of yield stress on pipe flow turbulence for generalised Newtonian fluids. *Journal of Non-Newtonian Fluid Mechanics*, Elsevier, v. 249, p. 53–62, 2017.

SINGH, J.; RUDMAN, M.; BLACKBURN, H. M. The influence of shear-dependent rheology on turbulent pipe flow. *Journal of Fluid Mechanics*, Cambridge University Press, v. 822, p. 848–879, 2017.

SINGH, J.; RUDMAN, M.; BLACKBURN, H. M. Reynolds number effects in pipe flow turbulence of generalized Newtonian fluids. *Physical Review Fluids*, v. 3, n. 9, p. 094607, 2018.

SUGA, K.; KUWATA, Y.; TAKASHIMA, K.; CHIKASUE, R. A D3Q27 multiple-relaxation-time lattice Boltzmann method for turbulent flows. *Computers & Mathematics with Applications*, Pergamon, v. 69, n. 6, p. 518–529, 2015.

SYRAKOS, A.; GEORGIOU, G. C.; ALEXANDROU, A. N. Solution of the square lid-driven cavity flow of a Bingham plastic using the finite volume method. *Journal of Non-Newtonian Fluid Mechanics*, Elsevier, v. 195, p. 19–31, 2013.

SYRAKOS, A.; GEORGIOU, G. C.; ALEXANDROU, A. N. Performance of the finite volume method in solving regularised Bingham flows: Inertia effects in the lid-driven cavity flow. *Journal of Non-Newtonian Fluid Mechanics*, v. 208-209, p. 88–107, 2014.

TANG, G.; WANG, S.; YE, P.; TAO, W. Bingham fluid simulation with the incompressible lattice Boltzmann model. *Journal of Non-Newtonian Fluid Mechanics*, v. 166, n. 1-2, p. 145–151, 2011.

THOMAS, A. D.; WILSON, K. C. New analysis of non-Newtonian turbulent flow - yield-power-law fluids. *The Canadian Journal of Chemical Engineering*, v. 65, n. 2, p. 335–338, 1987.

THOMAS, D. G. Transport characteristics of suspensions: Part IV. Friction loss of concentrated-flocculated suspensions in turbulent flow. *AIChE Journal*, v. 8, n. 2, p. 266–271, 1962.

TOMITA, Y. A study on non-newtonian flow in pipe lines. *Bulletin of JSME*, v. 2, n. 5, p. 10–16, 1959.

TOUIL, H.; RICOT, D.; LÉVÊQUE, E. Direct and large-eddy simulation of turbulent flows on composite multi-resolution grids by the lattice Boltzmann method. *Journal of Computational Physics*, Elsevier Inc., v. 256, p. 220–233, 2014.

VIKHANSKY, A. Lattice-Boltzmann method for yield-stress liquids. *Journal of Non-Newtonian Fluid Mechanics*, v. 155, n. 3, p. 95–100, 2008.

VIKHANSKY, A. Construction of lattice-Boltzmann schemes for non-Newtonian and two-phase flows. *The Canadian Journal of Chemical Engineering*, v. 90, n. 5, p. 1081–1091, 2012.

WANG, C.-H.; HO, J.-R. Lattice Boltzmann modeling of Bingham plastics. *Physica A: Statistical Mechanics and its Applications*, v. 387, n. 19-20, p. 4740–4748, 2008.

WANG, G.; WAN, D.; PENG, C.; LIU, K.; WANG, L. P. LBM study of aggregation of monosized spherical particles in homogeneous isotropic turbulence. *Chemical Engineering Science*, Elsevier Ltd, v. 201, p. 201–211, 2019.

WEN, C. *The transition to asymmetry in pipe flow of shear-thinning fluids*. Thesis (PhD) — University of Liverpool, 2016.

WHITE, F. M. *Viscous fluid flow*. 3. ed. Ahmedabad, India: Tata Mcgraw Hill, 2011. 652 p.

WILSON, K. C.; THOMAS, A. D. A new analysis of the turbulent flow of non-Newtonian fluids. *The Canadian Journal of Chemical Engineering*, v. 63, n. 4, p. 539–546, 1985.

XIE, C.; ZHANG, J.; BERTOLA, V.; WANG, M. Lattice Boltzmann modeling for multiphase viscoplastic fluid flow. *Journal of Non-Newtonian Fluid Mechanics*, v. 234, p. 118–128, 2016.

ZHENG, E.; RUDMAN, M.; SINGH, J.; KUANG, S. Direct numerical simulation of turbulent non-Newtonian flow using OpenFOAM. *Applied Mathematical Modelling*, Elsevier Inc., v. 72, p. 50–67, 2019.

ZOU, Q.; HE, X. On pressure and velocity boundary conditions for the lattice Boltzmann BGK model. *Physics of Fluids*, v. 9, n. 6, p. 1591–1598, 1997.